A thesis for the degree of Doctor of Philosophy

Elastic Anomaly of Adsorbed Films

February 2019

Graduate School of Science and Technology
Keio University

Takahiko Makiuchi

Acknowledgements

This work was done during my last three years in Shirahama Laboratory, Department of Physics, Faculty of Science and Technology, Keio University. I owe my achievement especially to my supervisor, Professor Keiya Shirahama. He gave me opportunities to struggle with challenging issues, he let me use a gorgeous French dilution refrigerator and a great amount of expensive liquid helium, and he treated me as a physicist, for my view, when we discussed. I greatly acknowledge his leadership, kindness, and passion.

I also thank the thesis committee members, Professor Atsushi Hotta, Professor Keiji Saito, and Professor Shinichi Watanabe for valuable feedback and comments, especially on interpretations of my results.

I thank Prof. Daisuke Takahashi (Ashikaga), one of my coworkers, for encouraging me time after time. I also thank Prof. John Beamish (Alberta), Dr. Ján Nyéki (Royal Holloway), Dr. Michikazu Kobayashi (Kyoto), Dr. Aron Beekman (Keio), Prof. Tomi Ohtsuki (Sophia), and Dr. Tomoki Minoguchi (Tokyo) for fruitful discussions. I also appreciate discussions with members in the Quantum Fluids and Solids community.

People in the lab helped me a lot. I have learned a lot of technical experience from Dr. Satoshi Murakawa and Tomoya Tsuiki, without which I cannot accomplish the research. Time spent with them was delightful. Dr. Yusuke Nago helped me for improvements of the articles and presentations. He was also kind to guide me in nanofabrication world, though I could not afford to start a new topic during this period. I am grateful to Michihiro Tagai, who designed and fabricated the torsional oscillator and did some experiments with me in the early stage. His torsional oscillator was so successful that it could unveil new aspects, the elastic anomaly, of thin adsorbed helium, hydrogen and neon films that could ever not be examined with any other method. I thank Katsuyuki Yamashita for fabricating some equipment and helping the neon and hydrogen experiments. I also thank Noriyuki Usami for helping me to fabricate Grafoil torsional oscillators and the pressure gauge of Kapton diaphragm, and Takahiro Suzuki for the characterization of Grafoil. The Grafoil experiment is ongoing and I hope we can do something

important. Many colleagues made my life in doctoral course valuable: Tomoyuki Tani, Misuzu Sakai, Kosuke Mikuni, Takumi Shimoda, Ryoma Wada, Kohei Kaiya, Yu Tanaka, Keisuke Kuwahara, Yusuke Morikawa, Tomoki Murakami, Kenta Abe, Ryohei Kiyota, and Yusuke Miyoshi.

I thank many people in Keio University. My life at Keio has been made valuable by my friends: Philipp Gubler, Ryo Hanai, Daichi Kagamihara, Ryuichiro Kawakubo, Digvijay Kharga, Amane Kobayashi, Yusuke Masaki, Morio Matsumoto, Satoshi Natori, Mao Oide, Shoko Okuda, Sho Ozaki, Yuki Sekiguchi, Hideyuki Sera, Hiroyuki Tajima, Shuji Tamaki, Pieter van Wyk, and Ryo Yokokura.

Special thanks goes to my mother, Yuko. She has constantly encouraged and helped me so that I could continue my research with little anxiety about my career and finance. I am also grateful to my sister and her husband for their warm help. I was so happy in the laboratory during my experiment last summer to hear that their daughter was born. Finally, I thank my father, the late Professor Katsuhiko Makiuchi, for his continuous guidance to science and engineering from my childhood to his last sleep.

I was financially supported by Japan Society for the Promotion of Science, and by Keio University: Grant-in-Aid for JSPS Research Fellow JP18J13209 (2018), Research Grant of Keio Leading-edge Laboratory of Science and Technology (2016, 2017), and Keio University Doctorate Student Grant-in-Aid Program (2016).

Contents

Chapter 1

Introduction

Physical adsorption is a ubiquitous phenomenon in everyday life, but understanding and controlling it is still a challenging issue in both basic science[1, 2] and modern technologies such as hydrogen storage[3] and gas sensing[4]. This thesis presents a series of elasticity measurements for helium, neon, and hydrogen films adsorbed on a porous glass substrate by means of torsional oscillator technique.

In condensed matter physics, adsorption of molecules on a solid surface has been utilized to produce two-dimensional (2D) films that show a number of emergent phenomena that are not observed in the bulk materials. In a classical picture, an adsorbed film is bound to the substrate due to van der Waals attraction, and freezes at absolute zero. An important exception is ^{4}He film, which becomes superfluid due to large zero-point fluctuation and weak interaction. A few atomic layers of ^{4}He film adsorbed on a solid substrate exhibit superfluidity when the film coverage (or density) exceeds a critical value, which is typically two atomic layers [5]. The ^{4}He film thinner than the critical coverage is in a localized phase at low temperatures. The many-body state of the localized phase has attracted attentions, and a possibility of Bose glass had been proposed [6]. However, there had been inconsistencies among theories and experiments. The seminal Bose glass model propose that the localized phase is gapless and compressible, but the heat capacity measurement revealed that the thin ^{4}He film is actually gapped [7]. The elasticity is an essential physical quantity in the localized phase because it is linked to the compressibility, but there had been no method to directly measure the elasticity of adsorbed films at low temperatures.

In this thesis, I have used a torsional oscillator which can directly measure the elasticity and dissipation in adsorbed films. I and coworkers discovered an *elastic anomaly*, in which the elasticity increases at low temperatures with an excess dissipation, in both bosonic ^{4}He and fermionic ^{3}He films below 1 K [8].

The elastic anomaly is explained by thermal activation of atoms from the localized to spatially-extended band and an elastic relaxation process. Helium films are in a localized phase which is gapped and compressible, probably a sort of Mott insulator or Mott glass. By increasing the coverage, the localized helium films undergo a (super)fluid–insulator quantum phase transition, together with a gap closure and a vanishment of the elastic anomaly.

To examine whether the elastic anomaly is intrinsic to the quantum phase transition of helium films or not, I conducted similar experiments for neon, a less quantum noble gas, and hydrogen isotopes H_2, HD (hydrogen deuteride), and D_2 (deuterium). The low temperature properties of neon and hydrogen films had been less investigated and the phases of the ground state and at finite temperature, and the phase transitions had not been elucidated. Neon film shows the elastic anomaly at about 5 K, and does not show quantum phase transition [9]. I also observed the elastic anomaly in bosonic H_2 and D_2, and fermionic HD films in a temperature range 1–10 K. Unlike helium and neon, the elastic anomaly of hydrogen appears at several temperatures. The discoveries of the elastic anomaly in every film examined suggest that it is a universal phenomenon in adsorbed molecular films.

This chapter is an introduction to the quantum matters (helium, hydrogen, and neon), the physical adsorption, and the previous studies on thin films. Chapter 2 describes the experimental apparatus and methods used in the helium, neon, and hydrogen experiments. In Chapters 3, 4, and 5, I show the experimental results, analyses, and discussion for helium, neon, and hydrogen films, respectively. Chapter 6 is conclusions.

1.1 Helium, hydrogen, and neon

Condensed helium, hydrogen and neon are quantum matters due to large zero point energies and weak intermolecular (interatomic) interactions. Helium becomes quantum liquid, i.e., superfluid, even at absolute zero temperature, at which all other molecules solidify [10]. Molecular hydrogen becomes quantum solid where the amplitude of zero-point motion is comparable to the lattice constant [11]. Solid neon is barely a quantum solid in the sense that the nearest neighbor distance is slightly larger than the distance of pair potential minimum due to zero-point motion [12].

1.1.1 Isotopes and states of molecular hydrogen

Helium exists in bosonic and fermionic counterparts, ^{4}He and ^{3}He, as stable isotopes. As two electrons fill up the K shell, helium is chemically inert and exists as

Table 1.1: Possible combinations of the quantum numbers J and I for H_2 and D_2 at the ground and first excited states. The abbreviations S and AS denote symmetric and antisymmetric, respectively.

	level	J	I	g_I	designation
H_2	ground	0 (S)	0 (AS)	1	para
	first excited	1 (AS)	1 (S)	3	ortho
D_2	ground	0 (S)	0, 2 (S)	6	ortho
	first excited	1 (AS)	1 (AS)	3	para

a noble gas atom.

Neon is the second lightest noble gas after helium. The stable isotopes of neon are bosonic ^{20}Ne and ^{22}Ne, and fermionic ^{21}Ne, in descending order of the natural abundance.

Hydrogen (H, nuclear spin 1/2) and deuterium (D, nuclear spin 1) are stable isotopes of hydrogen atom. We used molecular hydrogens, H_2, HD and D_2, in the present study. For solid hydrogen, important properties are associated with degrees of freedom in two nuclei [11, 13]. The nuclear part of the wave function of hydrogen molecule divides into the orbital and spin part. The quantum numbers linked to the orbital part are a vibrational quantum number $v = 0,\ 1, \ldots$ and a rotational quantum number $J = 0,\ 1, \ldots$. The quantum number for the nuclear spin part is I, which can be 0 or 1 for H_2, 1/2 or 3/2 for HD, and 0 or 2 for D_2. The nuclear wave function of H_2 and D_2 must be symmetric under exchange of the nuclei because of the principle of indistinguishability of identical particles. The energy level difference between $J = 0$ and $J = 1$ is of the order of 100 K, whereas that of $v = 0$ and $v = 1$ is more than 1000 K [13]. The spin part energetically contribute to hyperfine splitting of $J \neq 0$ levels of the order of 10^{-5} K [11]. As we are concerned with the ground and first excited state, we set $v = 0$ and consider the combination of J and I, which is listed in Table 1.1.

The nuclear spin degeneracy g_I is statistical weight which determine the existence ratio from Boltzmann distribution. The states which have larger g_I are called *ortho*, and the others are *para*. The existence ratio of ortho- to para-H_2 is 3:1, and that of ortho- to para-D_2 is 2:1 at high temperature, e.g., at room-temperature. At the liquid ^{4}He temperature (4 K), almost 100 % of H_2 or D_2 is the ground state species, para-H_2 or ortho-D_2, in equilibrium. The ortho–para conversion from $J = 1$ to $J = 0$ state needs to flip the spin state at the same time, and the latter can occurs only when strong inhomogeneous magnetic or electric fields are applied [11]. Therefore we generally need magnetic catalyst to accelerate the conversion in the experimental time (hours or days). On the other hand, HD has two distinguishable

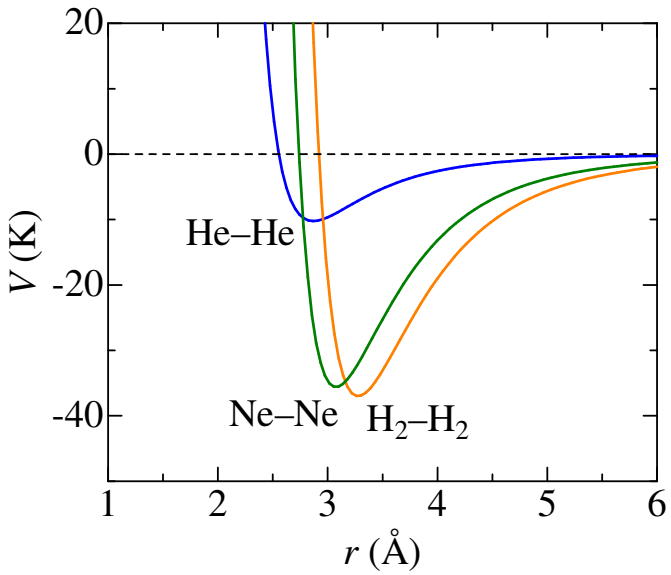

Figure 1.1: Lennard-Jones potential using parameters in Table 1.2.

nuclei, therefore it has no restriction between the rotational and spin states.

For every hydrogen molecules, the first excited state is the rotational state $v = 0$, $J = 1$. The wave function of hydrogen molecule with $J = 1$ is an elongated ($M = 0$) or a flattened ($M = \pm 1$) spheroid shape.

1.1.2 Intermolecular interaction

Two neutral molecules attract each other with van der Waals force, whose potential energy is proportional to $-1/r^6$, where r is an intermolecular distance. The origin of the van der Waals force for closed-shell atoms, such as helium and neon, is London dispersion force, which is weak [14].

The simple and commonly used intermolecular potential is the Lennard-Jones potential (or 6–12 potential), which is

$$V(r) = 4\varepsilon \left[\left(\frac{\sigma}{r}\right)^{12} - \left(\frac{\sigma}{r}\right)^{6} \right], \tag{1.1}$$

where $\varepsilon > 0$ is a potential depth, and σ is a parameter of distance. The potential minimum is at $r = \sqrt[6]{2}\sigma \simeq 1.12\sigma$. The second term is the van der Waals potential, and the first term is a short-range repulsion.

Table 1.2: The mass, Lennard-Jones parameters [15], and quantum parameter of molecules.

	m (u)	σ (Å)	ε (K)	Λ
^{3}He	3.016	2.556	10.22	3.08
^{4}He	4.003	”	”	2.68
H_2	2.016	2.92	37.0	1.74
HD	3.022	”	”	1.42
D_2	4.028	”	”	1.23
Ne	20.18	2.74	35.6	0.60
Ar	39.95	3.41	120	0.19

A harmonic approximation for the Lennard-Jones potential gives

$$V(r) \simeq -\varepsilon + \frac{k}{2}(r - \sqrt[6]{2}\sigma)^2, \tag{1.2}$$

where $k = 72\varepsilon/(\sqrt[3]{2}\sigma^2)$ is a spring constant. The zero-point energy is

$$\text{(Zero-point energy)} = \frac{\hbar\omega}{2} = \frac{\hbar}{2}\sqrt{\frac{k}{m}} \simeq 0.602\frac{h}{\sigma}\sqrt{\frac{\varepsilon}{m}}. \tag{1.3}$$

Note that, for example, zero-point energy of ^{4}He calculated from Eq. (1.3), 19.0 K, is larger than the potential depth $\varepsilon = 10.22$ K. This is because we have overestimated the curvature around the potential minimum and thus the harmonic approximation was not adequate for ^{4}He. But this simple equation is still useful. Here we introduce a quantum parameter [16]

$$\Lambda = \frac{h}{\sigma\sqrt{m\varepsilon}}, \tag{1.4}$$

which is roughly a ratio of the zero-point energy to the intermolecular potential depth, ε. The larger the quantum parameter is, the more the molecule has quantum characters.

1.1.3 Bulk phase diagram

Figure 1.2 shows the phase diagrams of bulk helium, hydrogen, and neon. In Fig. 1.2(a), there exist quantum liquid phases even at $T = 0$, and no triple point for a solid–liquid–gas coexistence. The superfluid transition line of ^{4}He is at about 2 K, which is close to the Bose–Einstein condensation temperature, 3.1 K, calculated from the density of liquid ^{4}He and considering it as a ideal Bose gas [17]. Fermionic ^{3}He becomes superfluid at ultra low temperature about 2 mK, because the attractive

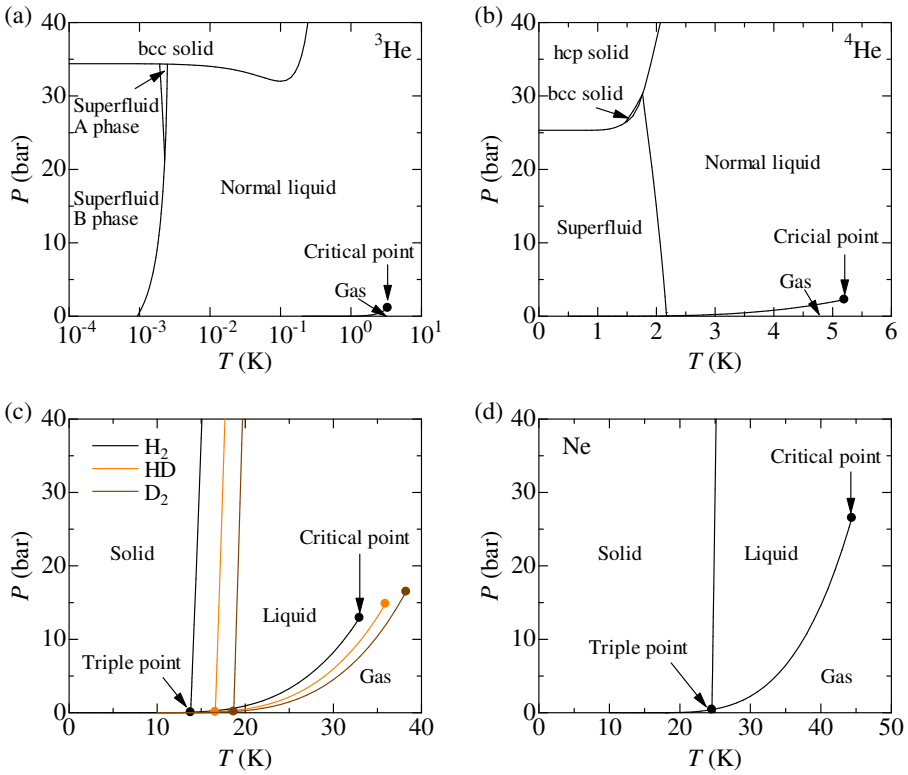

Figure 1.2: Temperature–pressure phase diagrams of (a) ^{3}He, (b) ^{4}He, (c) H_2, HD and D_2, and (d) Ne. The pressure ranges are common, but the temperature ranges are different from each other (logscale for ^{3}He). Phase boundary data were taken from Refs. [18, 19, 20, 21], [18, 19, 22], [23], and [24] for (a)–(d), respectively.

interaction mediated by spin fluctuation for Cooper pairing is weak. The melting curve of ^{4}He has very small slope below 1 K, which means that the entropy of solid and superfluid phase are almost equal, using a Clausius–Clapeyron relation

$$\frac{dP}{dT} = \frac{s_\mathrm{l} - s_\mathrm{s}}{v_\mathrm{l} - v_\mathrm{s}}. \tag{1.5}$$

The melting curve of ^{3}He has a dip at about 100 mK, below which $s_\mathrm{l} > s_\mathrm{s}$.

The phase diagram of H_2, HD and D_2 are described in Fig. 1.2 (c). The phase separation lines and the triple and the critical points are shifted to higher temperatures by increasing the mass. The phase diagrams of hydrogen, and Ne in Fig. 1.2 (d) are typical ones in thermodynamics.

Table 1.3: Properties of helium, hydrogen, and neon. v_m^{liq} and v_m^{sol}: molar volume of liquid and solid at triple point (hydrogen and neon) or at 0 K, 0 bar (helium) from Refs. [18, 23, 24]; T_c: superfluid transition temperatures (highest values) [18]; T_t and p_t: triple point temperature and pressure [19, 23]; T_b: boiling temperature at 1 bar [18, 19, 23]; T_C and p_C: critical temperature and pressure [18, 19, 23].

	^{3}He	^{4}He	H_2	HD	D_2	^{20}Ne
Statistics	fermion	boson	boson	fermion	boson	boson
I	1/2	0	0	1/2, 3/2	0, 2	0
m (u)	3.016	4.003	2.016	3.022	4.028	20.18
v_m^{liq} (cm^3/mol)	36.84	27.58	26.173	24.62	23.262	16.17
v_m^{sol} (cm^3/mol)	—	—	23.30	21.84	20.58	14.19
T_c (K)	0.0025	2.1768	—	—	—	—
T_t (K)	—	—	13.803	16.60	18.691	24.56
P_t (bar)	—	—	0.07042	0.124	0.1713	0.433
T_b (K)	3.19	4.21	20.268	22.14	23.63	27.1
T_C (K)	3.32	5.1953	32.976	35.908	38.262	44.4
P_C (bar)	1.15	2.2746	12.928	14.839	16.497	27.6

1.2 Physical adsorption

1.2.1 Molecule–surface interaction

A molecule in the vicinity of a substrate experiences an adsorption potential. Although the realistic molecule–substrate interaction is complex [12], its simple form is obtained by an assumption that the molecule and the atoms in the substrate interact with 6–12 potential, and the interaction is additive. Integrating Eq. (1.1) over a semi-infinite ($z < 0$) mono-atomic substrate of an atom number density n, we get a 3–9 potential

$$V(z) = 4\pi\varepsilon n \left[\frac{\sigma^{12}}{45z^9} - \frac{\sigma^6}{6z^3} \right]. \tag{1.6}$$

We can rewrite the 3–9 potential as

$$V(z) = \frac{4C_3^3/27D^2}{z^9} - \frac{C_3}{z^3}, \tag{1.7}$$

where $C_3 = 2\pi\varepsilon n\sigma^6/3$ is a van der Waals dispersion coefficient and $D = 2\sqrt{10}\pi\varepsilon n\sigma^3/9$ is a potential depth [25, 26, 27, 28]. The potential minimum is at $z_0 = \sqrt[3]{2C_3/3D}$. The ground-state binding energy E_b is smaller than D in magnitude because of the zero-point energy. Selected parameters from previous studies or from Eq. (1.6)

Table 1.4: Parameters of the 3–9 potential for several molecule–substrate (adsorbate–adsorbent) combinations: the van der Waals dispersion coefficient C_3, the potential depth D, and the ground-state binding energy E_b. Data are from reference or calculation. For E_b, data are for ^{4}He and H_2, and in parentheses are for ^{3}He or D_2.

	C_3 (KÅ^3)	D (K)	E_b (K)	Ref.
He–graphite	2090 ± 180	193 ± 5	143 ± 2 (135 ± 2)	[26]
He–SiO_2	1290	100		[29, 30]
He–NaF	850	87.9	57.1 (52.2 ± 0.7)	[26]
He–^{4}He(liq.)	130.3	8.227	7.2 (5.0)	Eq. (1.6), [26]
He–Cs	673	4.4	1.7	[26]
H_2–graphite	6030 ± 350	600 ± 6	483 ± 4 (517)	[26]
H_2–NaF	2510	305		[26]
H_2–H_2(sol.)	1240	52.6		Eq. (1.6)
HD–HD(sol.)	1320	56.1		Eq. (1.6)
D_2–D_2(sol.)	1410	59.5		Eq. (1.6)
Ne–graphite	4010	378	349	[26]
Ne–NaF	1720	149.3		[26]
Ne–Ne(sol.)	1340	68.6		Eq. (1.6)

are listed in Table 1.4. The values of C_3 and D are common among isotopes. The curves of 3–9 potential for He on four substrates are shown in Fig. 1.3.

Looking into the data in Table 1.4, we find that C_3, D and E_b are small for helium, and large for hydrogen. This fact is because helium only has dipole moment fluctuation, while hydrogen has dipole and higher order electric moments. Neon has intermediate values between helium and hydrogen.

Graphite substrate has the deepest potential D among every substrate shown in Table 1.4. Basal-plain graphite surface is a honeycomb lattice of carbon atoms, and a molecule on graphite favors to be at a site which is surrounded by six carbon atoms. The carbon-carbon bond distance is 0.142 nm, and the distance between a pair of nearest adsorption sites is 0.246 nm. The amplitude of the corrugation potential is 40 K [31]. The corrugation is not so strong that it does not prevent the lateral motion of single adsorbed molecule.

Although silica porous materials are abundant not only in adsorbed film studies but also in our everyday lives as silica gel, available data of adsorption parameters are very few. Boninsegni gathered the parameters for ^{4}He–SiO_2 from three numerical and theoretical studies [29], and we chose one of them [30] for Table 1.4. The parameters C_3 and D are smaller than those for graphite substrate, but still larger

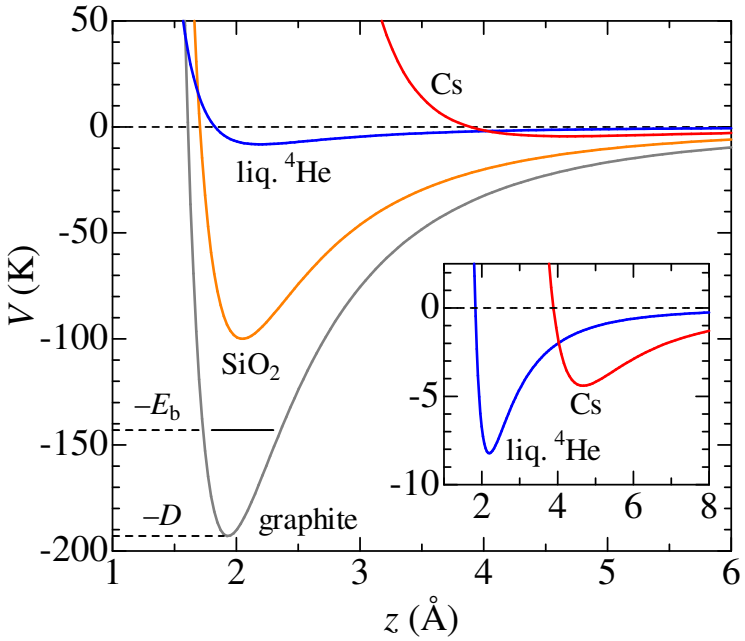

Figure 1.3: 3–9 potential for He (either ^{4}He and ^{3}He) on four different substrates using parameters in Table 1.4. The potential depth and the ground-state binding energy (for ^{4}He) is shown only for graphite substrate. The inset shows an expanded view for "liquid ^{4}He" and Cs substrates.

than those for NaF substrate. Data on NaF is available for every molecules in the table, and shown for comparison.

The coefficients for molecule on homogeneous condensate, such as He–^{4}He(liq.), are calculated from Eq. (1.6) and Lennard-Jones parameters in Table 1.2. Note that a parameter of long-range attraction C_3 of He–^{4}He(liq.) is the smallest among all the substrates [27], including those not appeared in Table 1.4. The potential depth D is, however, smaller for He–Cs than for He–^{4}He(liq.) because the outer dense electrons of alkali atoms give rise to an large repulsion for He atom. Helium atoms prefer to aggregate into a condensate instead of being adsorbed onto Cs, which means that helium film does not wet Cs surface.

The 3–9 potential ignores the structure of the surface and interactions among adsorbed atoms, therefore diverse physics appears in real adsorbed film systems, which we are looking at from now.

1.2.2 Adsorbed films on ordered and disordered substrates

Physical adsorption of atoms (molecules) takes place when the temperature T of the system (atoms and substrate) is so low that atoms can not escape from the binding energy by thermal vibration. The substrates employed in experiments are mostly solid surfaces with large surface area, e.g., porous materials, packed powders, and chemically exfoliated materials.

The surface is characterized by analyzing an adsorption isotherm. We show typical adsorption isotherms for graphite and porous glass substrates in Fig. 1.4. These adsorption isotherms are taken at or below the boiling temperature of adsorbate, e.g., 77 K for nitrogen. The step-wise curve of the isotherm on graphite is a signature of layer-by-layer growth of the adsorbed atoms. The lower the temperature, the sharper the step becomes. On the other hand, the gentle slope on porous glass suggests that the adsorbed film continuously grows without layer structure. The surface of porous glass is highly disordered, and it is natural to think that the adsorbed film forms a non-crystalline (amorphous) film. The hysteresis at higher pressure is due to capillary condensation. In the next section, we see the detailed characters of the substrates.

Typical examples of (a) an adsorption isotherm on graphite (ordered substrate) and (b) an adsorption-desorption isotherm on porous glass (disordered substrate). In (a), the steps of the isotherm indicate the layer-by-layer growth of adsorbed molecules. In (b), the gradual increase in $0 < P/P_0 < 0.4$ indicates that distinct layer structure is not present. The hysteresis in $0.4 < P/P_0 < 0.8$ is due to capillary condensation with distributed pore diameter.

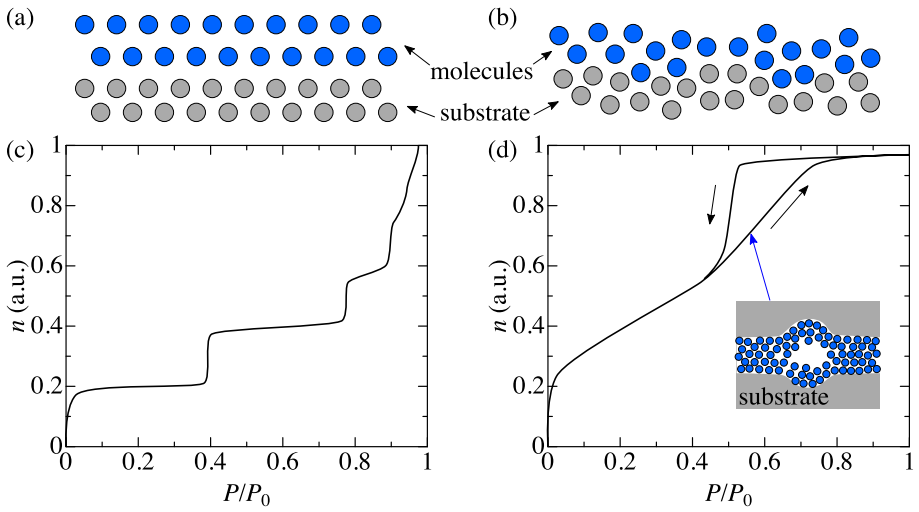

Figure 1.4: Schematic illustrations of adsorption on (a) ordered and (b) disordered substrates, and typical adsorption isotherms on (c) ordered and (d) disordered porous substrates. The pressure P is divided by a saturated vapor pressure P_0, and n is a coverage or an amount of adsorbed molecules. The inset in (d) describes capillary condensation in the adsorption process.

Ordered substrates

The basal-plane of graphite provides periodic potential for adsorbed atoms. Exfoliated graphite such as Grafoil and ZYX [32, 33] have been used in torsional oscillator [34, 35], heat capacity [36, 37, 38] measurements, etc. because they have huge specific surface area (surface area per mass) favorable to enhance the sensitivity. Grafoil has a typical platelet size 10–20 nm with the specific surface area 15–20 m^2/g [36]. ZYX has large platelet size 100–200 nm but small specific area compared with Grafoil. In third sound measurements, the highly oriented pyrolytic graphite (HOPG) is used [39].

On the periodic potential produce by graphite, adsorbed films (He, H_2, Ne, Kr, etc.) grow layer-by-layer and exhibit plural (first order) phase transitions [12]. The stepwise structure of adsorption isotherm is observed for many molecules, such as ^{4}He [39], HD [40], Ne [41], and N_2 [42]. Monolayer films exhibit several phases and those coexistence, commensurate solid, gas, liquid, liquid-gas, solid-gas and so on. Helium on graphite forms clear layer structures from one to more than seven atomic layers [34, 39]. In one or two layers films, commensurate phases, in which the number ratio of the adatoms and sites is rational, appears at certain coverages (densities). The first layer commensurate phase is $\sqrt{3} \times \sqrt{3}$ phase at $n =$

6.36 nm^{-2}, in which the nearest atoms separation is $\sqrt{3}$ times larger than the site distance. Actually, there exists various emergent phases in the first and the second layer of ^{4}He [37, 38] and ^{3}He [36] on graphite. Potential corrugation provided by graphite and correlation between helium atoms produce various ordered phases, up to 2 layers, such as Mott insulator, heavy Fermi liquid, nuclear magnetic phases, and coexistence of superfluid and density wave order [35, 43, 44].

A facet of cleaved ionic crystals such as MgO provide a square surface lattice, in contrast to the triangular lattice on the graphite [12]. The isotherm of adsorbed molecules on MgO shows the step-wise structure, the sign of layer-by-layer growth [45, 46, 47].

Disordered substrates

Most of the substrates do not provide the atomically-ordered adsorption potential because of an amorphous structure, impurities, defects, or a geometric constraint. We classify such substrates as disordered substrates. On disordered substrates, molecules do not grow layer-by-layer.

Porous silica glass is a frequently used disordered substrates in adsorption studies. A single piece of porous glass which is more than a few centimeters long is generally available. Porous Vycor glass has three-dimensionally connected pores from one end to another [48], whose real-space image is shown in Fig. 1.5. The mean pore diameter of Vycor is typically 1–10 nm. The specific surface area is larger than 100 m^2/g. Porous Gelsil glass has recently been used to study helium in restricted geometries [49, 50, 51]. Although the pore diameter is comparable or slightly smaller than Vycor, it is known to be a host of the localized Bose–Einstein condensate of liquid ^{4}He where the pores are fully filled with. Molecules are adsorbed on the pore wall of the porous glass, which is schematically shown in Fig. 1.6. Adsorption isotherms on Vycor were extensively studied for ^{4}He [52], ^{3}He [53], H_2 [54, 55], D_2 [55], and Ne [55]. For porous glasses which has small pore size, such as Vycor and Gelsil, the adsorption and desorption isotherms are hysteretic due to capillary condensation , which is shown in Fig. 1.4(b).

Porous glasses are disordered substrates both in the distribution of the pore diameter and in surface roughness in atomic level. Helium 4 film adsorbed on Vycor at $n > n_c$ is superfluid, and the power law of the superfluid density is rather three-dimensional, $\rho_s \propto (1 - T/T_\lambda)^{2/3}$ [5]. Gelsil is the same kind of porous glass with a relatively small pore diameter compared with Vycor. The phase diagram of ^{4}He film on Gelsil is similar to that of Vycor [49]. A clear difference is in the full-pore region: Liquid ^{4}He confined in Gelsil exhibits localized Bose–Einstein condensation and a quantum phase transition [51], whereas liquid ^{4}He in Vycor does not.

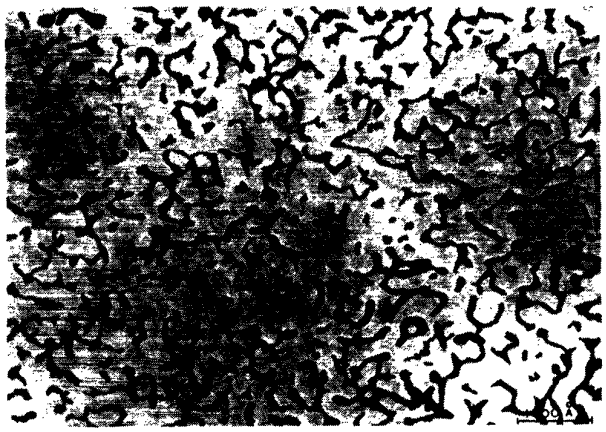

Figure 1.5: Transmission electron micrograph of a section of porous Vycor glass [48]. The pore is in white, and the silica is in black. The scale bar at the bottom-right is in 1000 Å. [Reprinted with permission from P. Levitz, G. Ehret, S. K. Sinha, and J. M. Drake, The Journal of Chemical Physics **95**, 6151 (1991). Copyright 1991 ACS Publications.]

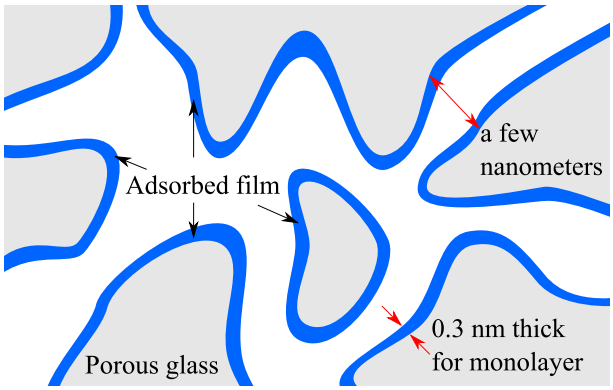

Figure 1.6: Schematic drawing of the cross-section of a Vycor- and Gelsil-like porous glass (grey) on which a molecular film (blue) is formed. The pores (white) are three-dimensionally connected. The distance between the porous glass walls is a few nanometers.

The Kosterlitz–Thouless (KT) transition [56] was first realized in a few atomic layers of ^{4}He film on a roll of Mylar, a plastic film [57, 58]. In previous experiments [57, 58, 59, 60, 61], a long Mylar strip was rolled with spacers of micron-sized aluminum powders and was encapsulated in a torsion bob of the oscillator. The total surface area was a few square meters. On this substrate, ^{4}He film is two-dimensional and undergoes the KT transition when the coverage exceed a critical value, about 28 μmol/m^2 [59].

Although the porous gold is not a glass, we would like to mention it here because it is the only substrate where crossover from KT to 3DXY has been observed other than porous glass. Porous gold used by Csáthy *et al.* has large pore diameter, and the adsorbed ^{4}He film exhibits Kosterlitz–Thouless transition [62, 63]. A Kosterlitz–Thouless transition of ^{4}He film on a planer gold shows beautiful agreement with the theory [64].

Wada and coworkers employed a series of porous materials which vary the dimensionality of adsorbed helium from 3D to 0D [65]. Hectorite provide 2D flat surfaces which are stacked with by pillars. The surface of Hectorite is assumed to be smectite layer (kagome structure) of oxygen atoms, with adsorption site spacing of 0.57 nm [65, 66]. But no layer-by-layer growth has been observed by vapor pressure and heat capacity measurements, so I consider that Hectorite can be classified as a disordered substrate due to heterogeneity of the surface and the pillars.

1.3 Enigma of localized adsorbed films

Adsorbed molecules localize to the substrate in several conditions. In classical mechanics, molecules stop any thermal motion at $T = 0$, and they are completely localized to the substrate due to attractive force from the substrate. How do molecules localizes when the quantum mechanics is involved? For interacting particles in spatially periodic potential, the insulating phase is a Mott insulator. In disordered potentials, Anderson insulator and Bose glass are the candidates for the insulating phase. Adsorbed helium films on disordered substrate are strongly correlated system which are localized at a low coverage, which corresponds to less than 2 atomic layers. The phase of the localized ^{4}He film is, however, elusive. Up to now, no theory or model is consistent with experimental observations for the localized ^{4}He film.

The localized phase is in contact with the superfluid phase at a quantum critical point at $n = n_c$ and $T = 0$. The quantum phase transition is driven by changing the film coverage n. In the context of quantum phase transition, to know the localized phase is to know better the superfluid phase and the whole picture of ^{4}He film.

We see previous studies of the localized and superfluid ^{4}He film as follows. We

also mention the studies of ^{3}He, hydrogen and neon films on disordered substrates.

1.3.1 Superfluid onset in helium 4 films

It has long been known that ^{4}He film on solid surface becomes superfluid. A textbook example is the film flow experiment [67], in which a film of 100 atomic layers (30 nm) in thickness flows without friction below the bulk transition temperature $T_\lambda = 2$ K. The coherence length $\xi(T)$ of the bulk superfluid ^{4}He is $\xi(0) = 0.3$ nm at $T = 0$, which is almost equal to the diameter of a ^{4}He atom. Therefore, by reducing the film thickness toward a few atomic layers, the superfluid film is considered to be a spatially two-dimensional system. Long-range order (such as off diagonal long range order in 3D) can not exist at a finite temperature in two-dimension due to large fluctuation. On the other hand, the superfluidity of atomically thin helium films adsorbed on substrates has been observed [68]. Kosterlitz and Thouless showed that a superfluid transition associated with vortex-antivortex pairing with quasi-long-range order (power-law decay of correlation function to distance) is possible in two-dimensional system at finite temperature [56]. The prediction of KT theory is that the superfluid density ρ_s jumps from zero to finite at the KT transition temperature T_{KT}, and the ratio between ρ_s and T_{KT} is universal [69],

$$\frac{\rho_s(T_{KT}^-)}{T_{KT}} = \frac{2k_B m^2}{\pi\hbar^2}, \tag{1.8}$$

where, m is a mass of the particle. A dynamic version of the KT transition [70] and the universal jump were shortly confirmed in ^{4}He film adsorbed on a plastic Mylar film [57, 58]. As Mylar is a polyester film (stretched polyethylene terephthalate), the surface is disordered in atomic scale. The dynamic KT transition was in perfect agreement with the experimental results on planer gold substrate [64]. The surface of the planer gold is probably flatter than the surface of Mylar, but both of the surfaces are not periodic and belong to disordered substrates.

On graphite, an ordered substrate, the KT transition was observed for the third and higher layers of ^{4}He film, but the signature was not clear compared with on disordered substrates [34]. Moreover, so-called reentrant superfluidity was observed before the second layer completion at localized commensurate solid phase [34]. The reentrant superfluidity might be a quantum hexatic phase [38], an intertwined state of superfluid and density wave order [35], and it is currently studied in several research groups. The superfluidity on graphite is much more complex due to the periodicity and corrugation in the adsorption potential. The superfluidity on graphite is fascinating, but it does not mean that superfluidity on disordered substrates is boring: It is rather surprising that superfluid transition of on disordered substrate shows a perfect agreement with the KT theory.

On disordered porous glass substrate, ^{4}He film is locally two-dimensional, but the film connects three-dimensionally all over the pore wall. The superfluid density of ^{4}He film on Vycor obeys a power low

$$\rho_s(T) \propto (1 - T/T_c)^{\zeta}, \tag{1.9}$$

with an exponent $\zeta = 0.63 \pm 0.03$, which is close to $\zeta = 0.674 \pm 0.001$ in 3D bulk ^{4}He [5, 71, 72]. These values of the exponent mean that the superfluid density gradually increases below T_c, which is in contrast to the KT universal jump in Eq. (1.8). The bulk-like exponent in ^{4}He film on Vycor is because the coherence length in the temperature range of this power low region is much larger than the pore size [5]. A crossover from the KT to 3D character has been confirmed by a systematic experiment using Vycor-like porous glasses with different pore diameters from 5 to 1000 nm [73]. The crossover was also observed as a competition between the pore size and the coherence length as a function on temperature on bare and H_2-preplated porous gold with a pore diameter of 130 nm [74, 75].

A common feature in the superfluid onset on disordered substrates is that the superfluid phase appears only when the coverage n exceeds a critical coverage n_c. The superfluid transition temperature T_c increases as n increases from n_c. The critical coverage is typically corresponds to 2 atomic layers on porous glass [5], and it decreases by reducing the potential depth from the substrate down to 0.5 layers [63]. Figure 1.7 shows a generic coverage–temperature phase diagram of ^{4}He film on disordered substrate. The T_c curve bump against the coverage axis at $T = 0$ and $n = n_c$. The transition temperature at a coverage close to n_c obeys a power law

$$T_c \propto (n - n_c)^w. \tag{1.10}$$

Csáthy *et al.* [63] thoroughly investigated the effect of substrates to n_c and an n–T_c relation. They employed a torsional oscillator which contains a porous gold substrate, and coated the substrate with 4 layers of adsorbents to make "other substrates" such as H_2, Ne and Ar. The porous gold is an aggregate of interconnected gold strands (typical diameter $\sim$ 60 nm), and preplated with The critical coverage varies from 5.5 to 24.6 μmol/m^2, the former is for H_2 and the latter is for bare Au substrate. They found that n_c has monotonic dependence on the potential depth D and the binding energy E_b, which may be consistent with the inert layer model. The substrate effect on the critical coverages from other experiments, the graphite substrate [34, 39] or even "liquid ^{3}He layers" atop of the ^{4}He film [62], also fits well with the n_c–D and n_c–E_b sublinear scaling. They also found that the n–T_c relations on various substrates perfectly collapse on to a single curve by reducing the coverage axis to $f(n - n_c)$, where f is a substrate-dependent correction factor of order unity. The scaling at a coverage near n_c was

$$T_c \propto (n - n_c)^{1.6}. \tag{1.11}$$

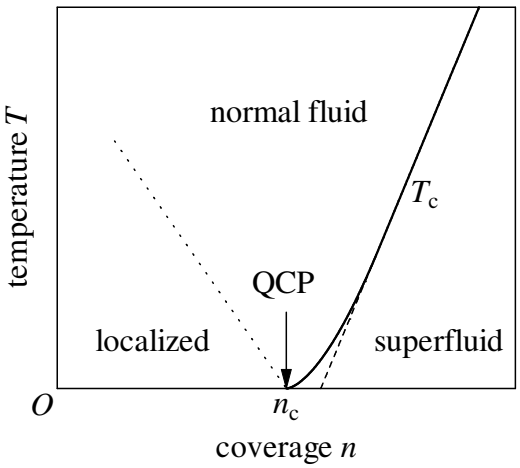

Figure 1.7: Generic phase diagram of ^{4}He film on a disordered substrate. The dashed line is an extrapolation of a linear n–T_c dependence at higher coverages. The film at higher temperature is a normal fluid. The film at $n < n_c$ and near $T = 0$ is an localized film, which is the target in this thesis.

The exponent 1.6 is consistent with previous studies [5, 7].

The localized phase, indicated in the lower left in Fig. 1.7, is the elusive phase. Following subsections are dedicated to previous attempts to unveil the nature of the localized phase.

1.3.2 Inert layer model

The case of $w = 1$ corresponds to the inert layer model. In this model, the film at a coverage $n < n_c$ is a solid layer due to strong van der Waals attraction from the substrate. The inert solid layer is completely localized and does not flow. If more ^{4}He atoms are added on top of the inert solid layer, the additional atoms are slightly distant from the substrate and feel weaker attractive force. Above a critical coverage n_c, the additional atoms are free from the strong surface attraction and can become superfluid below a finite T_c. In the superfluid phase, the superfluid overlayer and inert solid underlayer are distinct from each other. The superfluid density at $T = 0$ is

$$\rho_s(0) = n - n_c. \tag{1.12}$$

In the early stage of superfluid ^{4}He film studies in 1970s, the experimental results had been explained with this inert layer model [76, 77].

The inert layer model goes well with the fact that n_c scales with the potential

depth D of different substrates [63], but is inconsistent with many experimental results, such as the nonadditivity of the heat capacity [78, 63, 7]. The inert layer model does not consider the interaction among helium atoms.

1.3.3 Bose–Hubbard model

The Bose–Hubbard model is a standard model which describes strongly correlated spinless bosons in a lattice and the superfluid–insulator transition [6]. The model starts with a Bose–Hubbard Hamiltonian

$$\hat{H} = -J \sum_{\langle i,j \rangle} \hat{a}_i^\dagger \hat{a}_j + \frac{V}{2} \sum_i (\hat{n}_i - 1)\hat{n}_i - \sum_i (\mu + \delta\mu_i)\hat{n}_i, \tag{1.13}$$

where $\hat{a}_i^\dagger$ and $\hat{a}_i$ are the creation and annihilation operator of a boson at ith site, and $\hat{n}_i = \hat{a}_i^\dagger \hat{a}_i$ is the number operator. The first term in a hopping energy with $-J < 0$, where bosons favor to be in a superfluid ground state to minimize the energy. The second term is an onsite repulsion term that disfavors two or more atoms occupying the same site. The third term is a chemical potential with a disorder $\delta\mu_i$.

Mott insulator

In the situation $J = 0$ and $\delta\mu_i = 0$ (no hopping, no disorder), bosons localize and cannot move from site to site. When the particle number per site $\langle N \rangle$ is an integer number 1, 2, 3, ... (commensurate), the system is a Mott insulator. Even if we slightly increase J, the system remains Mott insulator because a boson cannot hop to the nearest occupied site due to onsite repulsion. But if we increase J further, the bosons condense into superfluid phase. This scenario can be seen from the phase diagram in Fig. 1.8.

If $\langle N \rangle$ is not an integer, bosons can hop with a very small but finite J. That is shown at the contours in Fig. 1.8 (a), penetrating the superfluid phase with $J > 0$. To increase the particle number is to increase the chemical potential μ. At $J = 0$, the chemical potential jumps from 0 to V when $\langle N \rangle$ increases across 1. At this jump, the compressibility is $\kappa = \partial n / \partial \mu = \infty$, therefore has infinite compressibility. But whenever $\langle N \rangle = 1, 2, 3, \ldots$, therefore in the Mott insulating phase, the compressibility is zero, $\kappa = 0$ (incompressible), with a finite energy gap $\Delta > 0$.

In realistic helium films, the hopping term is finite $J > 0$, and what we can change is μ by increasing $\langle N \rangle$. This suggests that we can experimentally trace a vertical dotted line in Fig. 1.8(a), whose starting point is at $J/V > 0$ and $\mu/V = 0$, already in the superfluid phase. Therefore, the Mott insulating picture in a strict sense does not answer the superfluid onset in ^{4}He film.

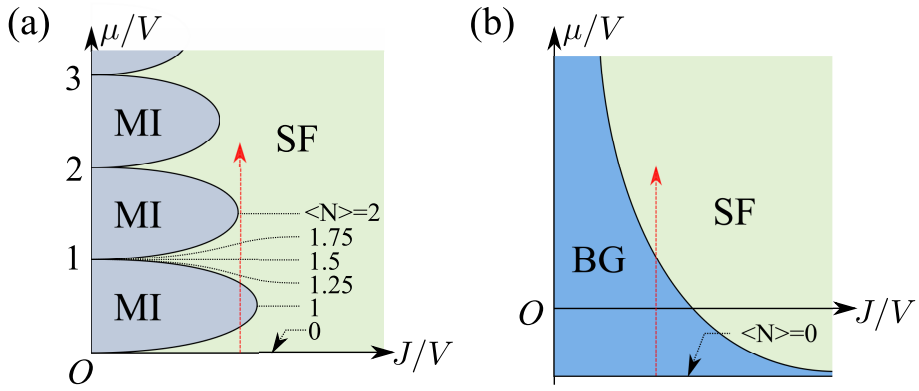

Figure 1.8: Phase diagrams in the Bose–Hubbard model (a) without disorder and (b) in the strong disorder limit, after Refs. [6, 7, 79]. MI: Mott insulator; BG: Bose glass; SF: superfluid. The black dotted curves in (a) are contours of constant particle number par site. Red arrows starting from $\langle N \rangle = 0$ are possible traces in ^{4}He films experiments.

Bose glass

With finite $\delta\mu_i$, the potential becomes disordered. The disorder lowers the limit of the chemical potential, and bosons favor to localize to deep potential sites. The jump in the chemical potential in the Mott insulator disappears by increasing the disorder, and the system becomes always compressible. The compressible and non-superfluid phase is called Bose glass. Non-zero compressibility implies that Bose glass is gapless with respect to particle-hole excitation.

Fisher *et al.* argued that the commensurate Mott insulating phase is destroyed in a strong disorder limit, and there are two phases, Bose glass and superfluid [6]. The phase diagram is shown in Fig. 1.8 (b). They predicted that the superfluid onset of ^{4}He film on a porous glass is the Bose glass–superfluid transition. The trace in Fig. 1.8 (b) does not conflict to the experimental situation that the superfluidity appears once the coverage n exceeds the critical coverage n_c.

The critical exponents of the Bose glass was theoretically studied by using a renormalization group theory [6]. The critical exponents from experiments of superfluid ^{4}He film, however, did not quantitatively agree with the predicted critical exponents of Bose glass [7]. It was also shown that thin ^{4}He film in a localized phase is *gapped* [7], which is contrary to the Bose glass model.

Table 1.5: Gap and compressibility in three phases.

Phase	Gap	Compressibility
Mott insulator	$\Delta > 0$, gapped (particle-hole)	$\kappa = 0$, incompressible
Bose glass	$\Delta = 0$, gapless (particle-hole)	$\kappa > 0$, compressible
Mott glass	$\Delta > 0$, gapped (single-particle)	$\kappa = 0$, incompressible

Mott glass

There exists another insulating phase, called Mott glass. Mott glass appears between Mott insulator and Bose glass when we appropriately tune the strength of the disorder and the amplitude of the commensurate potential [80]. The Mott glass phase is characterized by a single-particle gap and zero compressibility. The particle-hole gap is closed.

We see the properties of Mott insulator, Bose glass, and Mott glass in Table 1.5. I emphasize that the compressibility, or the elasticity, of the insulating phase is as much as important compared with the information of the excitations (gap).

1.3.4 Heat capacity measurements of thin films

Helium 4 film

Heat capacity measurement of thin ^{4}He film on Vycor by Tait and Reppy showed clear evidence that the film at $n < n_c$ is not an inert solid layer [81]. The heat capacity of ^{4}He film on Vycor at $n < n_c$ has roughly quadratic T-dependence at high temperatures, but drops rapidly at low temperatures, which is shown in Fig. 1.9. Above a characteristic temperature T_B (to distinguish this from the superfluid T_c, we use T_B after Ref. [7]), the heat capacity is fitted to

$$C = AT + BT^2, \tag{1.14}$$

where A is a coefficient for the linear term and B is for a quadratic term. The linear term is dominant, and is supported as a single-particle excitation of atom from a solid island to 2D gas. For low temperatures, $T < T_B$, Tait and Reppy [81] introduced a T–dependence of the heat capacity

$$C = D(\Delta/2k_BT + 2)e^{-\Delta/k_BT}, \tag{1.15}$$

from a thermal activation model, where D is a prefactor and Δ is an energy gap. This expression of heat capacity comes from an single-particle thermal excitation from localized to extended states. Atoms in the localized state are fixed to the substrate, and atoms the extended states can move along the substrate and acts as a

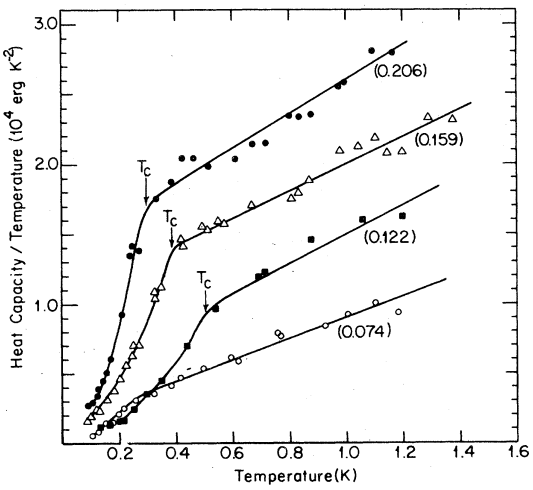

Figure 1.9: Heat capacity of thin ^{4}He films on Vycor divided by temperature as a function of temperature [81]. Numbers give the fractional filling $n/n_{\rm fp}$, where the critical coverage is $n_{\rm c} = 28.6\,\mu{\rm mol/m}^2$ and $n_{\rm c}/n_{\rm fp} = 0.337$, and $T_{\rm c}$ denotes $T_{\rm B}$ in the text. [Reprinted figure with permission from R. H. Tait and J. D. Reppy, Physical Review B **20**, 979 (1979). Copyright (1979) by the American Physical Society.]

normal fluid. Crowell *et al.* reexamined this temperature and coverage dependence of the heat capacity by Tait and Reppy [81], and argued that the localized ^{4}He film at $n < n_{\rm c}$ and $T < T_{\rm B}$ has a gap Δ, which does not agree with the gapless Bose glass model [7, 82].

The characteristic temperature $T_{\rm B}$ can be treated as a crossover temperature which separates the localized and mobile regime. It is dependent on n, and vanishes at or near the superfluid onset coverage $n_{\rm c}$. The physical interpretation for $T_{\rm B}$ is not clear: Is it a phase transition temperature?

On graphite, the phase transitions between 2D (commensurate or incommensurate) solid, 2D liquid, 2D gas and coexisting phases of those are characterized by a clear peak structure of the heat capacity [36, 37, 38]. Contrary to that, no evidence of the 2D phase transition has been found for ^{4}He on Vycor at $n < n_{\rm c}$ [81].

Helium 3 film

Contrary to ^{4}He films, studies of ^{3}He films on disordered substrates were few, since ^{3}He films show no superfluidity at currently available low temperatures. The heat capacity of ^{3}He film and the scaled one of ^{4}He film, as shown in Fig. 1.10, are essentially the same at high temperatures at similar coverages (10, 14 atom/nm^2).

However, the heat capacity of ^{3}He film at low temperatures is dominated by a contribution from nuclear spins [83, 84], contrary to the roughly exponential T–dependence in ^{4}He film. Therefore, the existence of gapped localized state was not clarified for ^{3}He films. The critical coverage for ^{3}He film was not identified.

Hydrogen film

Torii *et al.* [85] have measured the heat capacity of thin H_2 film in Vycor. A shown in Fig. 1.11, the heat capacity was parabolic, $C \propto T^2$, above a characteristic temperature, which is coverage-dependent, Below the characteristic temperature, the heat capacity abruptly decreases. They argued that the temperature dependence of the heat capacity of H_2 films is similar to that of ^{4}He film measured by Tait and Reppy [81] The coverage–temperature phase diagram is V-shaped (see for example Fig. 1.7), although the low temperature phase at a higher coverage is not superfluid in H_2 films. The breaking temperature T_B is at higher temperature than that of ^{4}He film; it is above 4 K at a low coverage. The similarity in the heat capacity suggests that there is a universal property between H_2 and ^{4}He on Vycor, which is probably related the localization of the films.

Neon film

Neon films have not been studied much: Past heat capacity studies suggested that submonolayer neon films on graphite have 2D solid and gas phases, and 2D solid-gas, solid-liquid, and liquid-gas coexisting phases [41, 86]. A phase diagram and heat capacity data for one coverage are shown in Fig. 1.12. A phase transition from a mobile (liquid-gas or solid-liquid) to a localized (solid-gas) phase occurs at about 14 K, at which the heat capacity shows a very sharp peak after proper annealing. Since these measurements were limited to rather high temperatures, quantum properties of neon films were not clarified. No systematic studies have been done for neon films on disordered substrates.

1.3.5 Slippage phenomenon in thin films

In several experiments [66, 87, 88], it is argued that thin ^{4}He and ^{3}He film anomalously slips on the substrates. The slippage phenomenon of ^{4}He and ^{3}He films on a Hectorite substrate appeared at a coverage less than the superfluid onset coverage, $n < n_c$, and disappears at $n = n_c$. In the ultrasound experiment [66, 87], the sound velocity is $v_0 = \sqrt{c/\rho_{sub}}$, where the elastic stiffness of the substrate c is constant, and the effective density ρ_{sub} is increased by helium adsorption. They observed a

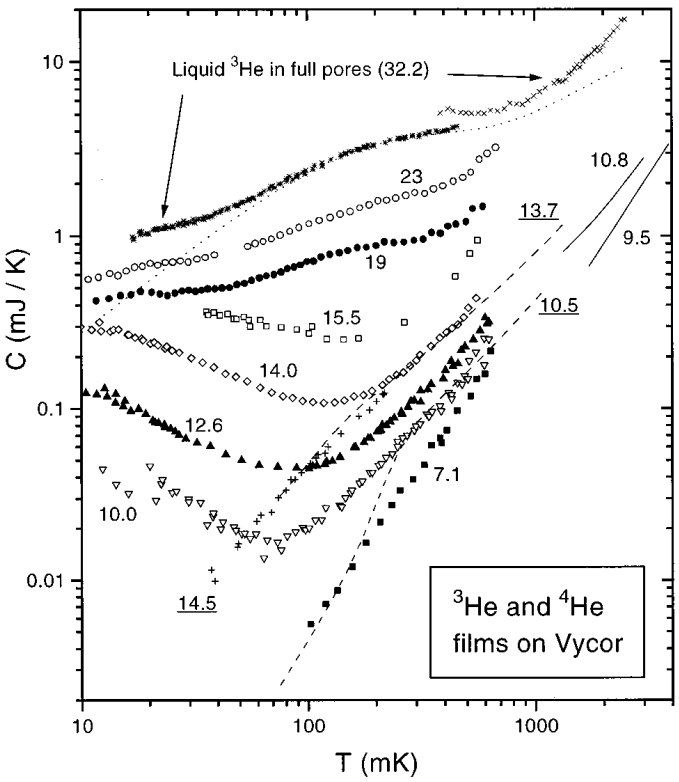

Figure 1.10: Heat capacity of ^{3}He film on Vycor as a function of temperature (up to a full-pore coverage) [84]. Numbers give the ^{3}He coverage in units of atom/nm^2 (= 1.66 μmol/m^2). Underlined numbers give the ^{4}He coverage in the same units. Lines and × data are from the previous studies, including Ref. [81] for the dashed lines. [Reprinted figure with permission from A. Golov and F. Pobell, Physical Review B **53**, 12647 (1996). Copyright (1996) by the American Physical Society.]

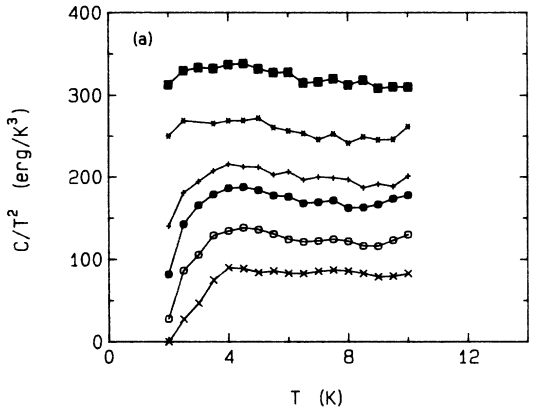

Figure 1.11: Heat capacity C of H_2 films on Vycor divided by T^2 as a function of temperature T [85]. The coverages are 3.2, 4.7, 6.0, 7.3, 8.6, 9.9 μmol/m^2 from bottom to top. [Reprinted figure with permission from R. H. Torii, H. J. Maris, and G. M. Seidel, Physical Review B **41**, 7167 (1990). Copyright (1990) by the American Physical Society.]

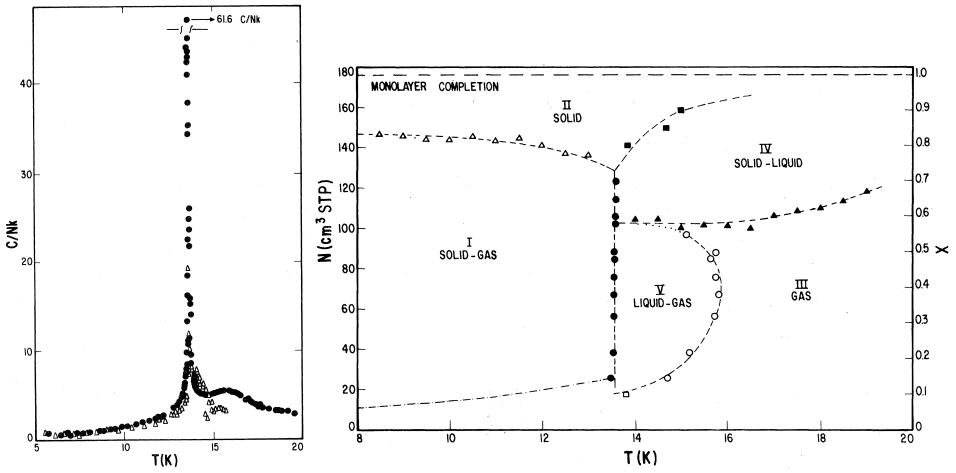

Figure 1.12: Heat capacity C (left) and a phase diagram (left) of monolayer Ne on graphite, where N is a coverage as a dosed gas volume at standard temperature and pressure, and X is a coverage to monolayer completion [41]. The C-data is at $X = 0.500$; △ before annealing; • after annealing. [Reprinted figure with permission from R. E. Rapp, E. P. de Souza, and E. Lerner, Physical Review B **24**, 2196 (1981). Copyright (1981) by the American Physical Society.]

sound velocity change and an excess attenuation which obey

$$\frac{\Delta v}{v_0} = \frac{\Delta\rho}{2\rho_{\rm sub}}\left[\chi + \frac{1}{1+(\omega\tau)^2}(1-\chi)\right], \tag{1.16}$$

and

$$\Delta\alpha = \frac{\Delta\rho\omega}{2\rho_{\rm sub}v_0}\frac{\omega\tau}{1+(\omega\tau)^2}(1-\chi). \tag{1.17}$$

This relaxation process is characterized by a relaxation time which obeys an Arrhenius relation,

$$\tau = \tau_0 \exp(E/k_{\rm B}T). \tag{1.18}$$

They fitted the data to the above equations, and obtained an attenuation peak temperature T^*, which may obey a power law

$$T^* \propto |n - n_{\rm c}|^a, \tag{1.19}$$

with $a < 1$.

Mohandas *et al.* [88] showed that submonolayer ^{4}He films on a Grafoil substrate slip at a few hundred mK. The study was done with a torsional oscillator with a resonant frequency of 1.2 kHz and at an amplitude of 200 nm, which is greater than a typical platelet size 10 nm of Grafoil [32]. The T dependence of their resonant frequency increment associated with a dissipation peak is consistent with those of Kogure *et al.* (see the next subsection) and the present results.

$$\delta Q^{-1} = \frac{A\omega\tau}{1+(\omega\tau)^2}, \tag{1.20}$$

$$\delta P = \frac{A'(\omega\tau)^2}{1+(\omega\tau)^2}, \tag{1.21}$$

with a single thermally activated relaxation time $\tau = \tau_0 e^{E/T}$ and an activation energy E in kelvin. Mohandas *et al.* found that E = 1–2 K while $\tau_0 = 2.5$ μs below registry and $E = (3.5 \pm 0.5)$ K while $\tau_0 = (7 \pm 2)$ μs in incommensurate solid.

1.3.6 Indication of stiffening phenomenon in thin films

The study in this thesis was motivated by an observation of anomalous frequency shift with excess dissipation in a torsional oscillator for the study of superfluid properties of ^{4}He films in porous Gelsil glass by Kogure *et al.* in our group [89]. Two torsional oscillators, which we refer to as TO1 and TO2, were employed as shown in Fig. 1.13. Each torsional oscillator contained a disk sample of porous Gelsil glass inside the torsion bob. In TO1, they glued all the faces of the glass

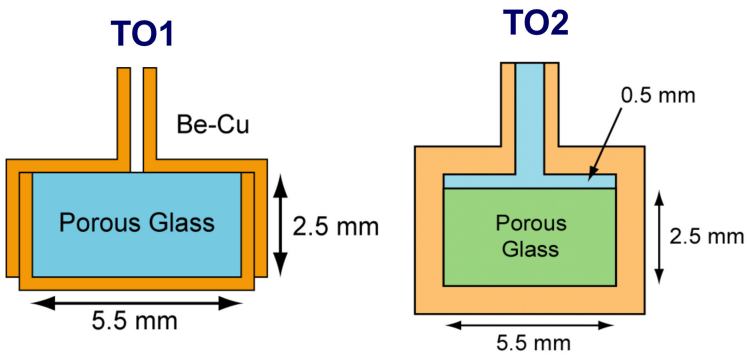

Figure 1.13: Schematic cross-sectional views of TO1 and TO2. The porous glass sample is glued to the BeCu enclosure with epoxy.

sample to the wall by Stycast 1266 epoxy. The epoxy penetrated to the hole of the torsion rod was carefully removed by inserting a drill bit. On the other hand, in TO2, there was an open space between the porous glass and one side of the wall of the bob, at which the torsion rod is attached.

Kogure *et al.* performed measurements of the resonant frequency f and dissipation Q^{-1} of TO1 and TO2 with adsorbed ^{4}He at $6 < n < 35$ μmol/m^2. In TO1, they observed a superfluid response at $n > n_c$ with $n_c = 22$ μmol/m^2 and also an anomalous behavior at $n < 22$ μmol/m^2. Figure 1.14 shows the results, which are converted to the normalized frequency shift $2\Delta f/f_0$ and excess dissipation ΔQ^{-1} by subtracting the background ($n = 0$) data from the finite coverage data. At $n > n_c$, the superfluid transition was observed as an increase in f below T_c. The sharp anti-crossing of Δf with a peak of Q^{-1} is third sound (surface wave in superfluid film) response. On the other hand, at $n < n_c$ where the ^{4}He film cannot be superfluid, f anomalously increases accompanying a dissipation peak. In TO2, however, such an anomaly below n_c was not observed, while the superfluid transition was seen at $n > n_c$ as in TO1.

Does this anomaly come from mass decoupling as in slippage phenomenon? Their answer is "probably not." They found that the absence of the anomaly in TO2 can originate from the existence of open space between the face of a porous glass disk and the wall of the torsional oscillator cell near the torsion rod. Takahashi calculated the change in resonant frequency when the shear modulus of glass inside the torsional oscillator bob increases, assuming the structures of TO1 and TO2 in finite element method (FEM) simulations. The results are shown in Fig. 1.15. When the shear modulus of glass inside TO1 increases 5 percent, f increases about 60 mHz, while it increases only 2 mHz in TO2.

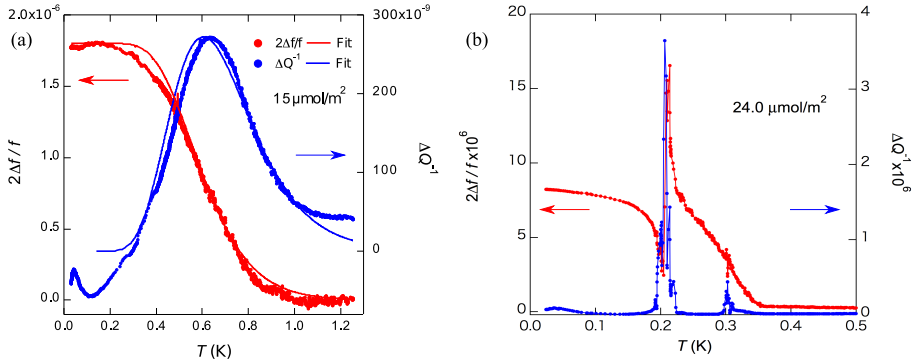

Figure 1.14: Resonant frequency shift and energy dissipation in TO1 with ^{4}He coverage (a) $n = 15$ μmol/m^2 and (b) 24.0 μmol/m^2. The data shown are after the subtraction of the background. Solid curves in (a) are the results of fitting for the "anomalous response." The superfluid transition temperature at 24.0 μmol/m^2 is $T_c = 0.35$ K, the temperature at which Δf suddenly increases.

They interpret these results as follows: In a realistic torsional oscillator made of metal for superfluid studies, the torsion bob is not rigid, and the resonant frequency of the fundamental torsional oscillation is determined not only by the shear modulus of the torsion rod but also by the shear modulus of the torsion bob, which consists of porous glass, BeCu enclosure and adsorbed helium in our experiments. This non-ideal nature of torsional oscillator has been established by studies of apparent supersolidity of bulk solid ^{4}He using torsional oscillators with many different designs [90, 91, 92]. In particular, it has been realized as an effect that the stiffness of the part of torsional oscillator near the torsion rod has a large contribution to resonant frequency [93]. The presence of the anomaly in TO1 and its absence in TO2 can be interpreted as a manifestation of this effect. In TO2, the stiffening of porous glass sample by helium adsorption will hardly contribute to the total torsion constant by the existence of open space inside the bob.

They analysed the anomaly with an anelastic response functions [94]

$$\frac{2\Delta f}{f} = \frac{\Delta G}{G_0}\left[1 - \int_0^\infty \frac{F(E)}{1+(\omega\tau)^2} dE\right], \tag{1.22}$$

$$\Delta Q^{-1} = \frac{\Delta G}{G_0}\int_0^\infty \frac{\omega\tau}{1+(\omega\tau)^2} F(E) dE, \tag{1.23}$$

which we will discuss in Chapter 3. Briefly, these functions describes a relaxational crossover between a high-temperature soft state and a low-temperature stiff state. These functions are essentially equivalent to Eqs. (1.16) (1.17) (1.20), and (1.21),

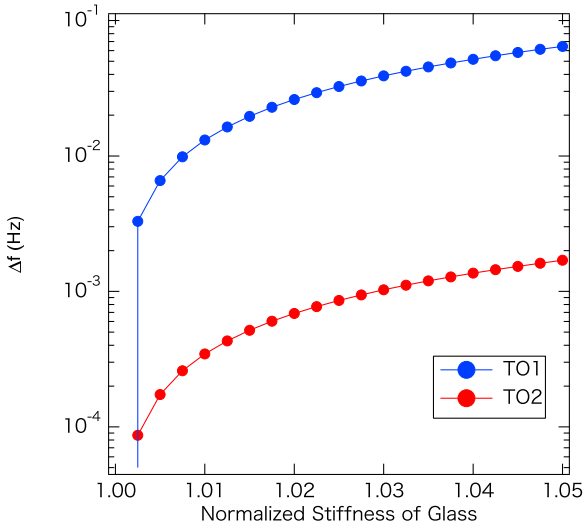

Figure 1.15: Resonant frequency shift of TO1 and TO2 as a function of normalized stiffness of porous glass sample, calculated by the FEM simulations by Takahashi. The resonant frequency shift of TO1 is 40 times larger than that of TO2.

except that Kogure *et al.* introduced a distribution $F(E)$ of the energy gap E. The fitting of the data to the response functions works well, as shown in Fig. 1.14.

The dissipation-peak temperature T_p and the superfluid transition temperature T_c are plotted in Fig. 1.16. The critical coverages n_c determined from the n dependences of T_p and T_c are identical within the accuracy of the data. These results indicate that ^{4}He film on a porous glass exhibit an elastic anomaly, and undergoes a quantum phase transition from the stiff to superfluid phase by increasing the coverage n. There still remains, however, a possibility of slippage phenomenon: The observed frequency shift in the anomaly was an order of magnitude smaller than that in the superfluid mass decoupling. Therefore, the increase in f in the anomaly can be explained as a mass decoupling of a part of the film.

1.4 Scope of this thesis

In this thesis, I focus on the following issues:

1. Clarify that the observed anomaly of thin ^{4}He film in Sect. 1.3.6 originates from an effect of elasticity.

2. Identify the phase of the localized molecular films.

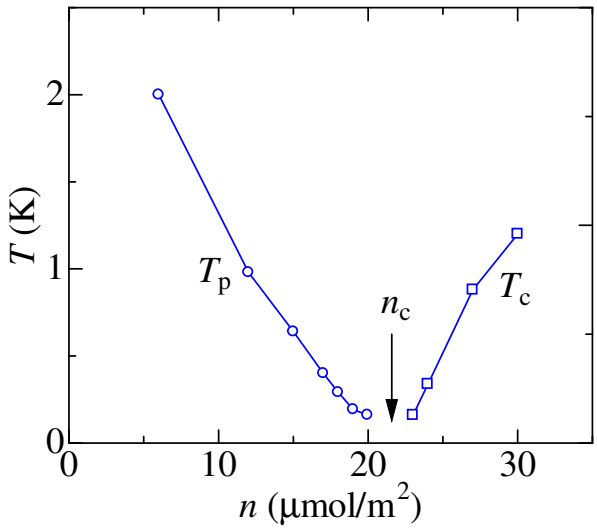

Figure 1.16: Dissipation peak temperature T_p and superfluid transition temperature T_c of ^{4}He film detected with TO1. The arrow is at $n = 21.6$ μmol/m^2.

3. Discover common elastic properties in thin films.

For these purposes, I used a new torsional oscillator which can directly measure the elastic constant of adsorbed films on porous glass substrate. I used the sample gases of pure ^{4}He, ^{3}He, Ne, H_2, HD, and D_2 for comparison of the effect of quantum properties, quantum statistics, and mass.

The design and method of the torsional oscillator are given in Sect. 2.1. The torsional oscillator was first designed and fabricated by my coworker Michihiro Tagai, and modified by him and the author after a test run. The ^{4}He and ^{3}He experiments were done by the author and Tagai. The Ne, HD, H_2 and D_2 experiments were done by the author and partially by Katsuyuki Yamashita. Every work in this thesis was supervised by Prof. Keiya Shirahama.

Chapter 2

Experimental Apparatus

We used a specially designed torsional oscillator, a dilution refrigerator, and a gas-handling system for the elasticity measurements of adsorbed films. Here I describe the details of the apparatus, and measurement procedures in the helium, neon and hydrogen experiments.

2.1 Torsional oscillator: The experimental cell

2.1.1 Brief background

A number of properties of superfluid ^{4}He and ^{3}He have been investigated by torsional oscillator experiments. A modern torsional oscillator technique was developed by Reppy and coworkers [5, 71]. They embedded a sample space for helium in a torsion bob, and made a cylindrical torsion rod of a piece of machined metal. The bob can oscillate with twisting the rod, and it has an eigenfrequency for the torsional oscillation. The resonant frequency is given by $f = (1/2\pi)\sqrt{k/I}$, where I is a moment inertia (mass) of the bob and k is a torsion constant (stiffness, spring constant) of the rod. The rigid construction enabled to measure the resonant frequency (of the order of 1 kHz) in very high resolution with good stability. When liquid helium in the bob becomes superfluid, the superfluid does not participate in the torsional motion so that the moment of inertia effectively decreases by a small amount, $I \rightarrow I - \delta I$ with $I \gg \delta I > 0$. The resonant frequency shift after the superfluid transition is $\delta f = f\delta I/2I$, typically more than 1 mHz, which is detectable in a good resolution. The superfluid transition is observed as a sudden rise of the resonant frequency when lowering the temperature over the transition temperature.

The torsional oscillator technique was so useful and trusted that it was employed for the search of *supersolidity* in solid ^{4}He. Supersolid is a quantum solid in

which atoms or vacancies move without friction simultaneously with conserving the translational symmetry of the crystal. In experimental studies published in 2004 [90, 95], the rise of the resonant frequency was indeed observed in solid ^{4}He, which the authors had claimed to be a discovery of the supersolid. But these observations were proved to be a fake response which was originated from the increase in elasticity of solid ^{4}He [96]. Since then, it is recognized that the stiffening of the solid inside the torsional oscillator bob increases the resonant frequency especially when the solid is near the root of the rod [92, 93].

In mechanical oscillation measurements such as torsional oscillator, quartz-crystal microbalance and ultrasonic measurement, it is a difficult issue to separate the effect of mass decoupling from the effect of elasticity change because the resonant frequency or sound velocity is always proportional to $\sqrt{(\text{stiffness})/(\text{mass})}$ of the substance. In many previous experiments of helium films, researchers attributed the change in frequency (velocity) to the change only in mass. Some researchers claimed that their observations of increase in the frequency are attributed as mass decoupling due to *slippage* phenomenon of atoms in conditions that superfluidity never appears [87, 88], without consideration of the elastic effect.

In Keio University, Shirahama and coworkers investigated the emergent phases of film, liquid and solid ^{4}He in a porous Gelsil glass [49, 50, 51]. Using two torsional oscillators which have Gelsil inside the bobs, they have observed an anomalous response of ^{4}He film at a coverage below the critical coverage of superfluid onset *only in one* torsional oscillator [89], which was described in Chapter 1. The anomalous response resembles exactly the fake response of "supersolid ^{4}He", and the torsional oscillator in question has the Gelsil near the root of the rod. Therefore, there appeared a plausible explanation that ^{4}He film at $n < n_c$ exhibit a change in elastic anomaly. A numerical simulation by Takahashi also supported this idea. The problem is, again, that they could not separate the effect of mass and elasticity, and there remained a possibility of mass decoupling.

In the present work, we fabricated a torsional oscillator which is sensitive to the elasticity change but not to the mass decoupling. I made numerical simulations to quantitatively elucidate the effect of elasticity and mass to the resonant frequency. We have succeeded to measure the elasticity of a few layers of adsorbed atoms with a reliable method. Our torsional oscillator was used in the elasticity measurement of not only helium films but also hydrogen and neon films.

2.1.2 Torsional oscillator design for elasticity measurement

The resonant frequency of the torsional mode is given by

$$f = \frac{1}{2\pi}\sqrt{\frac{k}{I}}, \tag{2.1}$$

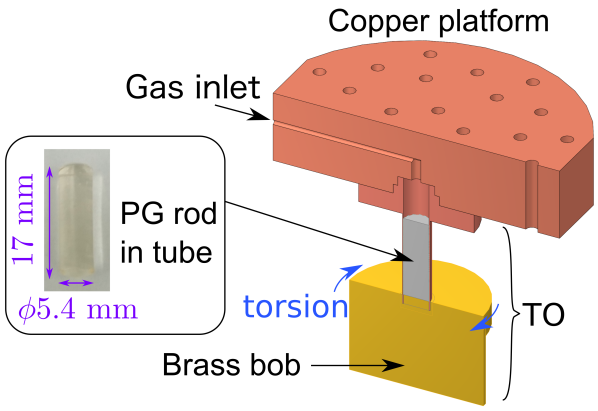

Figure 2.1: Cross-sectional view of the torsional oscillator (TO). The brown part is made of copper or beryllium copper, and the yellow is of brass. The photograph shows a rod-shaped porous Gelsil glass (PG).

where k is the torsion constant (stiffness) of the rod, and I is the moment of inertia of the bob. In conventional torsional oscillators, k is constant and I varies by mass decoupling. To measure the elasticity, we changed the location of the sample from inside the bob to inside the rod. As shown in Fig. 2.1, our torsional oscillator has a Gelsil sample inside a torsion rod of thin metal tube. The Gelsil is as a substrate for adsorption of atoms. There were a few experiments that employed torsional oscillators which have sample space inside the rods. Hollow-rod type torsional oscillators [91, 97] and a Vycor rod one [98] were used to measure the elasticity of solid ^{4}He confined in them. We succeeded in measuring the elasticity of thin films by using such a design of torsional oscillator with reliable sensitivity and stability.

2.1.3 Characterization of the porous Gelsil glass

Gelsil is a mesoporous silica (SiO_2) glass manufactured by sol-gel method. The pores are three-dimensionally connected. The pore structure is considered to be similar to that of Vycor [48], which is widely used in many superfluid helium studies. Adsorbed atoms form a film on the pore wall, and the atoms in fluid state can move along the wall.

The Gelsil sample used in this work is cylindrical shape, as shown in Fig. 2.1. The length is 17 mm, and the diameter is (5.4 ± 0.1) mm. The errors are from unevenness of the sample. The nominal pore diameter reported by manufacturer is 2.5 nm.

Before the insertion of the Gelsil into the torsional oscillator rod, we have made

Table 2.1: Measured properties of the Gelsil sample.

Property	Value	Method
Length L	17 mm	Caliper
Diameter D	(5.4 ± 0.1) mm	Caliper
Volume v	(0.39 ± 0.02) cm^3	$v = \pi D^2 L/4$
Mass m_{g0}	0.3713 g	Electronic balance
Density ρ_{g0}	0.954 g/cm^3	Mass/Volume
Surface area S	166 m^2	BET method
Mean pore diameter $\bar{d}$	4.4 nm	BET method
Peaked pore diameter d_p	3.9 nm	BJH method
Pore volume v_{pore}	0.184 cm^3	BJH method
Porosity p	0.54	BJH method

characterizations by nitrogen adsorption. The Gelsil sample was baked at 150 °C in vacuum for 3 hours to eliminate adsorbed impurities, especially water. The mass after the baking was 0.371 g, which gives a density $\rho_{g0} = 0.954$ g/cm^3 with the measures above. Then we took a nitrogen adsorption–desorption isotherm at 77 K for surface characterization by using BELSORP-miniII [99]. The result is shown in Fig. 2.2(a). The hysteresis loop of adsorption and desorption is Type IV in Brunauer–Deming–Deming–Teller (BDDT) classification [1], which is typical of the mesoporous material with cylindrical pores and looks very similar to the isotherm on Vycor [52]. A surface area analyzed with Brunauer–Emmett–Teller (BET) method [100] is 166 m^2 (447 m^2/g). The BET plot is shown in Fig. 2.2(b). A pore diameter distribution, analyzed with Barrett–Joyner–Halenda [101] method, has peaks of adsorption and desorption data at 3.9 nm, as shown in Fig. 2.2(c). The measured pore diameter 3.9 nm is larger than the nominal pore diameter 2.5 nm by manufacturer. The pore diameter distribution of the desorption data looks similar to the that of Vycor [48]. The parameters obtained are tabulated in Table 2.1.

Here we prepare useful quantities in Table 2.2. On disordered substrates, coverage and density are well defined quantities, but layer is not. However, the concept of layer is useful to have atomic scale picture of adsorbed films. Given a molar volume of adsorbate v_m, we can estimate a monolayer coverage. Considering simply a continuum of molecules, the monolayer coverage is

$$n_1 = (v^2 N_A)^{-1/3}. \tag{2.2}$$

Considering a close-packed structure for bulk and a triangular lattice for two-dimensional monolayer, and also lattice constants are common, the monolayer

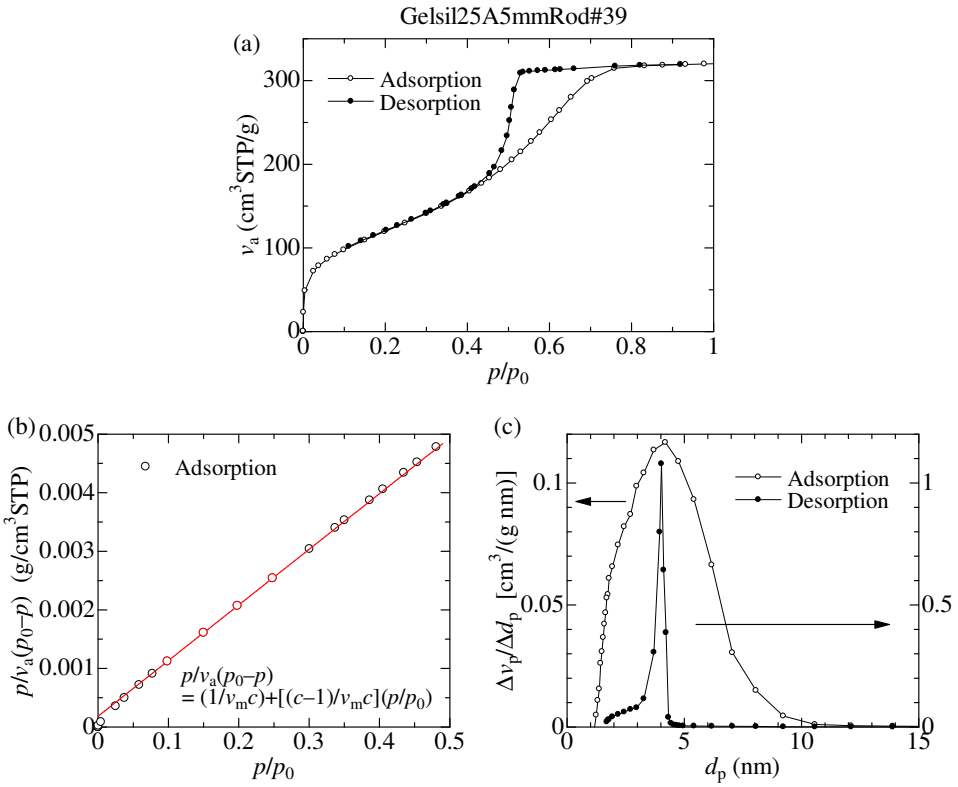

Figure 2.2: (a) Nitrogen adsorption and desorption isotherm of the Gelsil sample at 77 K. The abscissa is a pressure over saturated vapor pressure, and the ordinate is the amount of adsorbed nitrogen divided by the sample mass. (b) BET plot. The solid red line is a linear fit to the red open circles within the range $0.1 < p/p_0 < 0.3$, and the slope and the intercept give the monolayer adsorption volume v_m ($\propto S$) and $c = 53$. (c) Pore diameter distribution analyzed by BJH method. The abscissa is the pore diameter and the ordinate is the pore volume distribution. The curve from adsorption data gives indeed the pore distribution, and the peak from desorption data gives the bottleneck pore diameter.

Table 2.2: Estimated monolayer coverage n_1 using Eq. (2.2), monolayer thickness d_1, and full-pore coverage n_{fp} using Eq. (2.4),.

	v_{m} (cm^3/mol)	n_1 (μmol/m^2)	d_1 (Å)	n_{fp} (μmol/m^2)
^{3}He	36.84	10.70	3.940	30.1
^{4}He	27.58	12.97	3.578	40.2
H_2	23.30	14.52	3.382	47.6
HD	21.84	15.16	3.310	50.8
D_2	20.58	15.77	3.245	53.9
Ne	14.19	20.20	2.867	78.3

coverage is

$$n_1 = \frac{1}{2\sqrt{3}} \left(\frac{4\sqrt{2}}{v\sqrt{N_{\mathrm{A}}}} \right)^{2/3} \simeq 0.916 (v^2 N_{\mathrm{A}})^{-1/3}. \tag{2.3}$$

The prefactor in the latter equation is almost unity, therefore we use Eq. (2.2) for simplicity. A monolayer coverage might actually be larger than these naive estimations because the density of the first two layers is higher than that of bulk at zero pressure due to van der Waals attraction from the substrate.

A full-pore coverage is defined as a coverage at which the pore is fully filled with the molecules. It is estimated from a mole needed to fill the pore per surface area S (in m^2), so that

$$n_{\mathrm{fp}} = \frac{m_{\mathrm{g0}} v_{\mathrm{pore}}}{S v_{\mathrm{m}}}, \tag{2.4}$$

where the inverse of molar volume $1/v_{\mathrm{m}}$ is a mole per volume (in mol/cm^3), and $m_{\mathrm{g0}} v_{\mathrm{pore}}$ is the total pore volume of the porous glass (in cm^3). Calculated monolayer coverage n_1 and full-pore coverage n_{fp} are listed in Table 2.2.

2.1.4 Assembly of the torsional oscillator

After the pore characterization described above, the porous Gelsil glass was again baked at 150 °C in vacuum for 6 hours. Then it was glued with Stycast 1266 epoxy to an inner surface of a metal tube in a ^{4}He atmosphere The metal tube is as a support of the Gelsil rod to maintain the stability and rigidity, and we chose beryllium copper as the material because it has large thermal conductivity and high stability for the torsional oscillator experiment. The metal tube was machined from a single piece of beryllium copper and was tempered at 315 °C in vacuum for 3 hours to increase the elastic modulus. The outer and inner diameters of the tube are 6.0 and 5.5 mm, respectively.

The brass dummy bob is also glued to the tube with Stycast 1266 with a thin paper between the two to guarantee the electric insulation. The brass dummy bob serves as an electrode which was biased with dc voltage V_B during measurements. The electric contact from a coaxial cable to the dummy bob electrode was maintained by a thin gold wire (ϕ 0.025 mm) glued with Dotite silver colloid. The torsional oscillator was mounted on a torsional vibration isolator consisting of a massive copper platform with large rotational moment of inertia (70 mm ϕ , 30 mm thick) and a copper torsion rod (5 mm ϕ , 30 mm long). Two brass electrodes, which are for driving and detecting the torsional oscillation, are located on the platform so as to form two parallel plate capacitors with the flat faces of the dummy bob. The whole torsional oscillator setup was attached to the gold-preplated copper plate under a mixing chamber of a Joule–Thomson cooled dilution refrigerator [102].

Finite element method simulation

We performed FEM simulations to compute the resonant frequency shift of the torsional oscillator by the effective change of the elastic constant or the density in the Gelsil sample due to the adsorption of molecules. For this purpose, a computer-aided design (CAD) tool [103] and a FEM simulation software [104] were used. We treat the Gelsil rod as a continuous material with a Young's modulus E = 17.1 GPa and a Poisson's ratio $\nu = 0.155$, which were estimated from a ultrasound measurement [105].

The calculated resonant frequency by FEM was f = 962 Hz, which is 11% larger than the actual measured value f = 860 Hz at 4 K. The origin of this difference is not known. One possible reason is that the inhomogeneity of silica structure in the Gelsil sample. The normalized resonant frequency shift $2\delta f/f_0$, however, is a good quantity to compare the measured value to the FEM result.

We define the apparent shear modulus and density of the Gelsil by $G_g = G_{g0} + \delta G_g$ and $\rho_g = \rho_{g0} + \delta\rho_g$. The subscripts g0 denotes the value of the Gelsil at $n = 0$ (without adsorbed film). We actually changed the Young's modulus in the FEM simulations, and $\delta E_g/E_{g0} = \delta G_g/G_{g0}$. The results of the FEM simulations are shown in Fig. 2.3. The frequency shifts for small $\delta G_g/G_{g0}$ and $\delta\rho_g/\rho_{g0}$ in reasonable ranges are well fitted by linear functions,

$$\frac{2\delta f}{f_0} = 1.97 \times 10^{-1} \frac{\delta G_g}{G_{g0}}, \tag{2.5}$$

and

$$\frac{2\delta f}{f_0} = -1.33 \times 10^{-4} \frac{\delta\rho_g}{\rho_{g0}}. \tag{2.6}$$

Table 2.3: Estimated density and frequency shifts at the full-pore adsorption.

	$\delta\rho_g(n_{fp})/\rho_{g0}$	$2\delta f/f_0$
^{3}He	0.0406	-5.40×10^{-6}
^{4}He	0.0720	-9.58×10^{-6}
H_2	0.0429	-5.71×10^{-6}
HD	0.0686	-9.12×10^{-6}
D_2	0.0971	-1.29×10^{-5}
Ne	0.706	-9.39×10^{-5}

The effect of elasticity is larger than that of mass loading by a factor of 10^3 in our torsional oscillator. In a conventional torsional oscillator which has a porous glass inside the bob, it is estimated that $2\delta f/f_0 = \delta I/I_0 \sim 10^{-1}\delta\rho_g/\rho_{g0}$, where $I = I_0 + \delta I$ is the moment of inertia of the bob, and the prefactor is because the porous glass should be inside a container which also contributes to I (therefore $\delta I/I_0 < \delta\rho_g/\rho_{g0}$). For the torsional oscillators in Sect. 1.3.6, we can estimate from Fig. 1.15 that $2\delta f/f_0 \sim 10^{-3}\delta G_g/G_{g0}$ and $\sim 10^{-4}\delta G_g/G_{g0}$ for TO1 and TO2, respectively. Comparing the prefactors, we confirm that our torsional oscillator is special for detecting the elastic change of the sample.

We assume that the elasticity of the adsorbed film and the Gelsil are additive. The densities of the adsorbed film and the Gelsil are obviously additive. The total mass of adsorbed molecules is $mN_A nS$, where m is the mass of a molecule (in kg in the SI). Therefore, the density change upon the adsorption of molecules is estimated to be

$$\frac{\delta\rho_g(n)}{\rho_{g0}} = \frac{mN_A nS}{m_{g0}}. \tag{2.7}$$

The effective change in the density due to full-pore adsorption is tabulated in Table 2.3.

2.1.5 Forced torsional oscillation with damping

The equation of torsional motion of the torsional oscillator is

$$I\ddot{\phi} + \Gamma\dot{\phi} + k\phi = N, \tag{2.8}$$

where ϕ is the twisted angle between the root and the tip of the rod, Γ is a damping coefficient, and N is an applied torque. The coefficients I and k are described earlier, the moment of inertia of the bob and the torsion constant of the rod. Let us use from now a normalized form of Eq. (2.8),

$$\ddot{\phi} + \gamma\dot{\phi} + \omega_0^2\phi = n, \tag{2.9}$$

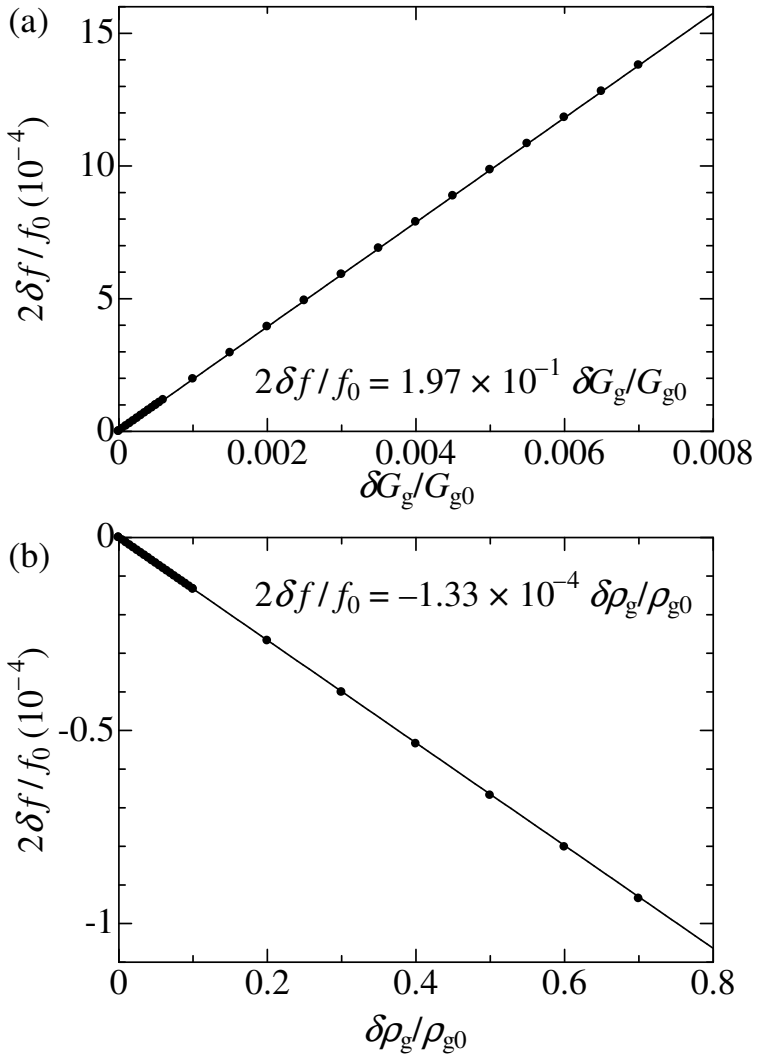

Figure 2.3: Normalized resonant frequency shift due to changes in (a) the shear modulus and (b) the density of the porous glass simulated by FEM. Lines are linear fittings.

where $\gamma \equiv \Gamma/I$, $\omega_0^2 \equiv k/I$, and $n \equiv N/I$.

We apply a torque $n = n_0 e^{i\omega t}$ with an angular frequency ω, and write $\phi = \phi_0 e^{i\omega t}$. The solution of Eq. (2.9) is

$$\phi_0 = \frac{n_0}{\omega_0^2 - \omega^2 + i\omega\gamma}. \tag{2.10}$$

When the damping is small (the Q factor is large) as in the usual torsional oscillator technique (including our torsional oscillator), $\omega_0 = \sqrt{k/I}$ is the resonant angular frequency at which $|\phi_0|$ takes its maximum. We write $\phi_0 = |\phi_0| e^{i\theta}$, where θ is a relative phase between n and ϕ. For $\omega \ll \omega_0$, $\theta = 0$. At $\omega = \omega_0$, $\theta = -\pi/2$. For $\omega \gg \omega_0$, $\theta = -\pi$.

We can describe that

$$\phi_0 = n_0 \frac{(\omega_0^2 - \omega^2) - i\gamma\omega}{(\omega_0^2 - \omega^2)^2 + (\gamma\omega)^2}. \tag{2.11}$$

Here we write $\omega = \omega_0 + \Delta\omega$ with $|\Delta\omega| \ll \omega_0$ and $\gamma \ll \omega_0$, and get a Lorentzian function

$$\mathrm{Im}(\phi_0) = n_0 \frac{-\gamma/\omega_0}{(2\Delta\omega)^2 + \gamma^2}. \tag{2.12}$$

It is now clear that γ is the full width at half maximum. The Q factor is $Q = \omega_0/\gamma$, which we introduce from the definition later. In torsional oscillator technique, typical values are of the order of $Q = 10^5$–10^6, and we confirm the abovementioned condition $\gamma \ll \omega_0$ was fulfilled.

2.1.6 Two parallel capacitors for drive and detection

The torque is applied electrostatically. As described earlier, the torsional oscillator has a moving biased electrode (B) on the bob which moves in torsional oscillation and two fixed electrodes for the drive (D) and pickup (P). A schematic view is shown in Fig. 2.4. The faces of the fixed electrodes are designed similarly, a circle of 11 mm in diameter for each. To calculate the displacement, velocity and applied strain, we have measured parameters below: The capacitance between the drive and bias electrodes $C_\mathrm{D} = 6.6686$ pF at 4 K, between the pickup and bias $C_\mathrm{P} = 10.1055$ pF at 4K, the area of the parallel plate capacitor $S = 95$ mm^3 (common to D-B and P-B), the arm length from the torsion axis to the center of the drive and pickup electrode $l = 12.5$ mm (common).

We calculate the distance between the parallel plates, d_D and d_P, from $C = \varepsilon_0 S/d$, where ε_0 is the electric constant. We have set C so that d is approximately 0.1 mm.

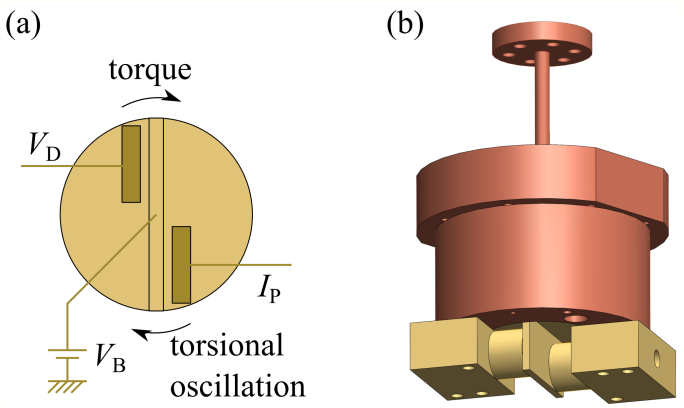

Figure 2.4: (a) Bottom view of a moving electrode and two fixed electrode for the drive and pickup. (b) 3D view of the torsional oscillator.

Now we calculate the torque N. The moving electrode is biased with dc voltage at $V_B = 200$ V. A drive voltage V_D, which is ac or pulse with much smaller amplitude than V_B, is applied to the fixed drive electrode. Then the potential energy stored is $U = C_D(V_B - V_D)^2/2$. Considering virtual displacement, the torque is given by

$$N = -l\frac{\partial U}{\partial d_D} = \frac{l(V_B^2 - 2V_BV_D + V_D^2)C_D^2}{2\varepsilon_0 S}. \tag{2.13}$$

The term including V_B^2 is a constant torque, therefore we omit it from now. As the term including $2V_BV_D$ is typically 100 times larger than the term including V_D^2 in time-average, we can ignore the latter. Thus we have

$$N = -\frac{2lV_BV_DC_D^2}{2\varepsilon_0 S}. \tag{2.14}$$

We measure the current I_P flows into the pickup electrode due to the capacitive change from the oscillation. The electric potential between the pickup and moving biased electrode is V_B. As the distance between the parallel plates changes due to the oscillation,

$$d_P(t) = d_{P0} - l\phi_0 e^{i\omega t}, \tag{2.15}$$

with $|l\phi_0| \ll d_{P0}$, the capacitance $C_P = \varepsilon_0 S/d_P$ changes, the charge $Q = C_PV_B$ changes, and the current $I_P = dQ/dt$ flows. Therefore, we have

$$I_P = i\frac{V_BC_P^2\omega l\phi_0}{\varepsilon_0 S}e^{i\omega t}. \tag{2.16}$$

2.1.7 Drive voltage in sine wave

When we apply an alternative voltage $V_{\mathrm{D}} = V_{\mathrm{D}0}e^{i\omega t}$ to the drive electrode, the torque is, from Eq. (2.14),

$$N = -\frac{lV_{\mathrm{B}}V_{\mathrm{D}0}C_{\mathrm{D}}^2}{\varepsilon_0 S}e^{i\omega t}. \tag{2.17}$$

Assigning this into Eq. (2.10), we have a twisted angle

$$\phi_0 = -\frac{lV_{\mathrm{B}}V_{\mathrm{D}0}C_{\mathrm{D}}^2}{\varepsilon_0 SI(\omega_0^2 - \omega^2 + i\omega\gamma)}e^{i\omega t}. \tag{2.18}$$

Combining Eqs. (2.16) and (2.18), we finally get

$$I_{\mathrm{P}} = -i\frac{\omega V_{\mathrm{D}0}(V_{\mathrm{B}}C_{\mathrm{D}}C_{\mathrm{P}}l)^2}{(\varepsilon_0 S)^2 I(\omega_0^2 - \omega^2 + i\omega\gamma)}e^{i\omega t} \xrightarrow[\omega=\omega_0]{} -\frac{V_{\mathrm{D}0}(V_{\mathrm{B}}C_{\mathrm{D}}C_{\mathrm{P}}l)^2}{(\varepsilon_0 S)^2 I\gamma}e^{i\omega_0 t}. \tag{2.19}$$

The drive voltage V_{D} and the pickup current I_{P} are in opposite phase at the resonance.

2.1.8 Drive voltage in pulse

To drive the torsional oscillator at the resonance in the experiments, we assembled a feedback loop circuit, which is shown in Fig. 2.5. A rectangle function for drive with an amplitude $V_{\mathrm{D}0} = 1.5$ V and a width $w = 50$ μs is applied to the fixed drive electrode, and the torque is applied to the torsional oscillator bob electrode. The torsional oscillator bob oscillates at the eigenfrequency (resonant frequency) f. A sinusoidal current I_{p} flows from the fixed pickup electrode and we measure its amplitude R (in ampère) with a lock-in amplifier. The monitor-out signal from the lock-in amplifier passes through a band-pass filter set at the resonant frequency, and it goes into the zero-cross detector. The zero-cross detector amplifies the signal until saturation, and generate a square wave at f (with an opposite phase). The square wave is separated to a reference signal of the lock-in amplifier, a frequency counter, and the function generator as a trigger for the next pulse. I set a delay time time for the trigger so as to maximize the pick-up current amplitude. The time constant of the lock-in amplifier was set at 3 s, and the integration time for frequency counting was 60 s. The signals were monitored with a oscilloscope. The monitor of the oscilloscope is schematically shown in Fig. 2.6.

As the Q factor is sufficiently large, the torsional oscillator oscillates in a sinusoidal manner even when the applied torque is pulsed. This is what one experiences on a swing, where a parent pushed the back of their child and the child swings sinusoidally. To convert our above calculations for the sinusoidal drive

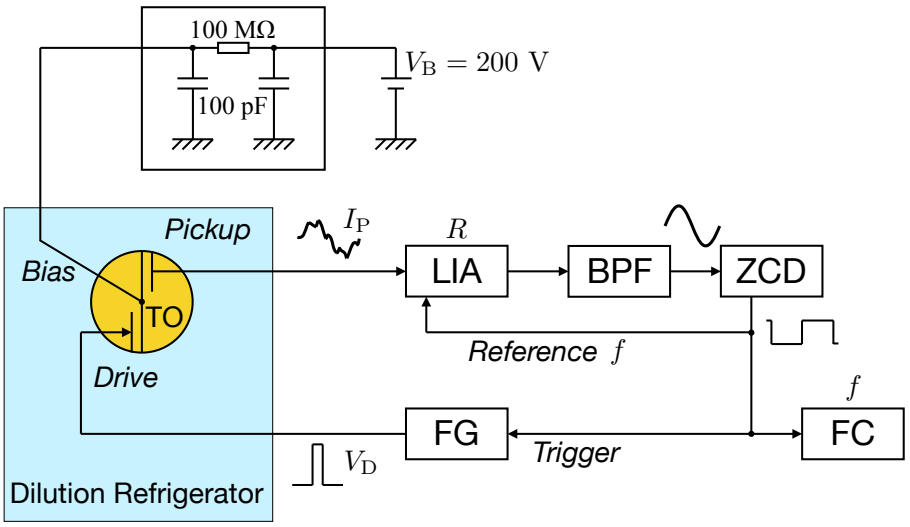

Figure 2.5: Loop circuit for driving the torsional oscillator at the resonance. TO: torsional oscillator; LIA: lock-in amplifier; BPF: band-pass filter; ZCD: zero-cross detector; FC: frequency counter; FG: function generator.

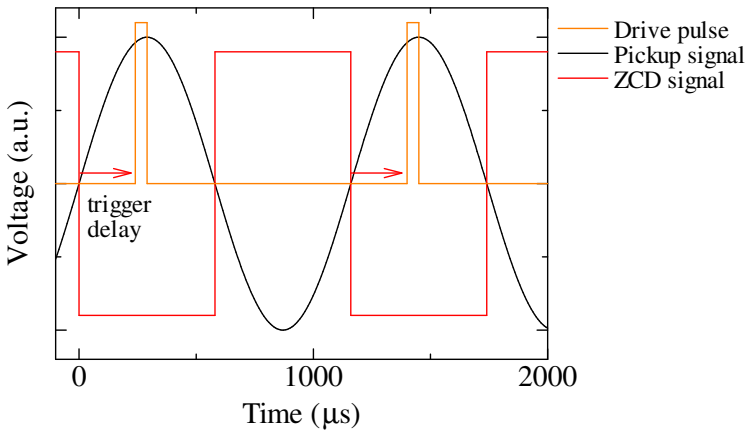

Figure 2.6: Oscilloscopic representation of the filtered pickup current, the zero-cross detector signal, and the drive pulse.

voltage to the pulsed one, we compare the energy. We assume that the twisted angle of the torsional oscillator rod ϕ_0 does not decay in a period of cycle P. The torque at a sinusoidal drive $V_{\rm D0}\cos(\omega_0 t)$ is

$$N \simeq \frac{lV_{\rm B}V_{\rm D0}C_{\rm D}}{\varepsilon_0 S}\cos(\omega_0 t). \tag{2.20}$$

At the resonance,

$$\phi = \phi_0 \sin(\omega_0 t), \tag{2.21}$$

and

$$d\phi = \phi_0\omega_0 \cos(\omega_0 t)dt. \tag{2.22}$$

The energy stored during a period $P = 1/f = 2\pi/\omega$ is

$$E_{\rm sinus} = \int N d\phi = \int_0^P \frac{lV_{\rm B}V_{\rm D0}C_{\rm D}}{\varepsilon_0 S}\phi_0\omega_0\cos^2(\omega_0 t)dt = \pi\frac{lV_{\rm B}V_{\rm D0}C_{\rm D}\phi_0}{\varepsilon_0 S}. \tag{2.23}$$

On the other hand, the energy stored by one pulse is calculated as follows. We set the trigger so that the drive pulse (width: w; amplitude: V) is applied when the D–B distance $(d + l\phi)$ is the smallest, i.e., the time when $\phi = -\phi_0$. In other words, the pulse is applied at $t = 0$ where the twisted angle is $\phi = -\phi_0\cos(\omega_0 t)$, therefore

$$d\phi = \phi\omega_0 \sin(\omega_0 t)dt, \tag{2.24}$$

and

$$E_{\rm pulse} = \int_0^w \frac{lV_{\rm B}VC_{\rm D}}{\varepsilon_0 S}\phi_0\omega_0\sin(\omega_0 t)dt = [\cos(\omega_0 w) - 1]\frac{lV_{\rm B}VC_{\rm D}\phi_0}{\varepsilon_0 S} \tag{2.25}$$

$$\simeq \frac{(\omega_0 w)^2}{2!}\frac{lV_{\rm B}VC_{\rm D}\phi_0}{\varepsilon_0 S}. \tag{2.26}$$

We compare $E_{\rm pulse}$ with $E_{\rm sinus}$ to be equal, so that we can convert the pulse drive voltage V with a width w to a sinusoidal voltage amplitude $V_{\rm D0}$ as

$$V_{\rm D0} = \frac{(\omega_0 w)^2}{2\pi}V. \tag{2.27}$$

This relation is useful to calculate Q for loop circuit.

2.1.9 Quality factor

Continuous sinusoidal drive

The definition of the quality factor is

$$Q \equiv 2\pi\frac{\text{(Energy stored)}}{\text{(Energy loss per cycle)}}. \tag{2.28}$$

The torsional equation of motion under an applying torque $N = N_0 \cos(\omega t)$ is

$$I\ddot{\phi} + \Gamma\dot{\phi} + k\phi = N_0 \cos(\omega t). \tag{2.29}$$

The solution is $\phi = \phi_0 \cos(\omega t + \theta)$, where ϕ_0 is an angular amplitude, and θ is a phase delay. The energy stored is a sum of a kinetic and a potential energy, so that

$$\begin{aligned}
(\text{Energy stored}) &= \frac{1}{2}I\dot{\phi}^2 + \frac{1}{2}k\phi^2 && (2.30)\\
&= \frac{1}{2}\phi_0^2[I\omega^2 \sin^2(\omega t + \theta) + k\cos^2(\omega t + \theta)] && (2.31)\\
&\xrightarrow{\omega=\omega_0} \frac{1}{2}\phi_0^2 I\omega_0^2. && (2.32)
\end{aligned}$$

The energy loss in one period, $P = 1/f = 2\pi/\omega$, is

$$\begin{aligned}
(\text{Energy loss per cycle}) &= \int_{\text{cycle}} \Gamma\dot{\phi}d\phi && (2.33)\\
&= \int_0^P \Gamma\phi_0^2\omega^2 \sin^2(\omega t + \theta)dt && (2.34)\\
&= \pi\Gamma\phi_0^2\omega && (2.35)\\
&\xrightarrow{\omega=\omega_0} \pi\Gamma\phi_0^2\omega_0 && (2.36)
\end{aligned}$$

Thus, at the resonance, the quality factor is

$$Q = \frac{\omega_0}{\gamma}. \tag{2.37}$$

The denominator γ is a full width at the half maximum of the Lorentzian function in Eq. (2.12).

As ω_0 is almost constant and the measuring amplitude R is equal to $|I_P|$ in Eq. (2.19), we have

$$Q = cR, \tag{2.38}$$

where c is a constant. Therefore, once we know c, we can get the temperature dependence of Q by simply measuring that of R with the loop circuit.

Ring-down method

We can also measure Q by a ring-down method. At a constant drive at the resonance (either sinusoidal or pulsed), we shut off the drive voltage at $t = 0$, then the current amplitude decays as

$$R = R_0 e^{-t/\tau_R}, \tag{2.39}$$

where τ_R is a relaxation time of R. The energy is $E \propto R^2$, therefore

$$E = E_0 e^{-2t/\tau_R}. \tag{2.40}$$

As the period $P = 1/f_0$ is far shorter than τ_R (because of high Q),

$$\text{(Energy Stored)} \simeq E_0, \tag{2.41}$$

and

$$\text{(Energy loss per cycle)} = E_0(1 - e^{-2P/\tau_R}) \simeq 2E_0 P/\tau_R, \tag{2.42}$$

for one period, $t = 0 \longrightarrow P$. Thus we get from the definition

$$Q = \pi f_0 \tau_R. \tag{2.43}$$

2.1.10 Linearity and rim velocity

If a very large torque is applied to the torsional oscillator, the torsional oscillator oscillates nonlinearly, and above relations do not hold. I confirmed in the experiments that the torsional oscillator oscillated in a linear regime with the applied drive voltage, i.e., $R \propto V_{\rm D}$.

The twisted angle $|\phi_0|$, rim velocity $v_{\rm r}$, and the maximum strain ϵ are given by

$$|\phi_0| = \frac{N_0}{|i\omega_0 \Gamma|}, \tag{2.44}$$

$$v_{\rm r} = r\omega|\phi_0|, \tag{2.45}$$

$$\epsilon = \frac{r|\phi_0|}{L}. \tag{2.46}$$

Some experimental parameters are listed in Table 2.4.

The value of the moment of inertia I of the brass bob is determined by the size and the density of the material. We rely on a calculated value from the design, $I = 3.5 \times 10^{-6}$ kgm^2. We get the damping coefficient and the torsion constant from the observed values of ω_0 and Q at 4 K, so that

$$\Gamma = I\omega_0/Q = 4.1 \times 10^{-7} \text{ kgm}^2\text{s}^{-1}, \tag{2.47}$$

and

$$k = \omega_0^2 I = 1.0 \times 10^2 \text{ kgm}^2\text{s}^{-2}.$$

The pulsed voltage ($V = 1.50$ V, $w = 50$ μs) applied in the experiments can be converted into $V_{\rm D0} = 0.017$ V of ac sinusoidal voltage from Eq. (2.27). The applied torque is, from Eq. (2.14)

$$N_0 = \frac{l V_{\rm B} V_{\rm D0} C_{\rm D}^2}{\varepsilon_0 S} = 2.3 \times 10^{-9} \text{ Nm}. \tag{2.48}$$

Table 2.4: Parameters in the torsional oscillator experiment.

Property	Value
Drive voltage	$V = 1.50$ V, $w = 50$ μs
Bias voltage	$V_B = 200$ V
D–B capacitance (at 4 K)	$C_D = 6.6686$ pF
P–B capacitance (at 4 K)	$C_P = 10.1055$ pF
Electrode arm length	$l = 12.5$ mm
Area of fixed electrode	$S = (5.5)^2\pi$ mm^2
Resonant frequency (< 4 K)	$f = 860$ Hz
Quality factor (< 4 K)	$Q = 4.6 \times 10^4$

Then we have $|\phi_0| = 1.0 \times 10^{-6}$ at the tip of the Gelsil rod, $v_r = 15$ μm/s at the rim of the tip ($r = 2.7$ mm), and $\epsilon = 1.6 \times 10^{-7}$ at the rim ($r = 2.7$ mm). The oscillation amplitude at the rim of the tip is $r|\phi_0| = 2.7$ nm, which is equivalent to the pore diameter of the Gelsil.

2.2 Refrigerator and thermometry

2.2.1 Dilution refrigerator

The ^{3}He–^{4}He dilution refrigerator is an essential apparatus to produce low temperature between 0.01–1 K in modern cryogenics [18]. We used a commercial dilution refrigerator with a Joule–Thomson helium condenser [102]. A schematic plan and a photograph inside the inner vacuum can (IVC) are shown in Fig. 2.7.

A typical condensation process of ^{3}He–^{4}He mixture is as follows: The refrigerator insert is submerged in liquid ^{4}He at 4.2 K in the dewar (outer vacuum can). The ^{3}He–^{4}He mixture gas (1:3 in ratio) at room-temperature was pressurized by a roots pump and a metal bellows compressor at 2.8–3.4 bar into the Joule–Thomson helium condenser. The pressure was stabilized in the range by opening and closing an electric valve automatically by the gas-handling system of the dilution refrigerator. The Joule–Thomson helium condenser cools down until 1 K by Joule–Thomson effect, and the mixture gas condenses into liquid. The mixture liquid cools the entire setups inside the inner vacuum can (shown in Fig. 2.7). When the necessary amount of ^{3}He–^{4}He mixture gas was condensed, the electric valve is closed and the temperature at the mixing chamber cools down to subkelvins. Then we start a turbo molecular pump for the normal circulation operation. The lowest temperature was 13 mK with loading the cooper plate and the torsional oscillator (in the ^{3}He experiment).

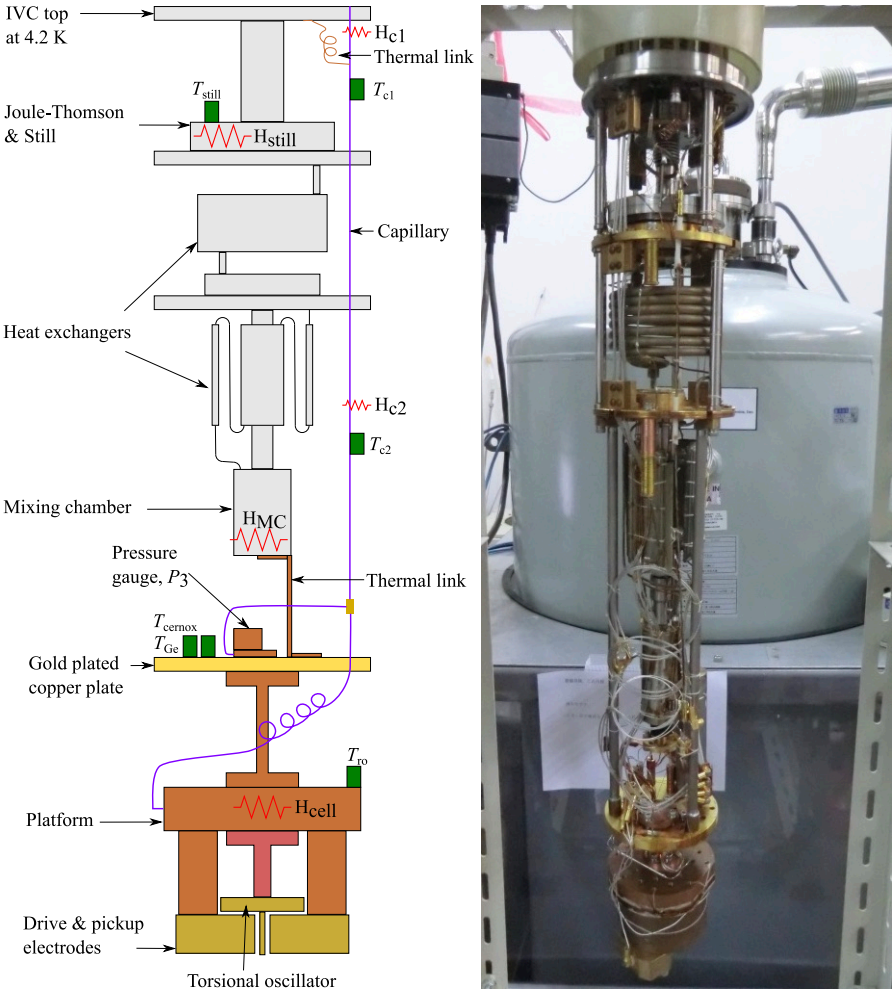

Figure 2.7: (Left) Schematic plan and (Right) photograph of the basic experimental setup inside the inner vacuum can (IVC) of the dilution refrigerator. The grey part is the dilution refrigerator, and the colored part is the torsional oscillator (brown and yellow), the pressure gauge (brown), the thermometers (green), the heaters (red), and the capillary (purple). The background of the photograph is the dewar.

The initial transfer consumes 60 litters of liquid ^{4}He. The additional transfer of 30 litters was done once a week. A helium re-condenser [106] was running during the experiments.

2.2.2 Temperature control

The temperatures at 4–6 points were monitored during the experiments, whose positions are indicated in Fig. 2.7 [Left]. We employed a ruthenium oxide (RuO_2) resistance thermometer ($T_{\rm ro}$) on the torsional oscillator platform, a germanium (Ge) thermometer ($T_{\rm Ge}$) and a Cernox thermometer ($T_{\rm cernox}$) on a copper plate, a still thermometer ($T_{\rm still}$) on the still, and two carbon ceramic sensors ($T_{\rm c1}$ and $T_{\rm c2}$) on the capillary. The thermometers on the capillary were introduced in the neon and the hydrogen experiments. The thermometer temperatures $T_{\rm Ge}$, $T_{\rm cernox}$, $T_{\rm still}$, $T_{\rm c1}$ and $T_{\rm c2}$ were calibrated by manufacturers.

The RuO_2 thermometer used to measure the temperature at the torsional oscillator was calibrated by us with the calibrated $T_{\rm Ge}$ (0.043–5 K) and a SRM768 temperature reference standard (below 0.5 K) on the copper plate. The fitting function is a modified version of a equation in Ref. [10],

$$(T_{\rm ro}/{\rm K})^{-0.20} = A_0 + A_1 \log(R_{\rm ro}/\Omega), \tag{2.49}$$

where $R_{\rm ro}$ is the measured resistance of the RuO_2 thermometer. This calibration was used to extend the lowest temperature limit until 0.013 K. At high T, this calibration was good until 1.3 K. The resistance of RuO_2 changes by thermal cycle, therefore we did this calibration for each experiment after the initial transfer. We measured no temperature difference between $T_{\rm ro}$ and $T_{\rm Ge}$, even when we used a heater at the torsional oscillator cell, $H_{\rm cell}$. Therefore, we regard $T_{\rm ro} = T_{\rm Ge}$ in the entire experiments below 1.3 K. A temperature between 1.0–300 K was measured with the Cernox thermometer.

We used three temperature control methods:

1. PID control with $T_{\rm ro}$ and a heater $H_{\rm cell}$ (0.01–1.3 K).
2. PID control with $T_{\rm cernox}$ and a heater $H_{\rm MC}$ (1.0–22 K).
3. Heat pulse to a heater $H_{\rm MC}$ (1.0–22 K).

In the ^{4}He and ^{3}He experiments, I used the first temperature control method. In the Ne experiment, the second method was used. In the H_2, HD, and D_2 experiments, a combination of the first and third method was used.

The first method was achieved by using a high-precision resistance bridge for use of cryogenic experiments and the thermometer and heater at the torsional oscillator

platform. The ^{3}He–^{4}He mixture was circulating through the dilution refrigerator (normal operation). As we can see in the data in this thesis, the stability of the temperature was sufficiently good. The higher temperature was limited to 1.3–2 K because the pressure in the circulation line, especially the pumping pressure, becomes so high that the turbo molecular pump may be damaged.

In the second temperature control method, we extended the temperature until 22 K. We circulated a small amount of ^{3}He–^{4}He mixture, about 15% of the normal operation. By this method, we could maintain the cooling power by Joule–Thomson effect, and the pumping pressure was kept moderate. The temperature was controlled with PID mode of a conventional cryogenic temperature controller.

The third temperature control method is an improved one from the second method. In some situations the temperature was not stabilized, probably because of a long relaxation time in the second method. A constant power heat pulse was applied to a heater H_{MC} at the mixing chamber without circulating the mixture. We waited for a few minutes for thermal equilibrium, then measured the temperature and the resonant frequency and amplitude of the torsional oscillator. The power and duration of the heat pulse were changed at different temperatures (high power and long duration at high temperatures) to keep ΔT per pulse roughly constant.

2.3 Gas handling system for film adsorption

We used a gas-handling system to prepare an adsorbed film on the cryogenic substrate. The schematic diagram and a photograph of the gas-handling system are shown in Fig. 2.8. The valves except V0 are needle valves, and V0 is a bellows valve. Two pressure gauges are digital gauges measuring P_1 and P_2, and the other is a Bourdon tube pressure gauge in a range 0–2 bar.

The tubes at V1–V5, at the right side of the gas-handling system, were connected to a liquid helium dipstick and sample gas cylinders. The liquid helium dipstick is a high pressure-resistant cylindrical tube with a valve and a Bourdon tube pressure gauge at the top, and with packed charcoal and molecular sieve at the bottom [107]. By immersing the bottom part in liquid helium at 4.2 K, either ^{4}He or ^{3}He gas are adsorbed on the packed porous material. We used the dipstick to collect the expensive ^{3}He gas in the cell after the ^{3}He experiment.

We used sample gases in cylinders purchased by suppliers. The impurity concentrations of the gases are reported by manufacturers or a supplier described in Table 2.5. The impurities in ^{3}He, HD and D_2 are probably the most abundant isotopes, ^{4}He or H_2. The neon gas was not separated into the isotopes. The natural abundance of isotopes ^{20}Ne, ^{22}Ne (bosons), and ^{21}Ne (fermion) are 90.48%, 9.25%, and 0.27%, respectively [108]. Our gas sample should therefore have the ratio close

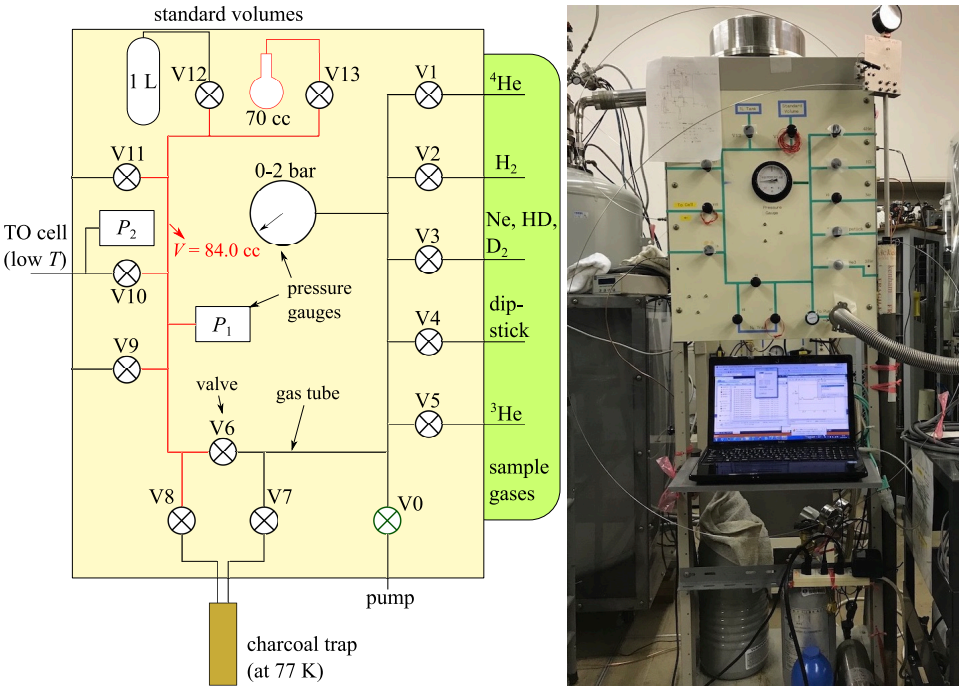

Figure 2.8: (Left) Schematic diagram and (Right) photograph of the gas-handling system for film adsorption. For example, ^{4}He gas was collected to the 1 L standard volume through valves V1, V7, V8, and V12 with others closed. Then V8 was closed (V12 is opened), and V10 was opened and closed when a desired moles were added to the torsional oscillator (TO) cell.

to the natural one, although the ratio was not analyzed.

The sample gas was moved from the right to left side in the gas-handling system through V7, the charcoal trap and V8 to eliminate the impurities such as water, and was prepared in one of the two standard volumes (1 liters or 70 cc ones) with V12 or V13 opened. When a desired amount of gas was moved, we closed V8. Then we have a gas of a volume V at a pressure P_1 and a temperature T in the red area in Fig. 2.8 (an example when only V13 is opened). When V13 is opened while others are closed, $V = 84.0$ cc. When only V12 is opened, $V = 1.02$ liters. We added the gas by opening and closing V10, and measured P_1 and T before and after the addition of the gas. The moles added N to the cryogenic torsional oscillator cell were calculated by the ideal gas law for the remaining gas, i.e., $N = (P_1V/RT)_{\rm before} - (P_1V/RT)_{\rm after}$, where R is the ideal gas constant. Typically, we added the molecules as $\Delta P = 4.9$ kPa at $T = 300$ K with the volume

Table 2.5: Information of sample gases.

Gas	Impurity concentration	Supplier	Manufacturer
^{4}He	$< 5 \times 10^{-7}$	[109]	[110]
^{3}He	$< 5 \times 10^{-4}$	[111]	
Ne	$< 1 \times 10^{-5}$	[109]	[110]
H_2	$< 1 \times 10^{-7}$	[109]	[110]
HD	$< 3 \times 10^{-2}$	[109]	[112]
D_2	$< 4 \times 10^{-2}$	[109]	[110]

$V = 84.0$ cc; we added $N = \Delta PV/RT = 1.7 \times 10^{-4}$ mol; the coverage changes by $\Delta n = N/S = 1.0\ \mu\text{mol/m}^2$.

During the introduction of neon and hydrogen to the torsional oscillator, we monitored pressures P_1 and P_2 in the gas-handling system (shown in Fig. 2.8), and P_3 in the dilution refrigerator (in Fig. 2.7) because these molecules can solidify in the cryogenic capillaries. If a solid grows in the capillary, the adsorbed film is not properly prepared at the desired coverage. A capillary block because of solid formation was detected as a pressure difference between P_2 and P_3. To measure P_3, we used a hand-made capacitive pressure gauge. We first made one with a gold-plated Kapton (plastic film) diaphragm (0.026 mm thick, ϕ14.0 mm in diameter) of design after Ref. [79]. This capacitive pressure gauge was used in the Ne, HD, and H_2 experiments. It has high sensitivity, but has a non-monotonic temperature dependence in a range 1–22 K and a hysteretic behavior when we applied a high pressure ($P_3 \sim 10$ kPa). Then we made another with a thin beryllium copper diaphragm (0.15 mm thick, ϕ12.0 mm in diameter) [113], which was used in the D_2 experiment. This has a monotonic temperature dependence and a reproducibility for high pressures. Either capacitive pressure gauges were sufficient to read if the pressure difference is present or not.

2.4 Experimental procedure

Here we describe the entire flow of experiments, which took about two years. We first performed the measurement for ^{4}He films. Then the torsional oscillator was warmed up to room temperature with pumping out the adsorbed ^{4}He with a turbo molecular pump, and the measurement for the next adsorbate, ^{3}He, was made. In the same manner, we made measurements in the order of ^{4}He, ^{3}He, Ne, HD, H_2, and D_2 with thermal cycles.

2.4.1 Helium film experiments

Before the cooling of the dilution refrigerator from room-temperature, the cell was flushed with the pure ^{4}He gas which was introduced through a charcoal trap immersed in liquid nitrogen. After the first transfer of liquid helium to the dewar of the dilution refrigerator, we started the experiment.

In the helium experiments, the quality factor was measured by a ring-down method in Eq. (2.43) before the warming and after the cooling at the lowest temperature for each coverage. We confirmed that $c = Q/R$ in Eq. (2.38) does not change during the helium experiment. For the ^{4}He experiment, $c = 2.48 \times 10^4$ nA^{-1}, and for the ^{3}He experiment, $c = 2.06 \times 10^4$ nA^{-1}. The dissipation Q^{-1} at each temperature is obtained from the corresponding current R.

Background data of the empty cell

Before the adsorption of helium, we took the temperature dependence of the resonant frequency f and energy dissipation Q^{-1} of the torsional oscillator. The result is shown in Fig. 2.9. The resonant frequencies without helium ($n = 0$, empty cell) at 1.0 K were $f = 860.822$ Hz for the ^{4}He and $f = 860.145$ Hz for the ^{3}He experiment, respectively. The slight difference between the two is because of a thermal cycle, which is typical of the torsional oscillator experiment: This is probably because of difference in the manner of thermal shrinkage with different cooling speed from 300 to 4 K or aging of the torsional oscillator material.

We refer to the temperature dependence of f and Q^{-1} of the empty cell ($n = 0$) as the background. The background resonant frequency was found to be linear in $\log(T/\mathrm{K})$ at $T > 20$ mK. We fit the data to a linear function

$$f_{\mathrm{B}}(T) = A_0 + A_1 \log(T/\mathrm{K}), \tag{2.50}$$

where the subscript B denotes the background. The fitting results are shown in Fig. 2.9 with solid lines. For the ^{3}He run, f takes a maximum at about 30 mK and decrease with further lowering T. We assume that f is constant below 30 mK because the number of data are not sufficient to fit the T dependence.

The dissipation Q^{-1} of the empty cell slightly increases as T decreases from 1 K to 80 mK, followed by a sudden drop below 50 mK. We fit $\log Q_{\mathrm{B}}$ to a polynomial

$$\log[Q_{\mathrm{B}}(T)] = \sum_{i=0}^{9} B_i \left[\log(T/\mathrm{K})\right]^i . \tag{2.51}$$

The drop of f and Q^{-1} below 30–50 mK is consistent with the effect of tunneling two-level systems (TLS) [10] which exist in the porous Gelsil glass. But this kind

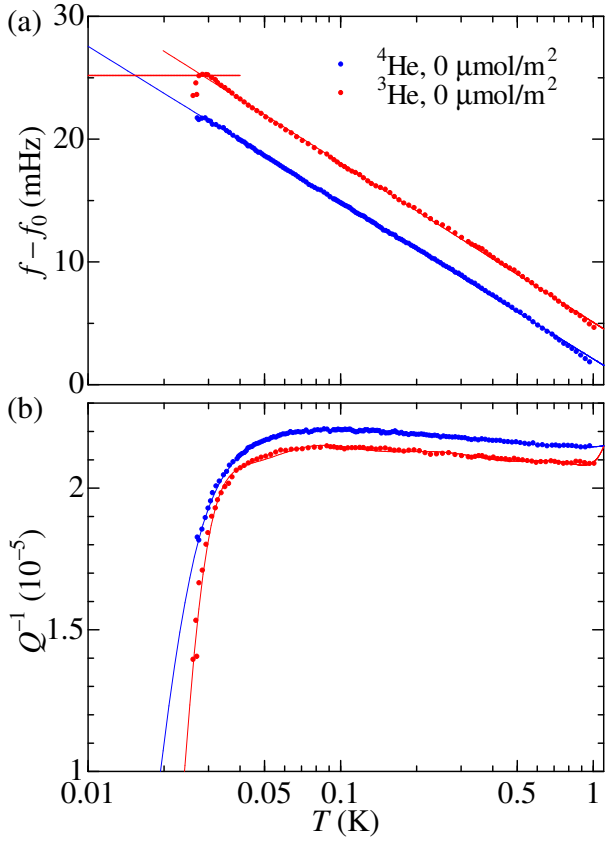

Figure 2.9: Background data of the empty cell (n = 0 μmol/m^2) of the ^{4}He and ^{3}He experiments. (a) Resonant frequency f from which a constant f_0 is subtracted. Here f_0 = 860.82 Hz for the ^{4}He run, and f_0 = 860.14 Hz for the ^{3}He experiment, respectively. (b) Energy dissipation Q^{-1} for the ^{4}He and ^{3}He runs. Lines and curves are results of the fitting (see the text).

of temperature dependence of the background is also characteristic of torsional oscillators with beryllium copper torsion rods [59].

Preparation of helium films and measurement

To prepare an adsorbed helium film, a known amount of helium gas was admitted from a room temperature gas-handling system with 1 L standard volume to the torsional oscillator at $T < 150$ mK. The capillary was thermally anchored at each stage of the dilution refrigerator to reduce the heat flux to the torsional oscillator, which is not shown in Fig. 2.7. After adsorbing helium gas at low temperature, the torsional oscillator was warmed up at sufficiently high temperature, typically 1–5 K, for several hours to uniformly spread out in the Gelsil. The torsional oscillator was again cooled to 10–30 mK. We measured the factor $c = Q/R$ at the lowest temperature for each coverage. We stated a measurement of the temperature dependence of the resonant frequency f and the dissipation Q^{-1} up to 1.1 K with the first temperature control method in Sect. 2.2.2. Data shown in this paper were taken during the warming. After the warming, the heater was turned off and the torsional oscillator was cooled, and adsorption for the next coverage was started. No hysteresis was observed between the warming and cooling.

The annealing temperature and duration were selected so that the frequency and the amplitude become stable. For ^{4}He films of coverage $n < 15$ μmol/m^2, the annealing was done at 5 K for 5 hours. At $16 \leq n \leq 26$ μmol/m^2, it was done at 1.1 K for more than 14 hours. For ^{3}He films, we annealed at 5 K for 5 hours for all coverages. For 16 μmol/m^2 of ^{3}He, we first annealed at 1.1 K for 12 hours as in the case of ^{4}He film. However, this condition was not sufficient because the frequency and dissipation were almost the same as those of previous $n = 15$ μmol/m^2 data. This indicates that ^{3}He atoms in the extended state (see Chapter 3) are less mobile than ^{4}He atoms. We finally found that the annealing at 5 K for 5 hours was sufficient for ^{3}He.

2.4.2 Neon film experiment

Before the Ne experiment, the gas-filling capillary was replaced from that used in the ^{4}He and ^{3}He experiments. Neon solidifies at such temperatures, therefore the capillary was *not* thermally anchored in the refrigerator except near the mixing chamber and the torsional oscillator cell, as shown in Fig. 2.7. The temperature of the capillary was measured at two points, and we confirmed that the two temperature was always higher than the temperature at the torsional oscillator cell. As neon film wets the surface of glass, neon atoms prefer to be inside the Gelsil, not in the the open space in the torsional oscillator cell (copper surface), at the same temperature.

Background data of the empty cell

The Ne experiment was done in a temperature range 1–22 K. The background data ($n = 0$, empty cell) is shown in Fig. 2.10. We fit f and Q with

$$f_{\mathrm{B}}(T) = A_0 \log(T/\mathrm{K}) + \sum_{i=1}^{8} A_i (T/\mathrm{K})^{i-1}, \tag{2.52}$$

and

$$\log[Q_{\mathrm{B}}(T)] = B_0 \log[\log(T/\mathrm{K})] + \sum_{i=1}^{10} B_i [\log(T/\mathrm{K})]^{i-1}. \tag{2.53}$$

There happened an abrupt decrease in the resonant frequency as large as −205 mHz during the annealing of the $n = 15$ μmol/m^2 film. I guess that no mechanical shock was applied to the refrigerator at that moment. The abrupt change of resonant frequency during the transfer of liquid helium is not rare, but it is typically of the order of 1 mHz. Though the cause of such large change is unknown, we offset the value to the resonant frequency data with coverage larger than 14 μmol/m^2.

Preparation of neon films and measurement

We took two days to measure the temperature dependence of f and Q^{-1} for one coverage. In the morning of the first day, the temperature $T = T_{\mathrm{cernox}}$ is about 10–20 K, which is lower than the triple point temperature $T_{\mathrm{t}} = 24.6$ K of neon. We added a known amount of neon gas to the torsional oscillator cell through the hot capillary, then we raised the temperature above T_{t}, typically at 25 K, with a heater $\mathrm{H_{MC}}$. The heater was turned off, and the torsional oscillator was cooled down through the night very slowly by a weak thermal link between the torsional oscillator cell to the top flange of the refrigerator at 4.2 K.

In the morning of the second day, the temperature is between 20–25 K, and the pressure is more or less 1 kPa. This value of the pressure ensures that an unsaturated film formed and was annealed in the Gelsil, and no solid exists on the capillary wall because it is lower than the sublimation pressure. We cooled the torsional oscillator by Joule–Thomson effect of circulating ^{3}He–^{4}He mixture gas of 15 % of the usual amount for the standard dilution refrigeration. In the evening, the temperature was 1 K, then we took the ringdown three times to measure c.. The value was $c = (1.92 \pm 0.05) \times 10^4$ nA^{-1} with a standard deviation, and we used the mean value 1.92×10^4 nA^{-1} for every coverage to get Q. We began the measurement of f and Q^{-1} with the second temperature control method in Sec 2.2.2.

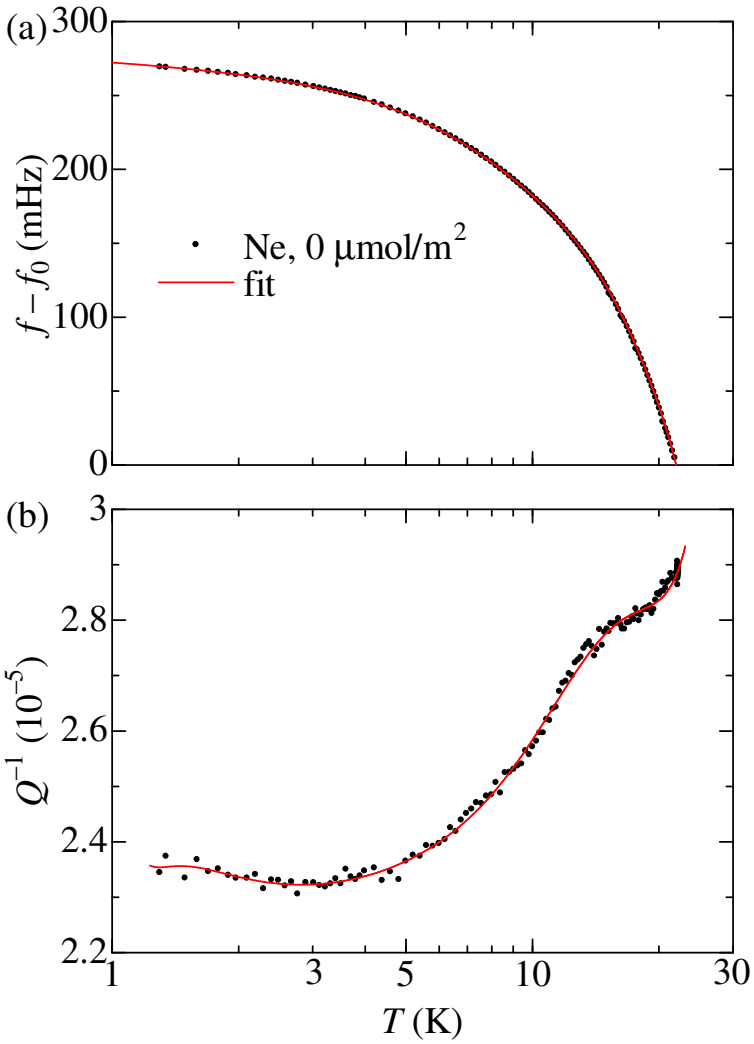

Figure 2.10: Background data of the Ne experiment. (a) Resonant frequency f from which a constant f_0 = 859.138 Hz is subtracted. (b) Dissipation Q^{-1}. The red solid curves are results of the fittings.

A neon film with the desired coverage was prepared by adding a known amount of neon gas to the cryogenic substrate. The neon gas was prepared in a room-temperature volume 84.0 cm^3, which consists of a standard volume and capillaries, and added into the cryogenic part by opening a needle valve between them. The temperature of the torsional oscillator was kept above the bulk triple point temperature 24.6 K for a few hours after the gas addition, then it was slowly decreased with weak cooling power by Joule–Thomson effect of circulating ^{3}He–^{4}He mixture. In this procedure, the adsorbed film is annealed and becomes uniform, and no bulk solid grows outside the Gelsil. The capillary inside the dilution refrigerator was wound by a heater of Manganin twisted wire, and was not thermally anchored except near the mixing chamber. The temperature of the capillary at a level of the still was measured and was confirmed to be always hotter than the torsional oscillator without using the heater.

We established the abovementioned procedure as a result of unsuccessful uniform adsorptions of neon on the Gelsil substrate. The first two coverages, which were intended to yield $n = 5$ and 8 $\mu mol/m^2$, were not properly prepared. Bulk solid neon was formed outside the Gelsil and blocked the capillary, which we concluded from a rise of P_2 (see Fig. 2.8) when the solid melted. We estimate the amount of solid from the volume and temperature in the capillary and P_2. We assume that the uncertainty of the estimated amount of solid is 30%, and we have the estimated coverages of (4.0 ± 0.3) and (4.5 ± 1.0) $\mu mol/m^2$, respectively.

2.4.3 Hydrogen film experiments

We have expected that hydrogen films may exhibit quantum phase transitions. Therefore, we have measured the elasticity at as low temperature as possible. We found that the lowest temperature was 80–100 mK with normal operation of the dilution refrigerator without thermal anchor of the capillary. We set the highest temperature at 22 K, which is above the triple point temperatures of bulk hydrogen isotopes.

We have learned from the Ne experiment that the thermal anchor near the mixing chamber is undesirable. The anchored point of the filling capillary may be cooler than the torsional oscillator cell when the torsional oscillator is warmed and the mixture was weakly circulating, and consequently the adsorbed molecules leaves from the porous glass to solidify on the coolest capillary wall. In the hydrogen experiments, we put only one thermal anchor between the 4.2 K bath and the top level of the capillary in the vacuum can. With this thermal anchor, the temperature at the capillary T_{c1} was 7 K when cooling torsional oscillator down to 100 mK. Without it, however, the temperature T_{c1} becomes higher than 30 K, and the lowest temperature of the torsional oscillator becomes above 100 mK because of heat flow.

Background data of the empty cell

The mathematical functions used to fit to the background data of the H_2, HD, and D_2 experiments, shown in Fig. 2.11, are the same as those of the Ne experiment.

The temperature dependence of the resonant frequency f has small discrepancy among the three experiments. The absolute values of the energy dissipation Q^{-1} are different, almost by a factor of 2. This is probably because of the difference in mechanical isolation conditions of the torsional oscillator cell. We made the experiments in the order of HD, H_2, and D_2, and we improved the mechanical isolation by changing the fixing point of the capillary near the torsional oscillator. In the HD experiment, the dissipation was highest in the entire temperature range probably because of vibration noise transmitted by the capillary to the torsional oscillator. A hump in Q^{-1}, shown in Fig. 2.11 (b), was observed only in the HD experiment. The frequency often shifted after film adsorptions. The condition of the capillary was improved in the next H_2 experiment.

The sawtooth-like rise of Q^{-1} in the D_2 empty cell, shown in Fig. 2.11 (b), was occasionally seen in many D_2 coverages at different temperatures in a range 10–20 K. We concluded that the sawtooth rise is an accidental background signature that is not related to the elastic anomaly, and ignored it.

The constant that relates the current amplitude of torsional oscillation to the quality factor, i.e., $c = Q/R$, was $c = (1.84 \pm 0.04) \times 10^4$, $(1.93 \pm 0.08) \times 10^4$, and $(1.85 \pm 0.02) \times 10^4$ nA^{-1}, for the H_2, HD, and D_2 experiment, respectively.

Preparation of hydrogen films and measurement

Each measurement for a single hydrogen coverage was a two-day long sequence. In the afternoon of the first day, the previous measurement up to 22 K was finished. The temperature of the torsional oscillator cell was decreasing very slowly because the heater was off but the thermal connection between the torsional oscillator and the liquid ^{4}He bath at 4.2 K is weak. Two capillary thermometers, T_{c1} and T_{c2}, were PID controlled at 25 K. We prepared a known amount of hydrogen gas at the gas-handling system, and added it to the cell by carefully opening the needle valve. After the addition, we closed the valve and calculated the coverage from the temperature and the pressure before and after the addition. We raised the torsional oscillator cell temperature to about 23 K, which is well above the bulk triple point temperature, and confirmed that the pressure increased. We left the refrigerator overnight without circulating the mixture *or* with circulating the mixture and PID controlling the temperature at the torsional oscillator cell to gradually decrease.

In the morning of the second day, the temperature was typically 5–10 K. We began the ^{4}He–^{3}He mixture condensation of the dilution refrigerator. After

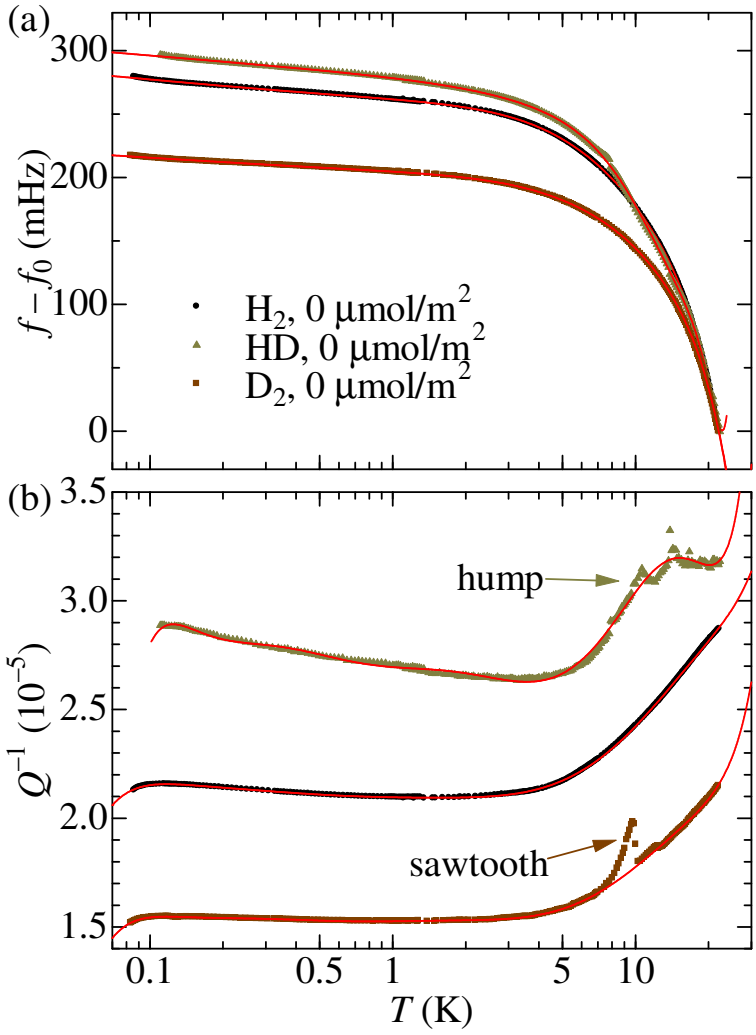

Figure 2.11: Background data of the H_2, HD, and D_2 experiments. (a) Resonant frequency f from which a constant f_0 is subtracted. The constant is set $f_0 = f(22\,\mathrm{K})$, which are 858.383, 859.371, and 849.163 Hz, for the H_2, HD, and D_2 experiment, respectively. (b) Dissipation Q^{-1}. Curves are results of the fitting.

the condensation, the turbo molecular pump was turned on, and we waited until the temperature becomes the lowest, typically 0.08–0.10 K. We measured $c = Q/R$ three times by the ring-down method. The T-dependence of f and Q^{-1} was measured by the first temperature control method in Sec 2.2.2. After the measurement in a temperature range 0.08–1.3 K, the temperature was kept at 1.3 K. We measured c again three times. The difference in c at 0.08-0.1 K and 1.3 K was within a few percent. Then we start collecting the mixture with PID controlling the temperature $T_{\rm cernox}$ at 3.0 K. Usually, it was already nighttime of the second day. We started a computer program for measurement, which turn off the PID controlled heater $\rm H_{MC}$ in 7 hours, waited for 2 hours, and start the third temperature control method in Sec 2.2.2 with measuring f and Q^{-1}.

Chapter 3

Helium Films

In both bosonic ^{4}He and fermionic ^{3}He films, we discovered the elastic anomaly, in which the elasticity of the film increases at low temperatures with an excess dissipation [8]. The elastic anomaly vanishes at a critical coverage, $n_c \sim 20$ μmol/m^2, corresponding to about 1.8 atomic layers. The thermal activation model [7, 81] combined with the elastic relaxation process successfully describes the experimental data, and we get an energy gap, which vanishes at $n \to n_c$, from fittings. We also get two-dimensional compressibility which diverges at $n \to n_c$ from a model of n-dependent energy band structure and a direct calculation from the experimental data. The elastic anomaly of helium films is linked to the quantum phase transition.

3.1 Experimental results

3.1.1 Raw data

Figure 3.1 shows the raw data of the resonant frequency f and energy dissipation Q^{-1} of the torsional oscillator at $n = 0$ (empty cell, background) and $n = 15.0$ μmol/m^2. The resonant frequency f at $n = 15.0$ μmol/m^2 increases from the background data in the entire temperature range. Furthermore, f at $n = 15.0$ μmol/m^2 increases more rapidly below 0.6 K than the background does. The energy dissipation Q^{-1} at $n = 15.0$ μmol/m^2 has a remarkable peak at about 0.5 K, where the slope of f is the largest. As T decreases further, f tends to saturate and Q^{-1} decreases. The gradual increase in f suggests a crossover in helium film from a soft to a stiff state, not a first order phase transition such as solidification. We call this anomalous elastic behavior an *elastic anomaly*.

Here we confirm that the above elastic anomaly does not originate from the mass decoupling. We have observed that f increases by $\delta f \sim 50$ mHz by the helium

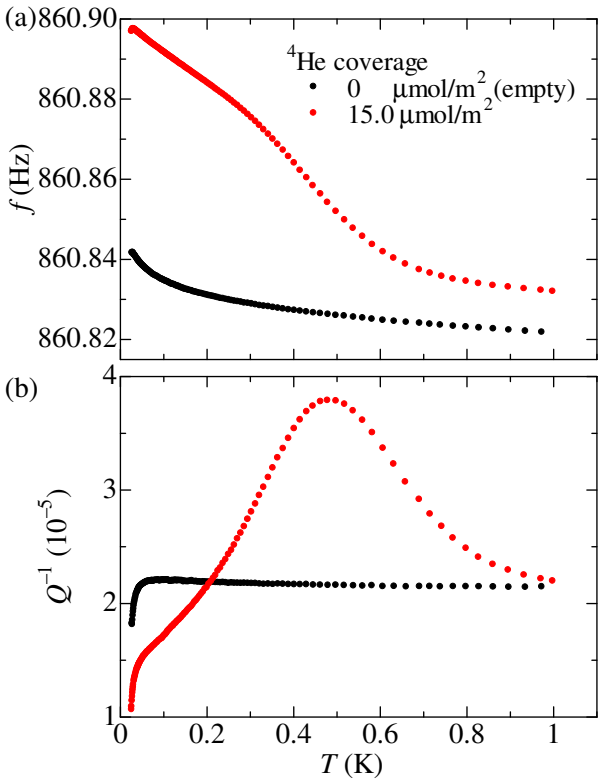

Figure 3.1: (a) Resonant frequency f and (b) dissipation Q^{-1} of the torsional oscillator with and without ^{4}He film.

adsorption of $n = 15.0\ \mu\mathrm{mol/m^2}$. From the FEM simulation result in Chapter 2, we can calculate that the frequency changes by $\delta f = -1.5$ mHz when 15 μmol/m^2 of ^{4}He film is adsorbed. Even if all the helium atoms were mass-decoupled from the oscillation, the frequency would increase by only 1.5 mHz. Thus the explanation using mass decoupling by superfluidity, supersolidity [90, 92, 95], and slippage phenomena [66, 87, 88] is rejected for the observation of the elastic anomaly.

3.1.2 Coverage dependence of the elastic anomaly

In Fig. 3.2, we show raw data for the coverage n from 0 to 23 μmol/m^2 for ^{4}He, and to 20 μmol/m^2 for ^{3}He, respectively. For both ^{4}He and ^{3}He films, we observed qualitatively similar elastic anomalies which are strongly coverage-dependent. The elastic anomaly vanishes at $n \simeq 23$ and 20 μmol/m^2 for ^{4}He and ^{3}He, respectively. We can regard these coverages as the critical coverage n_c. We will discuss later that n_c determined from the elastic anomaly in ^{4}He is identical to n_c for the onset of superfluidity within the experimental accuracy. At coverages $n > n_c$, both $f(T)$ and $Q^{-1}(T)$ are almost identical to those of the background, except for a small upward shift in f at all temperatures (+6 and +3 mHz for ^{4}He and ^{3}He, respectively). Therefore, in the superfluid phase of ^{4}He and the liquid phase of ^{3}He, no prominent elasticity change is observed. It is remarkable that at $n > n_c$ the torsional oscillator behaves as if there were no adsorbed helium except the temperature-independent shift.

Comparing the resonant frequencies at $n = 15$ and 23 μmol/m^2 of ^{4}He, for instance, we see that $f(15\ \mu\mathrm{mol/m^2})$ is larger than $f(23\ \mu\mathrm{mol/m^2})$ in the entire temperature range. This means that the thinner film has a *larger* elastic constant than the thicker film does. Therefore, the inert layer model, where the inert solid layer monotonically becomes thicker by increasing the coverage, does not explain the elastic anomaly. We show below that a two-band model considering gapped excitation in the localized state explains qualitatively the observed elastic anomaly.

3.1.3 Data at higher coverages

The resonant frequency shift δf and energy dissipation Q^{-1} at higher coverages ($n > n_c$) are shown in Fig. 3.3. We set $\delta f = 0$ at $T_{\max} = 1.1$ K because f sometimes jumped at $n > n_c$ probably due to the shock by liquid helium transfer. We made no correction for Q^{-1}, and the jump in Q^{-1} of ^{3}He between $n = 25.0$ and 27.0 $\mu\mathrm{mol/m^2}$ is possibly because of some shock.

The resonant frequency shift and energy dissipation have almost no coverage dependence at $n > n_c$, compared to the data at $n < n_c$. The highest coverage for ^{4}He was 25.0 $\mu\mathrm{mol/m^2}$, which is in a coverage of superfluid and is below the full-

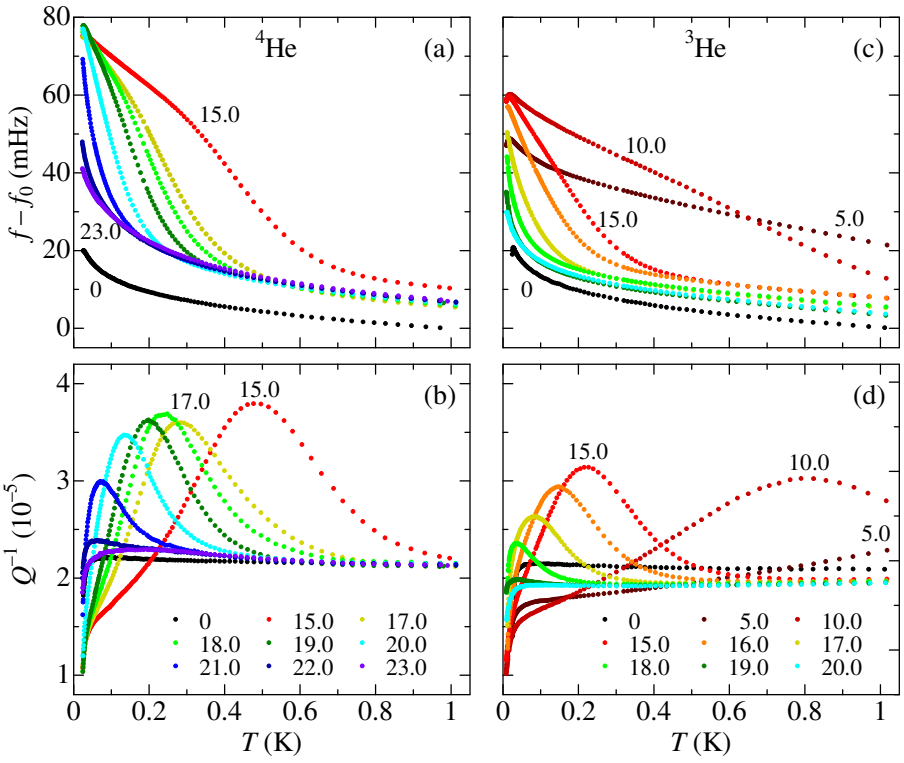

Figure 3.2: Resonant frequency f and energy dissipation Q^{-1}. (a) and (b): ^{4}He, and (c) and (d): ^{3}He films. Numbers give the coverage n in units of μmol/m^2. The constant f_0 is 860.822 Hz for ^{4}He and 860.145 Hz for ^{3}He, respectively.

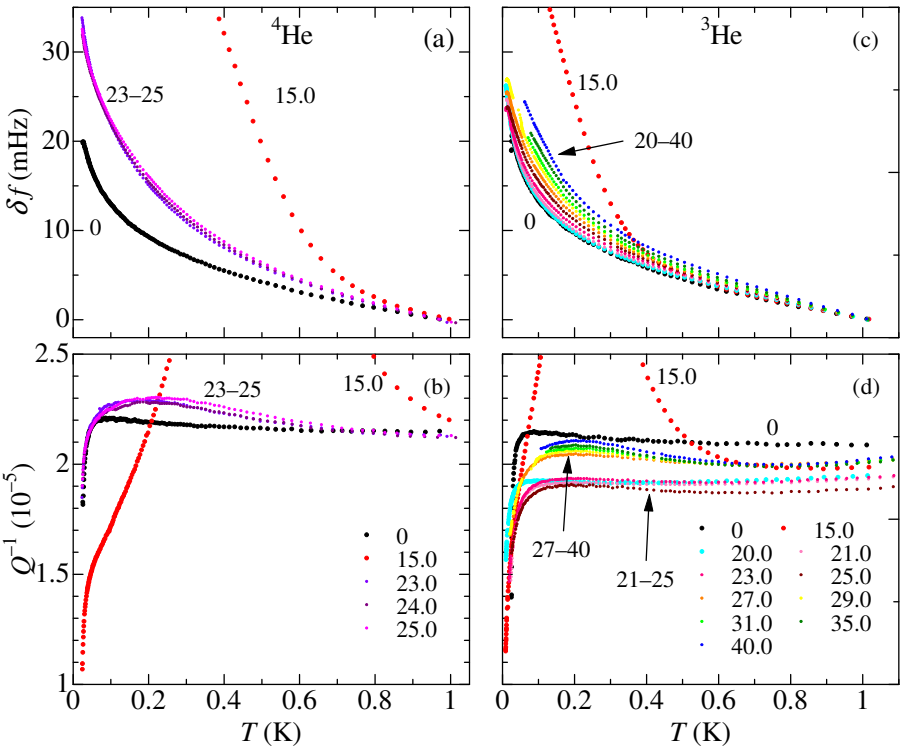

Figure 3.3: Resonant frequency shift $\delta f = f(T) -$ const. and energy dissipation Q^{-1} at higher coverages ($n > n_c$). (a) and (b): ^{4}He, and (c) and (d): ^{3}He films. Numbers give the coverage in units of μmol/m^2. The resonant frequency shift is set $\delta f(T_{max}) = 0$. Data of 0 and 15.0 μmol/m^2 are shown for comparison.

pore coverage, $n_{\rm fp} = 40.2$ μmol/m^2. The superfluid transition temperature $T_{\rm c}$ at $n = 25$ μmol/m^2 ($n - n_{\rm c} = 2$ μmol/m^2) is estimated to be roughly 200 mK from the previous results [49, 89] (see Fig. 1.16 for instance). We see no effect by superfluid transition in this measurement, as expected. The highest coverage for ^{3}He was 40.0 μmol/m^2, which exceeds $n_{\rm fp} = 30.1$ μmol/m^2. The small gradual increase in δf of ^{3}He by increasing n indicates an increase of the inert layer thickness by applying the pressure on it.

3.2 Model and analysis

3.2.1 Subtraction of the background

The temperature dependence of f and Q^{-1} in Fig. 3.2 is typical of a relaxational crossover under ac stress [94]. Assuming that the relaxation is caused essentially by adsorbed helium, the relaxational contribution to f and Q^{-1} is obtained by subtraction of the background from the raw data. We define the resonant frequency shift and the excess energy dissipation by

$$\delta f(T) \equiv f(T) - f_{\rm B}(T) - [f(T_{\rm max}) - f_{\rm B}(T_{\rm max})], \tag{3.1}$$

and

$$\delta Q^{-1}(T) \equiv Q^{-1}(T) - Q_{\rm B}^{-1}(T). \tag{3.2}$$

where $T_{\rm max} = 1.0$ K, and the background $f_{\rm B}(T)$ and $Q_{\rm B}^{-1}(T)$ are given in Chapter 2. By this definition of δf, we have omitted the background and the small constant frequency increments that were seen for all coverages (see f at high temperatures in Fig. 3.2), so as to set $\delta f = 0$ at $T_{\rm max}$. The temperature-independent extra background is attributed to adsorption of atoms in particularly deep potential sites on the disordered substrate, and this omission was necessary for the fitting of data to the response function given later. The definition of δQ^{-1} was sufficient for the data of ^{4}He, but we have added a small constant to set $\delta Q^{-1}(T_{\rm max}) = 0$ for the data of ^{3}He.

Figure 3.4 shows a normalized resonant frequency shift $2\delta f/f_0$ and an excess dissipation δQ^{-1}. At the critical coverage, $n_{\rm c} = 23$ and 20 μmol/m^2 for ^{4}He and ^{3}He respectively, $2\delta f/f_0$ is linear to $\log(T)$ in the ^{4}He case, but is constant in the ^{3}He case. By further increasing n from $n_{\rm c}$, $2\delta f/f_0$ and δQ^{-1} do not change in the displayed resolution.

Some features in the data in Fig. 3.4 are probably due to imperfection in the background subtraction. The normalized resonant frequency shift $2\delta f/f_0$ is rounded in both ^{4}He and ^{3}He probably because the subtraction was too much at lower temperatures. The excess dissipation δQ^{-1} becomes negative at low temperatures

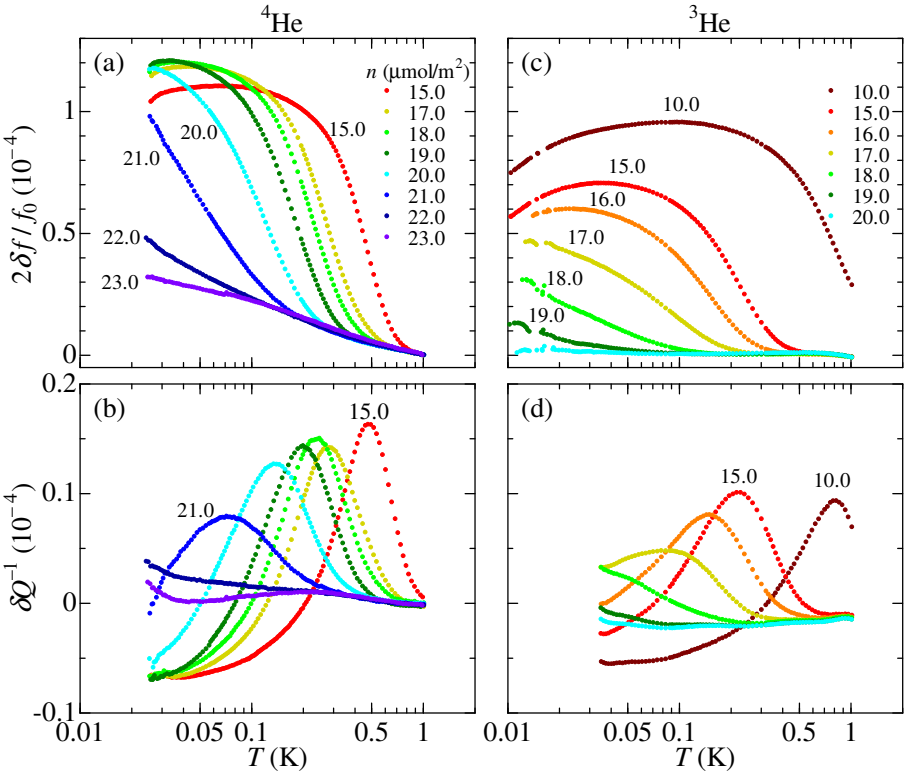

Figure 3.4: Normalized resonant frequency shift $2\delta f/f_0$ and excess dissipation δQ^{-1}. (a) and (b): ^{4}He, and (c) and (d): ^{3}He films.

for several coverages, meaning that helium adsorption decreases the internal loss of the glass. The physical origin of this apparently negative dissipation is not elucidated. This is possibly due to blocking of the motion in tunneling two-level systems in glass by helium adatoms [10]. The excess dissipation δQ^{-1} of ^{3}He between 0.01–0.03 K was abnormally enhanced and scattered, therefore we masked the data below 0.03 K for clarity. Except these features, the overall temperature dependence of $2\delta f/f_0$ and δQ^{-1} assures the existence of the elastic anomaly.

For the data in Fig. 3.4, we define a peak temperature T_p as a temperature at which the dissipation takes a peak. It can be considered as a crossover temperature between the stiff and the soft state. The coverage dependence of T_p will be shown later in Fig. 3.10, in which T_p approaches 0 K at $n = n_\mathrm{c}$ with a concave curvature.

3.2.2 Thermal activation model for anelastic relaxation

The relaxational crossover of the elastic anomaly is explained by the thermal activation model which was first proposed by Tait and Reppy in their heat capacity study [81]. Adsorbed helium atoms on a surface interact with strong hard-core repulsion, and form an energy band of localized and spatially-extended band which are separated by an energy gap E. At $T = 0$, all helium atoms are in the localized states. At finite temperatures, atoms are thermally excited to the extended states an energy gap. The excited atoms move freely along the substrate and act as a normal fluid. The thermal relaxation time is

$$\tau = \tau_0 e^{E/k_\mathrm{B}T}, \tag{3.3}$$

where τ_0^{-1} is an attempt frequency.

In the dynamical experiment at an angular frequency $\omega = 2\pi f$, when the relaxation time is much larger than the period of oscillation, i.e., $\omega\tau \gg 1$, the atoms are localized and contribute to the elasticity of the substrate. In the opposite situation, $\omega\tau \ll 1$, atoms are alternately excited and localized many times during the deformation of the substrate, therefore the elasticity of the helium–substrate composite system which we detect is equal to that of the substrate only. We analyze $2\delta f/f_0$ and δQ^{-1} by dynamic response functions for anelastic relaxation.

Anelasticity is defined as follows [94]: In ideal elasticity, the relation between stress and strain is *linear* (Hooke's law), *instantaneous* and *recoverable*. Anelasticity holds the *recoverability* and *linearity*, but does not the *instantaneousness*: The equilibrium is achieved after a sufficient time in anelastic material. Viscoelasticity does not hold the *recoverability*, *instantaneousness*, and often the *linearity*. In our case, the torsional oscillation is steady and the recoverability is not present, therefore anelastic response is the best to describe the observation.

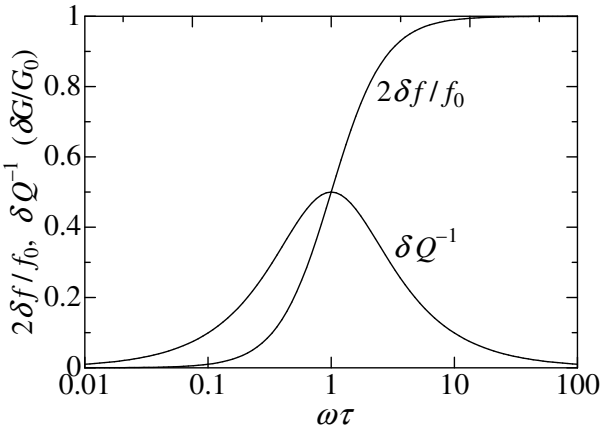

Figure 3.5: Dynamic response function from Eqs. (3.4) and (3.5).

According to similar anelasticity analysis for bulk solids [94], we have

$$\frac{2\delta f}{f_0} = \frac{\delta G}{G_0}\left[1 - \frac{1}{1+(\omega\tau)^2}\right], \tag{3.4}$$

$$\delta Q^{-1} = \frac{\delta G}{G_0}\frac{\omega\tau}{1+(\omega\tau)^2}, \tag{3.5}$$

where δG and G_0 are a relaxed shear modulus of the adsorbed film and a shear modulus of the torsion rod, respectively. As the torsion rod is a composite of the Gelsil, a thin Stycast 1266 epoxy and a thin beryllium copper tube, G_0 is an effective shear modulus of the composite torsion rod that holds $f_0 \propto \sqrt{k_0} \propto \sqrt{G_0}$, where k_0 is the torsion constant, introduced in Chapter 2, without adsorbed film . In our situation, $\delta G \ll G_0$ ($\delta f \ll f_0$). Therefore, when $\omega\tau \gg 1$,

$$f = f_0 + \delta f \propto \sqrt{G_0 + \delta G} \simeq G_0\left[1 + \frac{\delta G}{2G_0}\right]. \tag{3.6}$$

The $\omega\tau$-dependence of functions is shown in Fig. 3.5. We see that $2\delta f/f_0$ and δQ^{-1} are point- and mirror-symmetric to $\omega\tau$ in logarithmic scale. The normalized resonant frequency shift $2\delta f/f_0$ is maximal when $\omega\tau \gg 1$, at half-maximum with a maximal slope when $\omega\tau = 1$, and zero when $\omega\tau \ll 1$. The excess dissipation δQ^{-1} is maximal when $\omega\tau = 1$.

We regard $\omega = 2\pi f \simeq 2\pi f_0$ as a constant. The relaxation time τ is a temperature-dependent variable from Eq. (3.3), and we can change τ from zero to infinite by simply changing the temperature T. Another expressions of the thermal

relaxation time are

$$\ln(\omega\tau) = \ln(\omega\tau_0) + E/k_{\mathrm{B}}T. \tag{3.7}$$

Therefore, $2\delta f/f_0$ and δQ^{-1} are also symmetric to $1/T$. The upper abscissa in Fig. 3.5 is such an axis which is normalized with a peak temperature $T_{\mathrm{p}} = -E/[k_{\mathrm{B}} \ln(\omega\tau_0)] > 0$ at which δQ^{-1} takes a peak.

3.2.3 Distribution function for the energy gap

For a Debye relaxation process of a single-valued activation energy, $2\delta f(T \to 0)/f_0$ is twice as large as $\delta Q^{-1}(T_{\mathrm{p}})$ from Eqs. (3.4) and (3.5). The experimental results in Fig. 3.4 give, however, $[2\delta f/f_0(T_{\mathrm{min}})]/\delta Q^{-1}(T_{\mathrm{p}}) > 2$ as far as the δQ^{-1} peak is distinguishable. A Cole–Cole plot (Argand plot) in Fig. 3.6 shows that the observed elastic anomaly draws a deformed semicircle. The semicircle is a Debye relaxation with a single-valued relaxation time τ. The deformed semicircle means that the relaxation time has a distribution.

As the adsorption potential is disordered and adatoms form a non-crystalline film, it is natural to consider that the energy gap E has a distribution. We assume a lognormal distribution,

$$F(E) = \frac{1}{\sqrt{2\pi}\sigma E} \exp\left(-\frac{[\ln(E/\Delta)]^2}{2\sigma^2}\right), \tag{3.8}$$

where Δ is a median (a value separating the higher half of the population from the lower half) and σ is a dimensionless parameter. We hereafter regard Δ as the energy gap. The choice of the lognormal distribution, not a normal (Gaussian) distribution, is suitable for a symmetric shape of the peak of δQ^{-1} against logscale temperature. The lognormal distribution appears in attempts to interpret elastic aftereffect functions, dielectric relaxation phenomena [94], and an elastic relaxation in bulk solid ^{4}He [114]. We obtain a complex form of the dynamic response function as

$$\frac{2\delta f}{f_0} = \frac{\delta G}{G_0}\left[1 - \int_0^\infty \frac{F(E)}{1+(\omega\tau)^2} dE\right], \tag{3.9}$$

$$\delta Q^{-1} = \frac{\delta G}{G_0} \int_0^\infty \frac{F(E)\omega\tau}{1+(\omega\tau)^2} dE. \tag{3.10}$$

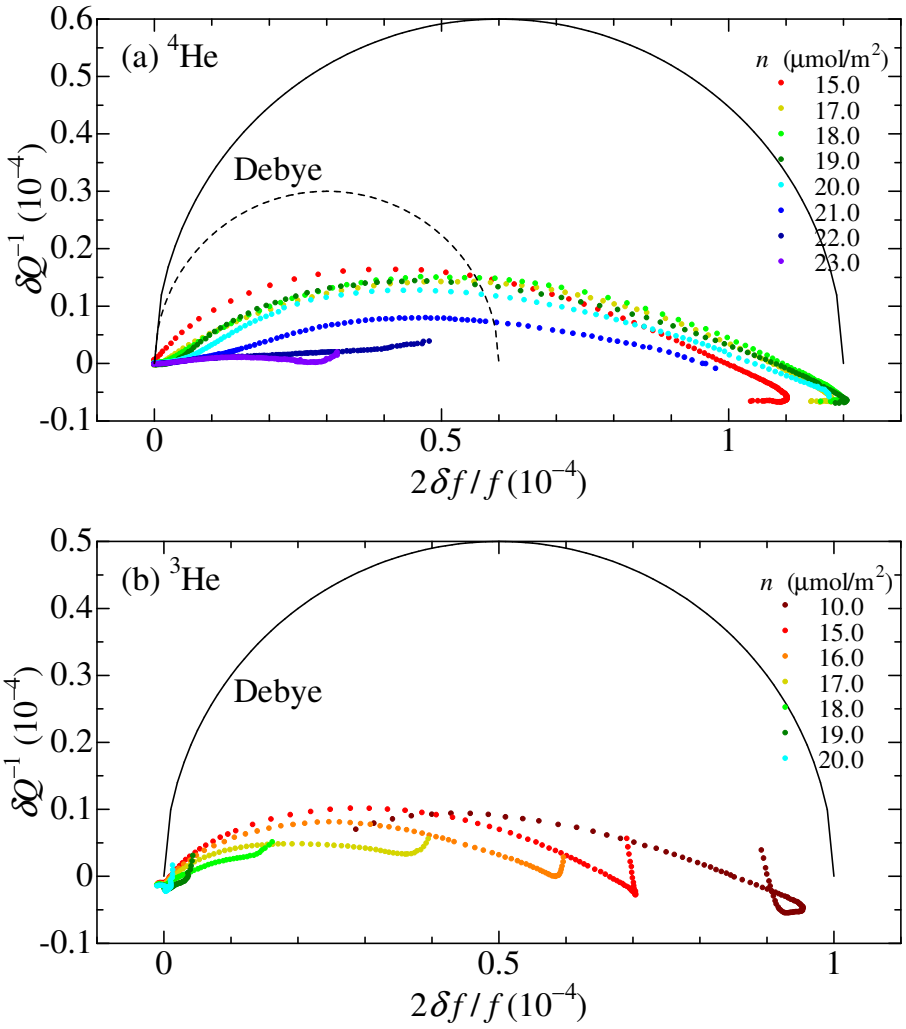

Figure 3.6: Cole–Cole plot of (a) ^{4}He and (b) ^{3}He films' data. The scales of the vertical to horizontal axis are equivalent. The semicircles describe Debye relaxation (single τ).

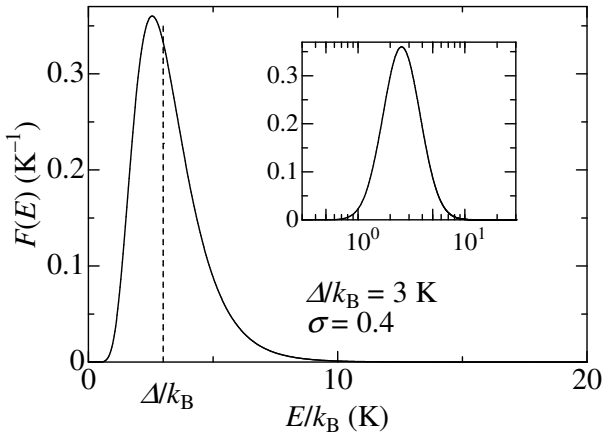

Figure 3.7: Lognormal distribution function. The vertical dashed line separates the higher half of the population from the lower half, therefore the areas of both sides are the same. In the inset, the shape of the distribution function is symmetric because the horizontal axis is in logscale.

3.2.4 Fittings

We perform fittings of the dynamic response function with the lognormal distribution to the data. Actually, we numerically did the integration by

$$\frac{2\delta f}{f_0} = \frac{\delta G}{G_0}\left[1 - \sum_{E=E_{\min}}^{E_{\max}} \frac{\delta E}{\sqrt{2\pi}\sigma E} \exp\left(-\frac{[\ln(E/\Delta)]^2}{2\sigma^2}\right) \frac{1}{1+(\omega\tau)^2}\right], \quad (3.11)$$

$$\delta Q^{-1} = \frac{\delta G}{G_0} \sum_{E=E_{\min}}^{E_{\max}} \frac{\delta E}{\sqrt{2\pi}\sigma E} \exp\left(-\frac{[\ln(E/\Delta)]^2}{2\sigma^2}\right) \frac{\omega\tau}{1+(\omega\tau)^2}, \quad (3.12)$$

with the number of samples 1000, $E_{\max}/E_{\min} = 10^4$, and $E_{\min} \ll k_B T_p \ll E_{\max}$. We found this condition was sufficient as increasing the number of samples or extending the range do not alter the results. The fittings were done by searching manually the best fit of the peak in Eq. (3.12) to the δQ^{-1} data. The position of the peak was strongly dependent on Δ. We used common parameters in Eqs. (3.11) and (3.12). The results of fitting are shown with solid curves in Figs. 3.8 and 3.9. Equations (3.11) and (3.12) fit well to the data, and the negative δQ^{-1} below 0.1 K does not have much influence on the quality of the fittings. From the fittings, we get Δ, $\delta G/G_0$, τ_0 and σ as fitting parameters. We found that Δ is strongly n-dependent and discuss it in the next section. The inverse attempt frequency τ_0 is ranged from

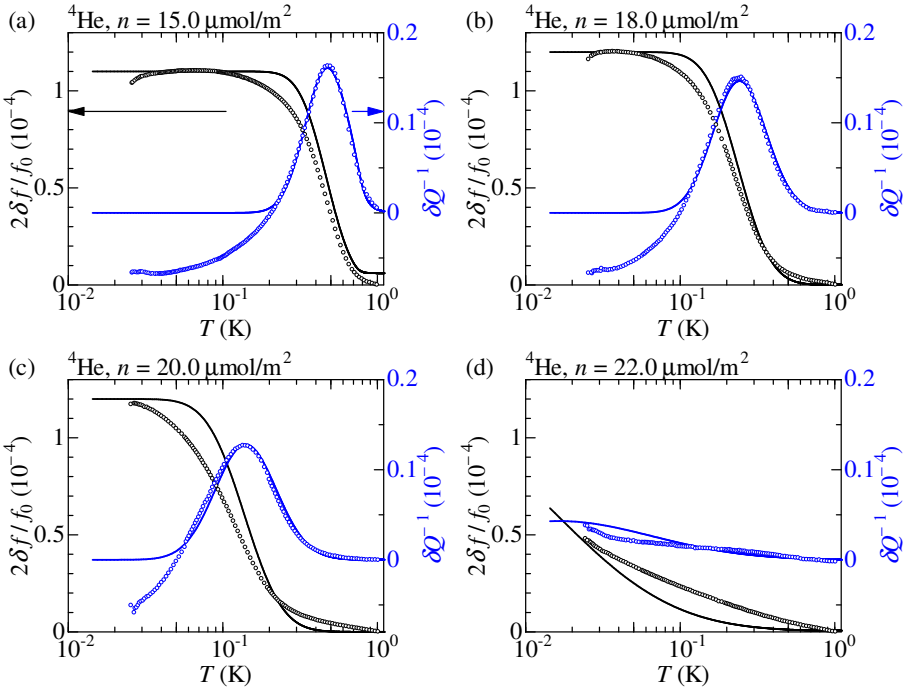

Figure 3.8: Normalized resonant frequency $2\delta f/f_0$ and excess dissipation δQ^{-1} for ^{4}He films at four coverages. Solid lines are the results of fitting to the complex response functions with a lognormal distributed energy gap (see the text).

0.4 to 0.6 ns, $\sigma = 0.31$–1.4, and $\delta G/G_0 = 0.7 \times 10^{-4}$–$1.2 \times 10^{-4}$ for ^{4}He and ^{3}He.

3.2.5 Coverage dependence of the energy gap and the dissipation peak temperature

The coverage dependence of the energy gap Δ and the dissipation peak temperature T_p are shown in Fig. 3.10. Both Δ and T_p smoothly decrease to 0 K as n approaches n_c. We find a remarkable relation between Δ and T_p, $\Delta \simeq 13 k_B T_p$, for both ^{4}He and ^{3}He, as clearly shown in Fig. 3.10. This relation between Δ and T_p reinforces the validity of the fittings. The relation $\Delta \simeq 13 k_B T_p$ holds the aforementioned relation $1 = \omega\tau \simeq \omega\tau_0 e^{13}$ in the anelastic dynamic response function.

Figure 3.10 shows that Δ and T_p decrease monotonically with some scatters. The gap is fitted by a power law

$$\Delta = \Delta_0 |1 - n/n_c|^a. \tag{3.13}$$

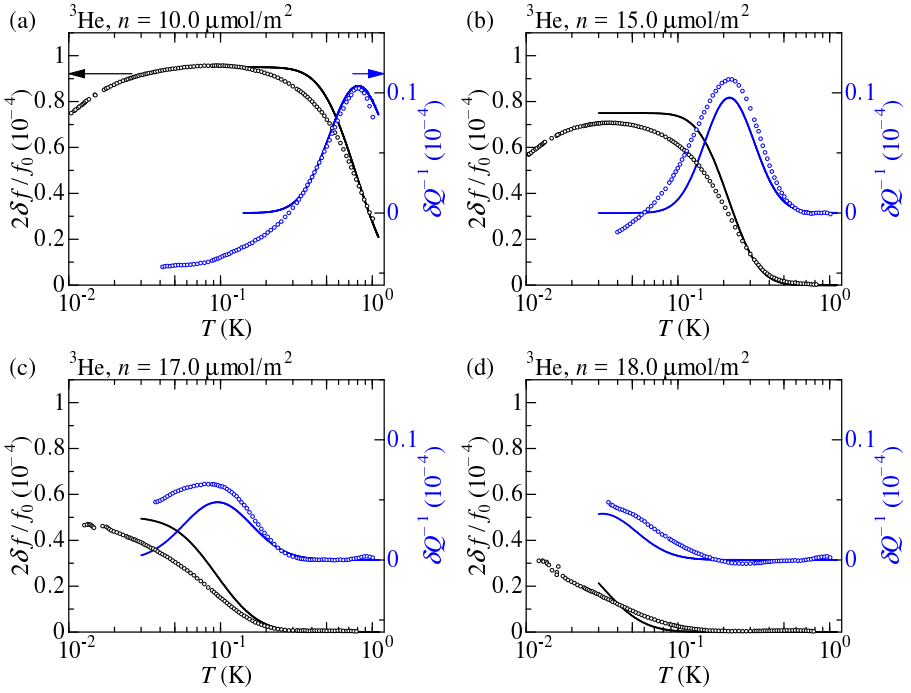

Figure 3.9: Normalized resonant frequency $2\delta f/f_0$ and excess dissipation δQ^{-1} for ^{3}He films at four coverages. Solid lines are the results of fitting to the complex response functions with a lognormal distributed energy gap (see the text).

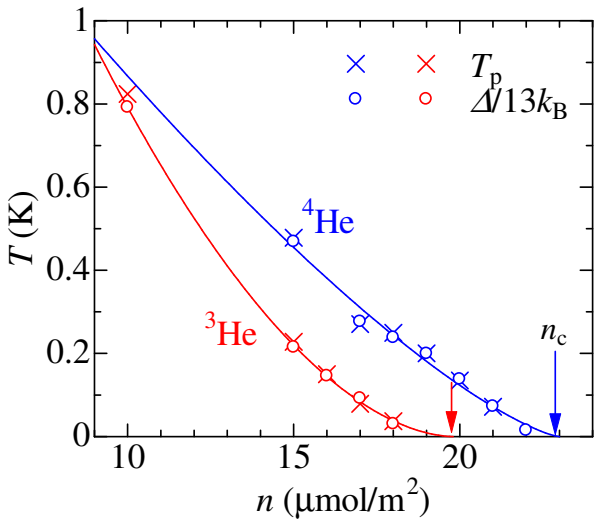

Figure 3.10: Dissipation-peak temperature T_p, and the energy gap Δ obtained from the fittings as a function of the coverage. Solid curves are power law fits for Δ from Eq. 3.13. Arrows indicate critical coverage n_c.

Nonlinear fittings give $\Delta_0/k_B = 23.9$ K, $n_c = 23.0$ μmol/m^2, and $a = 1.32$ for ^{4}He, and 36.5 K, 19.8 μmol/m^2, and 1.80 for ^{3}He, respectively. The exponent larger than 1, $a > 1$, means that the curvature is concave.

3.2.6 Energy band and compressibility

The fact that Δ decreases smoothly to zero as $n \rightarrow n_c$ indicates that the energy band also changes smoothly with n. We propose an energy band in Fig. 3.11. The localized states are completely filled at $T = 0$, and its uppermost edge is determined by n. Atoms in the localized states contribute to the elasticity. On the other hand, the extended states are empty at $T = 0$, and their lowermost edge, μ_0, has no or a negligible dependence on n. At high T, helium atoms are thermally excited from the localized to the extended states, resulting in a softening. At $n \geq n_c$, the gap is closed, and helium atoms can enter the extended states even at $T = 0$. ^{4}He atoms condensed in the extended states show superfluidity. This scenario was first discussed by Crowell *et al.* in a heat capacity study of ^{4}He films [7, 82].

The band for each n is analogous to that of an intrinsic semiconductor. The chemical potential μ at $T = 0$ is a function of n and is located at the middle of the

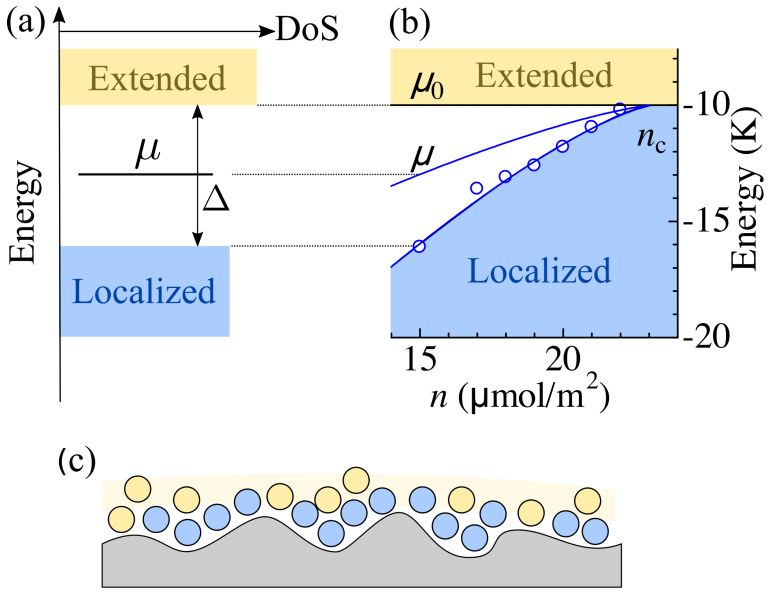

Figure 3.11: (a) Proposed energy band for helium films. (b) Coverage dependence of the edge of the energy band (with ^{4}He data). (c) Cartoon of helium atoms on the substrate in real-space. The blue atoms are localized, and the yellow atoms are in the spatially-extended mobile state.

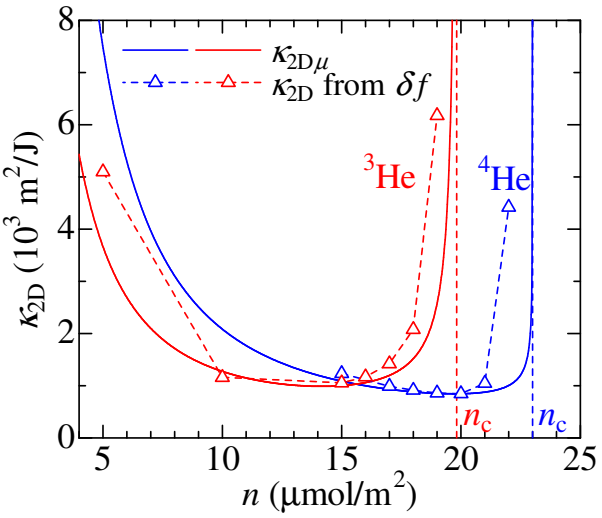

Figure 3.12: 2D compressibility of ^{4}He and ^{3}He films. Solid curves show $\kappa_{2D\mu}$ from Eq. (3.16) and triangles show κ_{2D} directly obtained from δf using Eq. (3.17).

gap, so that

$$\mu(n) = \mu_0 - \frac{\Delta(n)}{2}. \tag{3.14}$$

The 2D compressibility is, by definition,

$$\kappa_{2D\mu} = \left(N_A n^2 \frac{\partial \mu}{\partial n} \right)^{-1}, \tag{3.15}$$

where N_A is the Avogadro constant ($N_A n$ is a 2D number density of atoms). We refer to the 2D compressibility obtained from $\mu(n)$ as $\kappa_{2D\mu}$. From Eqs. (3.13), (3.14) and (3.15), we get

$$\kappa_{2D\mu} = \frac{2n_c}{aN_A n^2 \Delta_0} |1 - n/n_c|^{1-a}. \tag{3.16}$$

The results are drawn in Fig. 3.12 with solid curves.

The 2D compressibility is also obtained by directly comparing the observed frequency increment $\delta f(n)$ with Eq. (2.5), the FEM result. Here $\delta f(n)$ is a frequency increment from $f(n_c)$ at the lowest temperature. We use $f(n_c)$, not $f(n = 0)$, as the reference value because $f(n_c)$ contains the elastic contribution from atoms in deep potential sites, which we want to exclude from the calculation.

The shear modulus of Gelsil is $G_{g0} = 7.38$ GPa from an ultrasound study [105]. With a general relation $K = \lambda + (2/3)G$, where K is a bulk modulus and λ is a Láme constant, an effective 3D compressibility of helium film κ is $\kappa^{-1} = \delta K \simeq (2/3)\delta G$. It is converted to the 2D compressibility by $\kappa_{2D} = \kappa/d$, where $d = v_{film}n$ is the mean film thickness and v_{film} is the molar volume of helium film. Since v_{film} is unknown, we employ the molar volume v of liquid helium at 0 bar in Table 1.3. The actual molar volume of the thin helium film v_{film} should be smaller than v due to van der Waals attraction from the substrate [52]. Combining these equations, we have

$$\kappa_{2D} = \frac{0.148 f_0}{\delta f(n) G_{g0} v n}. \tag{3.17}$$

In Fig. 3.12, we plot κ_{2D} obtained from Eq. (3.17) with triangles. The overall agreement between $\kappa_{2D\mu}$ and κ_{2D} from δf definitely ensures the proposed band. In both ^{4}He and ^{3}He, κ_{2D} first decreases, then makes a plateau, and finally shows divergent behavior as n approaches n_c. The discrepancy near $n = n_c$ is because the experimental lowest temperature was limited to a finite temperature about 20 mK.

3.3 Discussion

The universality in ^{4}He and ^{3}He films is revealed by constructing a "unified" phase diagram shown in Fig. 3.13. The peak temperatures T_p's of ^{4}He and ^{3}He as a function of n/n_c nearly collapse onto each other, except that the curvatures differ. The difference of the zero-point energy, hence the binding energy from the substrate, between ^{4}He and ^{3}He does not affect the magnitude of the characteristic temperatures of the elastic anomaly.

Superfluid transition temperatures T_c's of ^{4}He on Gelsil in a previous torsional oscillator study [49] are also plotted in Fig. 3.13. The critical coverage for it was inferred to be $n_c = 20$ μmol/m^2, which is slightly smaller than 23 μmol/m^2 obtained from the elastic anomaly. The nominal pore diameters were 2.5 nm for both porous Gelsil samples, but they were provided by different manufacturers. The discrepancy in n_c might be originated from differences in some characteristics such as residual impurities, pore size and its distribution between two samples.

In a previous torsional oscillator study in Chapter 1, a torsional oscillator with a Gelsil in the bob (named TO1) has detected both the superfluid transition and the elastic anomaly, the latter is confirmed by the present study. The two characteristic temperatures, T_p and T_c, meet at the same critical coverage $n_c = 22$ μmol/m^2 in the experimental resolution (see Fig. 1.16 in Appendix B). A heat capacity study by Crowell *et al.* [7] may also suggests the common critical coverage for "T_B" and T_c, though the physical meaning of T_B, a crossover temperature of the heat capacity at

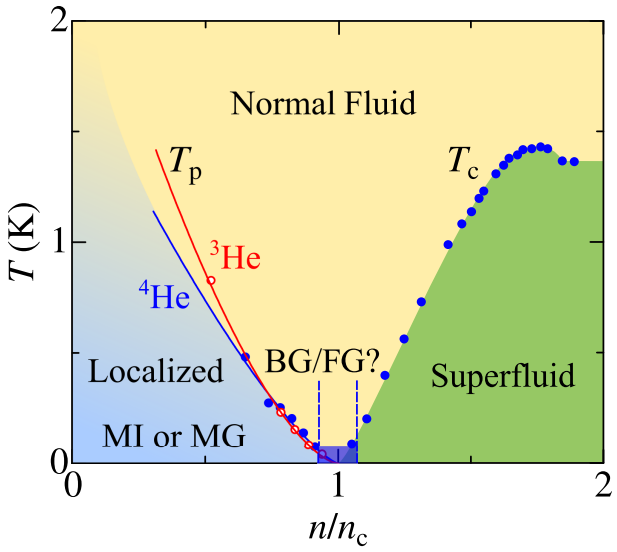

Figure 3.13: Unified phase diagram of helium films on a disordered Gelsil substrate constructed by the crossover temperature T_p and the superfluid transition temperature T_c (only for ^{4}He, from Ref. [49], $n_c = 20$ μmol/m^2). The curve of T_p divides the localized phase from the normal fluid phase. The localized phase near $T = 0$ is a sort of Mott insulator (MI) or Mott glass (MG). A possible region for Bose glass (BG) or Fermi glass (FG) is shown.

$n < n_c$, is not clear. Further experimental studies in the vicinity of n_c is necessary to conclude that the n_c's of the superfluidity and the elastic anomaly are exactly identical or slightly different.

Figures 3.10 and 3.13 show that $\Delta(n)$ and T_p obey a power law $\Delta \propto T_p \propto |n - n_c|^a$ with $a > 1$. A symmetry may exist between the critical exponent of Δ and that of superfluid T_c of ^{4}He films, in which $T_c \propto (n - n_c)^w$ with $w > 1$ in all previous results [7, 63].

Our finding is that ^{4}He and ^{3}He films at $n < n_c$ are identically *gapped* and *compressible* irrespectively of quantum statistics. These features do not strictly agree with the properties of Bose glass (gapped, compressible, for ^{4}He) [6], Mott insulator (gapped, incompressible) or Mott glass (single-particle gap, incompressible) [80].

We propose, however, that the localized helium film is a sort of Mott insulator or Mott glass in a realistic situation. One may consider the following model: Helium atoms are first adsorbed on some particularly deep adsorption sites, so as to weaken randomness. Additional helium atoms are adsorbed on the weakened potential

surface, and self-organize a nearly spatially periodic 2D Mott insulator or Mott glass with an n-dependent lattice spacing. The self-organization of sites allows a finite compressibility. The gap is finite because "sites are fully occupied" and an atom needs a finite energy to move.

Tackling this problem is important because it is related the nature of the onset of superfluidity, the quantum critical phenomena and the boson and fermion localization. Theoretical, numerical, and more experimental works are desired.

The gapped localized state that terminates at a certain coverage (n_c) has been observed in helium films on various substrates, such as Vycor [7, 81], Hectorite (2D flat substrate), FSM (1D pores), and zeolites [65]. This suggests that the gapped localized Mott insulator or Mott glass exists ubiquitously, irrespective of substrate randomness and dimensionality.

As to the ^{4}He films, our result does not reject the possibility of Bose glass in the vicinity of $n = n_c$, where the gap is almost closed and the compressibility increases significantly. Theories predict Bose glass emerging between a Mott insulator and superfluid in the presence of moderate disorder [6]. A previous experiment discussed a quantum critical behavior of possible Bose glass near n_c [7]. In our system, Bose glass can exist at about $22 < n < 23$ μmol/m^2, and a corresponding Fermi glass can occur in ^{3}He at $19 < n < 20$ μmol/m^2. Recently, quantum phase transitions among Mott insulator, Mott glass, Bose glass and Bose-Einstein condensate in a quantum magnet were reported [115]. Helium films in disordered substrates can pave the way for a new perspective of quantum phase transitions for the advantage of variable correlation and quantum statistics.

Chapter 4

Neon Film

In the neon experiment, I observed an elastic anomaly which is qualitatively similar to that of helium films in Chapter 3. In this chapter, I present and discuss the key features of the elastic anomaly of neon films (a coverage dependence of the elasticity at a low temperature limit, a height and temperature of the dissipation peak). The thermal activation model introduced in Chapter 3 is used to analyse the neon data.

The dissipation peak temperature T_p goes to 0 K as the coverage n approaches $n_\mathrm{c} \sim 20$ μmol/m^2 in helium films. In neon films, however, T_p does not decrease below 5 K. This indicates that neon film is close to a classical system, which does not show quantum phase transition and does not become superfluid. By this fact, we find that the elastic anomaly is not limited to the accompanying phenomenon of quantum phase transition, but is rather ubiquitous for adsorbed films on disordered substrate.

4.1 Experimental results

4.1.1 Raw data

We show raw data of the resonant frequency f and energy dissipation Q^{-1} at $n = 0$ and 10.0 μmol/m^2 in Fig. 4.1. When $n = 10.0$ μmol/m^2 of neon atoms are adsorbed, f and Q^{-1} increases slightly at $T > 10$ K. Below 10 K, f starts to deviate from the background T dependence and increases rapidly at temperatures from 7 to 3 K. At lower T, f returns to the same T dependence as the background. The dissipation Q^{-1} has a peak at 5.4 K, and it becomes lower than the background below 3 K. These behaviors are qualitatively the same as those observed in helium films below 1 K.

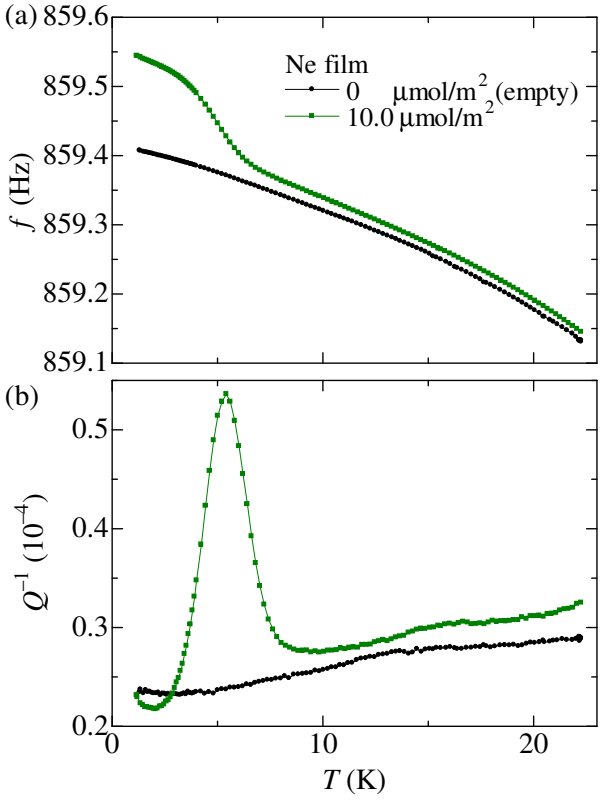

Figure 4.1: Raw data of (a) resonant frequency f and (b) energy dissipation Q^{-1} at neon coverages $n = 0$ (the background) and 10.0 μmol/m^2.

For a coverage $n = 10.0$ μmol/m^2, the frequency shift from the change in the density using Eq. (2.6) is −5 mHz. This is much smaller than the observed shift, +140 mHz, and is negative. Therefore, we conclude that the increase in f below 7 K originates from the increase in the elastic constant of the neon film.

4.1.2 Coverage dependence of the elastic anomaly

We define the frequency and excess dissipation shifts from the background as

$$\delta f(T) = f(T) - f_{\mathrm{B}}(T), \tag{4.1}$$

$$\delta Q^{-1}(T) = Q^{-1}(T) - Q_{\mathrm{B}}^{-1}(T), \tag{4.2}$$

where $f_{\mathrm{B}}(T)$ and $Q_{\mathrm{B}}^{-1}(T)$ are defined in Sect. 2.4.2. By these simple definitions, we can discuss the slight shifts in f and Q^{-1} between the finite coverage and the background data at high temperatures.

The T dependence of the normalized resonant frequency and energy dissipation shift, $2\delta f(T)/f_0$ and $\delta Q^{-1}(T)$, are shown in Figs. 4.2 and 4.3. The data with neon film ($n > 0$) have clear temperature and coverage dependences that are not present in the background ($n = 0$). The overall T dependence in $2\delta f(T)/f_0$ and $\delta Q^{-1}(T)$ definitely shows that neon films exhibit the elastic anomaly. From now, we discuss them using Fig. 4.2.

The normalized frequency shift $2\delta f/f_0$, i.e., the elasticity of the film, is almost constant at high and low temperatures, and changes in a range 3–15 K. At the lowest temperature $T_{\mathrm{min}} \simeq 1.2$ K, $2\delta f(T_{\mathrm{min}})/f_0$ increases monotonically with the coverage n from 4.5 to 30 μmol/m^2. We will show $2\delta f(T_{\mathrm{min}})/f_0$ as a function of n in Fig. 4.5 and discuss it later. At the highest temperature $T_{\mathrm{max}} = 22$ K, $2\delta f(T_{\mathrm{max}})/f_0$ is almost zero in the displayed resolution.

The peak of δQ^{-1} is located at the inflection point of δf. We define the temperature at the δQ^{-1} peak as T_{p}. At $n = (4.5 \pm 1.0)$ μmol/m^2, $T_{\mathrm{p}} \simeq 11$ K, while at higher coverages T_{p} stays at about 5 K with a slight coverage dependence. The dissipation peak grows in its height with increasing n up to 20 μmol/m^2. At higher coverages, the peak height saturates, and the dissipation becomes broadened at a high temperature side (6–10 K). The broadening is due to growth of a second dissipation peak at slightly higher temperatures. The excess dissipation $\delta Q^{-1}(T_{\mathrm{p}})$ and T_{p} as functions of n are shown in Figs. 4.5 and 4.6, respectively. As seen in Fig. 4.2 (b), the dissipation δQ^{-1} becomes negative below about 3 K. This apparently negative dissipation at low temperatures was also observed in the helium film measurements. On the other hand, δQ^{-1} above about 15 K is slightly positive. The disorder in δQ^{-1} at 20 K, seen only at (4.5 ± 1.0) μmol/m^2, synchronizes with pressure rise due to the melting of solid neon outside the Gelsil, which was mentioned in Chapter 2.

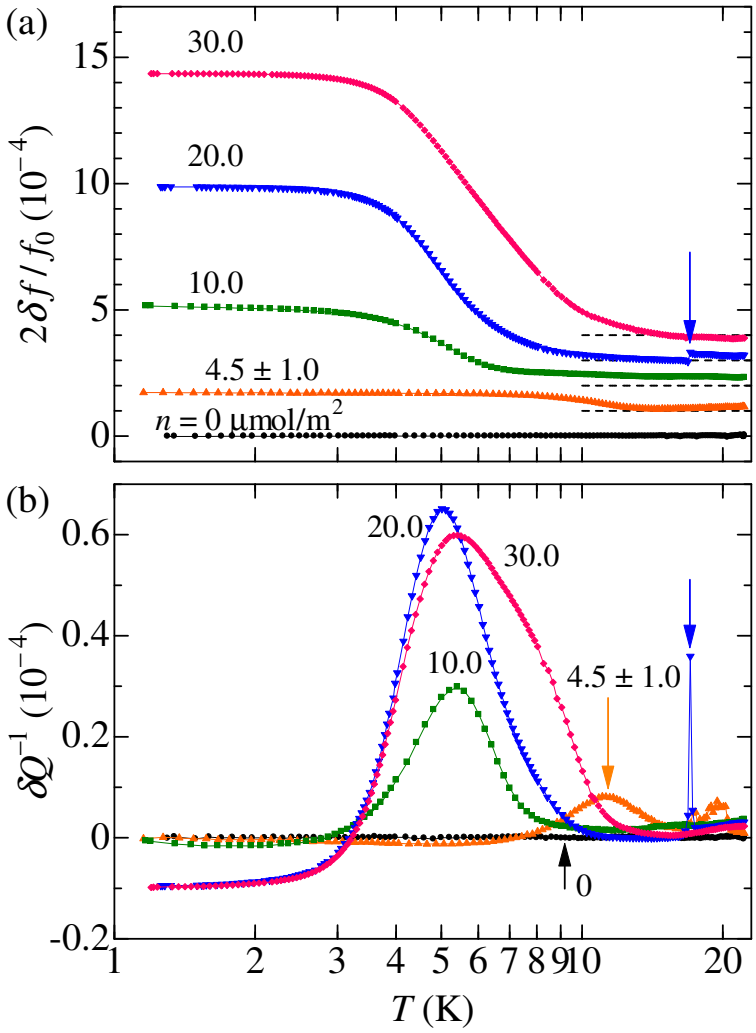

Figure 4.2: Temperature dependence of (a) normalized frequency and (b) energy dissipation shift for selected coverages. The constant frequency is taken to be f_0 = 859.133 Hz for every coverage. Data in (a) are vertically offset, indicated by dashed lines. The blue arrows indicate the anti-crossing and sharp dissipation peak.

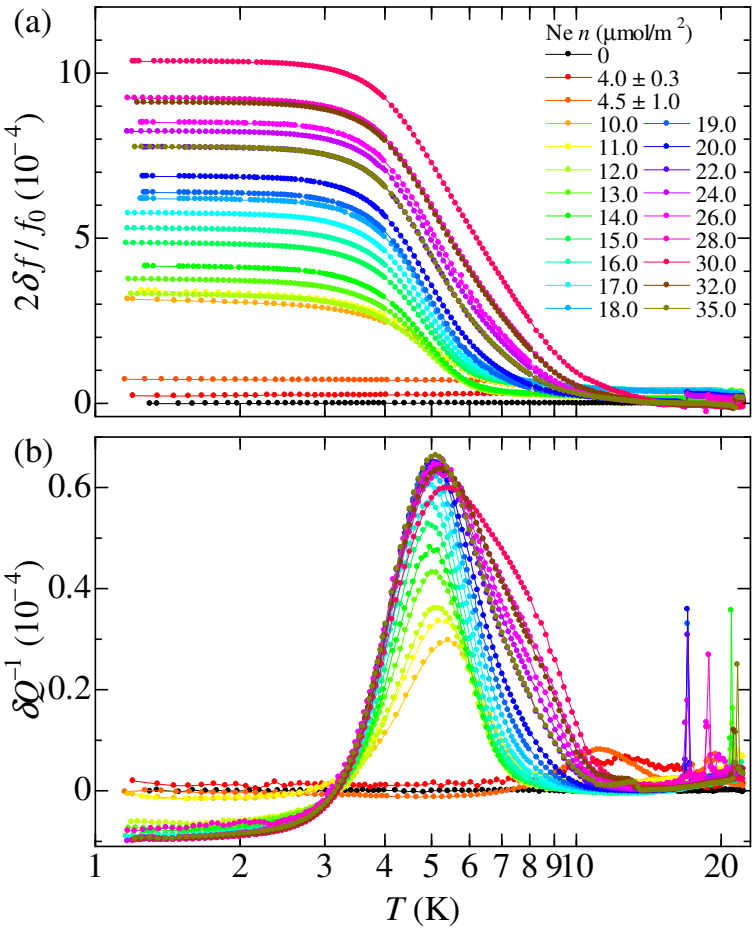

Figure 4.3: Temperature dependence of (a) normalized resonant frequency and (b) energy dissipation shift for all neon coverages. The color indicates the coverage. The base frequency is f_0 = 859.133 Hz for every coverage.

4.1.3 Anticrossing behavior

Besides the elastic anomaly, we observed an anticrossing behavior of the resonant frequency with a sharp dissipation peak. The anticrossing appears, for example, the $n = 20.0$ μmol/m^2 data in Fig. 4.2. The anticrossing occasionally emerged in the measurements of 13–35 μmol/m^2. The temperature of the anticrossing was ranged from 16 to 25 K and had no systematic dependence on the coverage.

We compare raw data of two successive coverages with and without anticrossing in Fig. 4.4. For $n = 18.0$ and 19.0 μmol/m^2, we have two anticrossings at 17.0 K and 22.2 K. In data of 19.0 μmol/m^2 cooling, we did a neon adsorption from 18.0 to 19.0 μmol/m^2 (at 25 K), an annealing (25 $\rightarrow$ 20 K), a liquid helium transfer (at 20 K), and a rapid cooling (20 $\rightarrow$ 1.2 K). The frequency shift indicated by a downward arrow at 20 K in Fig. 4.4 (a) is obviously from the vibration of the liquid helium transfer, and we omitted the change from the $n = 19.0$ μmol/m^2 data (the discrepancy in f-curves at 20–22 K is therefore apparent). We focus on the anticrossing at 17.0 K. The f-curve and peaked shape of Q^{-1} of 19.0 μmol/m^2 cooling and warming data overlap with each other, which means that the anticrossing is reproducible and reversible in T. The f-curves of 18.0 and 19.0 μmol/m^2 approximately overlay above 17.0 K, but separate below 17.0 K. This suggests that f at a low temperature side of the anticrossing decreases. The apparent discrepancy in f and Q^{-1} between 19.0 μmol/m^2 cooling and warming is because the actual temperature of the torsional oscillator cell is higher than the measured T due to the rapid cooling. If we cool sufficiently slowly, the apparent discrepancy vanishes.

The anticrossing clearly originates from a resonant coupling of some vibration mode (e.g., sound wave) in neon film or in porous glass to torsional oscillation, but it is yet to be elucidated. The anticrossing was not observed in helium and hydrogen films.

4.1.4 Coverage dependence

The normalized resonant frequency frequency shift $2\delta f(T_{\rm min})/f_0$ and the height of dissipation peak $\delta Q^{-1}(T_{\rm p})$ for all examined coverages are shown in Fig. 4.5. It is clearly seen that $2\delta f(T_{\rm min})/f_0$ is linear in n in a coverage range from 4 to 30 μmol/m^2. At 30 μmol/m^2, $2\delta f(T_{\rm min})/f_0$ shows a sharp maximum and then decreases. The open circles in Fig. 4.5 are values in which the effect of density change discussed in Eq. (2.6) are canceled. The overall coverage dependence of $2\delta f(T_{\rm min})/f_0$ is unchanged between the original and corrected values. The height of dissipation peak $\delta Q^{-1}(T_{\rm p})$ is also linear in n, but in a much narrower range from 4 to 18 μmol/m^2. Over the range, $\delta Q^{-1}(T_{\rm p})$ tends to saturate and shows

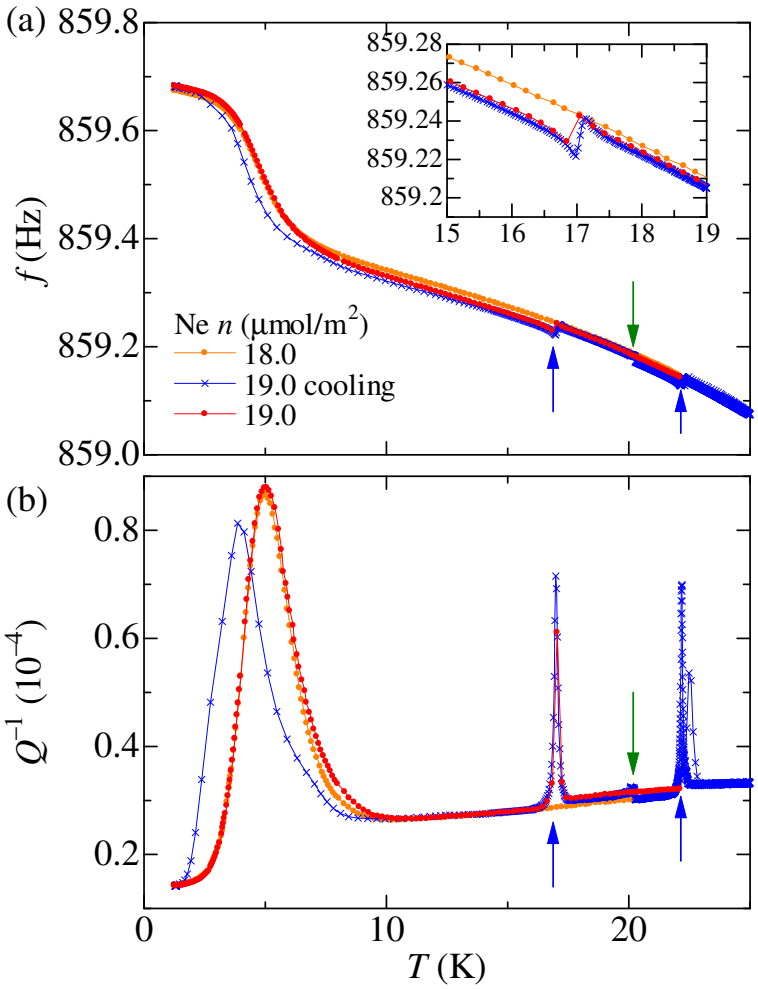

Figure 4.4: Comparison of raw data of (a) resonant frequency f and (b) energy dissipation Q^{-1} with and without the anticrossing (n = 19.0 and 18.0 μmol/m^2, respectively). The two upward blue arrows indicate the anticrossing, and the downward green arrow indicate a frequency shift due to liquid helium transfer. The inset is an expanded view.

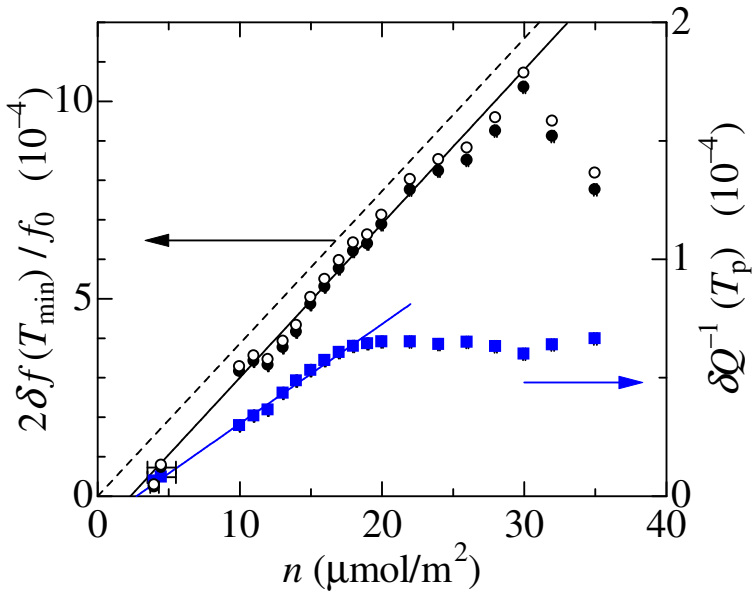

Figure 4.5: Coverage dependence of the normalized resonant frequency shift at $T_{\rm min} \simeq 1.2$ K and the energy dissipation at $T_{\rm p}$. Closed circles are $2\delta f(T_{\rm min})/f_0$ from Eq. (5.1), and open circles are values corrected for $\delta\rho_{\rm g}$. Solid lines are linear fittings, $y = a(n - n_{\rm offset})$. The dashed line is $2\delta f(0)/f_0$ from Eq. (4.3).

a shallow minimum at $n = 30$ μmol/m^2, the same coverage as that δf has a maximum. It is also clear that the linear fittings for both quantities do not pass the origin and have offset coverages. The results of fittings are $n_{\rm offset} = (2.3 \pm 0.5)$ and (2.7 ± 0.4) μmol/m^2 for $2\delta f(T_{\rm min})/f_0$ and $\delta Q^{-1}(T_{\rm p})$, respectively. The slopes are $a = (0.39 \pm 0.01)$ and (0.042 ± 0.001) (μmol/m^2)$^{-1}$ for $2\delta f/f_0$ and δQ^{-1}, respectively. The existence of offset coverage indicates that the first adsorbed neon atoms up to $n_{\rm offset}$ do not contribute to the elastic anomaly.

At the maximum of the normalized resonant frequency shift $2\delta f(T_{\rm min})/f_0$ at $n = 30$ μmol/m^2, the effective shear modulus $\delta G_{\rm g}$ is calculated to be 40.1 MPa by using $2\delta f(T_{\rm min})/f_0 = 1.07 \times 10^{-3}$, $G_{\rm g0} = 7.38$ GPa [105] and Eq. (2.5). As $2\delta f(T)/f_0$ does not change in a range 1.2–3 K and all neon atoms solidify at $T = 0$ in bulk, the stiff state is identified to be a solidlike localized state. The solidlike neon film is assumed to be an amorphous due to the disorder in adsorption potential. The effective shear modulus is smaller than the shear modulus of bulk solid neon $G_{\rm Ne} = 600$–900 MPa [116, 117], but it is reasonable for the following two reasons: (1) The neon film of $n = 30$ μmol/m^2 fills 36% of the entire volume of the pore.

(2) The porous structure reduces the effective shear modulus [118]. At the full pore coverage $n_{\rm fp} = 82.9$ μmol/m^2, the porosity of neon is $p_{\rm Ne} = 1 - p = 0.46$. There exist several attempt functions to describe the effective elastic modulus [118]. If we take $\delta G_{\rm g} = (1-p)^2 G_{\rm Ne}$, and assume a linearity $\delta f \propto n/n_{\rm fp}$, we have

$$\frac{2\delta f}{f_0} = 0.197 \frac{(1-p_{\rm Ne})^2 G_{\rm Ne}}{G_{\rm g0}} \frac{n}{n_{\rm fp}}. \tag{4.3}$$

This function is shown as the dashed line in Fig. 4.5, with $N_{\rm Ne} = 600$ MPa. The slopes of this assumption and the experimental data are almost identical. Therefore we conclude that the solidlike neon film has an identical elasticity to that of bulk solid.

On the other hand, in the soft state, $2\delta f(22\ {\rm K})/f_0 < 3 \times 10^{-5}$ (see Fig. 4.3), i.e., $\delta G_{\rm g} < 1$ MPa, for every coverage. Furthermore, $2\delta f(22\ {\rm K})/f_0$ does not change systematically by increasing n, which suggests that neon atoms in the soft state does not contribute to the elasticity. The large difference in $\delta G_{\rm g}$ between in the stiff and soft state suggests that the soft state is fluidlike. The fluidlike state appearing at temperatures much lower than the bulk triple point temperature 24.6 K might be realized by a strong supercooling of thin neon films in nanometer scale pores.

The coverage $n = 18$ μmol/m^2 at which $\delta Q^{-1}(T_{\rm p})$ starts to saturate is close to the monolayer coverage $n_1 = 21.0$ μmol/m^2. It is supposed that atoms adsorbed on porous glass do not form distinct layer structures but form an amorphous film. However, neon atoms can fill firstly all adsorption sites adjacent to the substrate at $n = n_1$, then further atoms are adsorbed on the already-adsorbed neon atoms. In such a situation, adatoms that are closer to substrate influence more prominently the dynamical response than adatoms farther from substrate does. The saturation of $\delta Q^{-1}(T_{\rm p})$ above 18 μmol/m^2 suggests that the first layer in contact with the glass surface mostly contributes to dissipation, although second layer still contributes to the elasticity ($2\delta f(T_{\rm min})/f_0$).

The elastic anomaly is characterized by the dissipation peak temperature $T_{\rm p}$. The coverage dependence is shown in Fig. 4.6, which is displayed as a phase diagram. We consider $T_{\rm p}$ as a crossover temperature between the stiff state at low T and the soft state at high T. For neon films, $T_{\rm p}$ decreases rapidly in a range 4–10 μmol/m^2, but does not decrease below 5 K by further increasing the coverage up to 35 μmol/m^2, roughly 1.7 layers. The n–$T_{\rm p}$ curve has a shallow minimum at 15 μmol/m^2, and a cusp at 30 μmol/m^2, the coverage at which $2\delta f(T_{\rm min})/f_0$ and δQ^{-1} show features.

As we have seen, the elastic anomaly of neon films at each coverage is qualitatively similar to that of helium films. In each phase diagram of ^{4}He and ^{3}He films, however, $T_{\rm p}$ approaches 0 K and vanishes at a critical coverage $n_{\rm c} \simeq 20$ μmol/m^2.

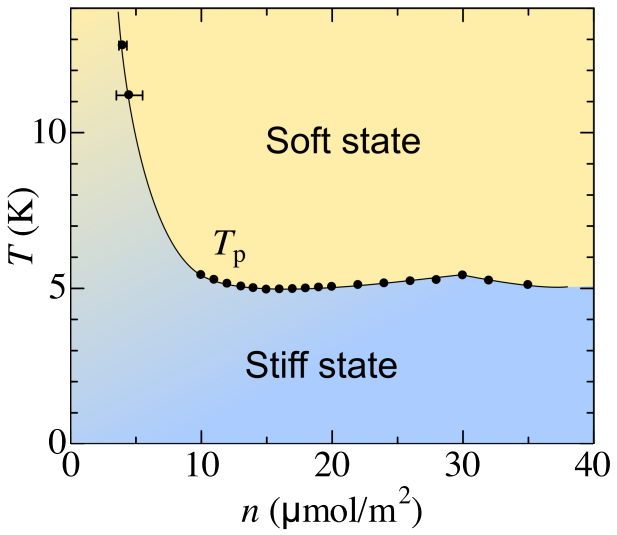

Figure 4.6: Phase diagram of neon film on a porous Gelsil glass. The boundary is the dissipation peak temperature T_p.

So the elastic anomaly of helium films is linked to the gapped solid phase of the one side of a (super)fluid–insulator quantum phase transition. On the other hand, T_p of neon does not decrease below 5 K. This indicates that neon film is close to a classical system, which does not show quantum phase transition and does not become superfluid. Therefore, the elastic anomaly is not limited to the accompanying phenomenon of quantum phase transition, but is rather originated generally from the energy structure of adsorbed films.

4.2 Analysis using the thermal activation model

For helium films, the elastic anomaly was explained by thermal activation of localized atoms [7, 81] and anelastic relaxation [8, 94]. Adsorbed atoms on surface interact by weak van der Waals attraction and strong hard-core repulsion, and form an energy band of localized states and extended states which are separated by a gap E. At $T = 0$, all atoms occupy the localized states. At a finite temperature comparable to the energy scale of the gap, atoms are thermally excited from the localized to extended states with a thermal relaxation time $\tau = \tau_0 e^{E/k_B T}$, where τ_0^{-1} is an attempt frequency. Using the dynamic response functions with a lognormal distribution of the energy gap, we introduced fitting functions, Eqs. (3.11) and

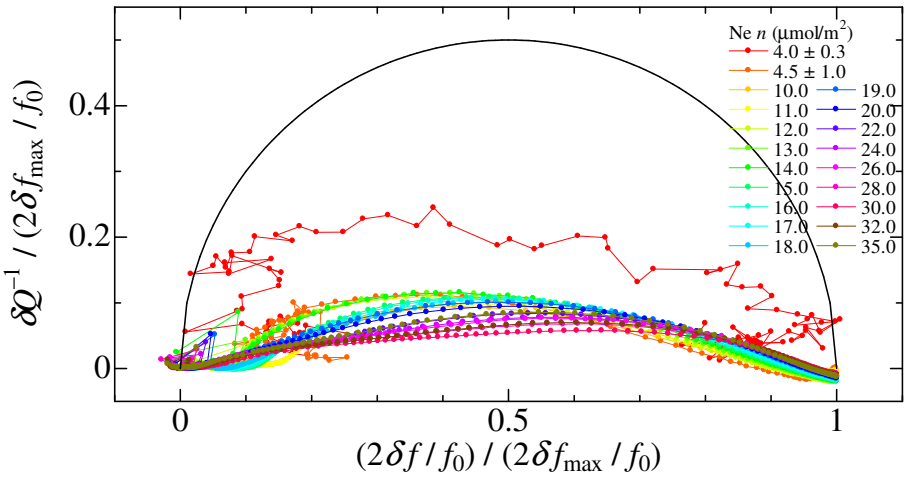

Figure 4.7: Cole–Cole plot of neon film data. The denominator $\delta f_{\max}$ is taken to be $\delta f(T_{\min})$ except for $n = (4.0 \pm 0.3)$ μmol/m^2 data. The solid curve is a semi-circle for Debye relaxation.

(3.12), in Chapter 3.

Figure 4.8 shows fittings of equations with $n = 18.0$ μmol/m^2 data. The fitting of $2\delta f/f_0$ to Eq. (3.4) is excellent. We refer to this fitting as fit-0. However, the parameter used in fit-0 gives a poor result in fitting δQ^{-1} data to Eq. (3.5). In particular, the symmetric shape in δQ^{-1} data is not reproduced.

In fit-f, the lower temperature shoulder of $2\delta f/f_0$ matches well with the data. The higher temperature shoulder slightly mismatches. The position and the symmetry of the dissipation peak of fit-f also agree with those of the data. The value of inverse attempt frequency $\tau_0 = 0.4$ ns and the ratio $\Delta/k_B T_p = 13$ were common to helium films [8]. The width and height of δQ^{-1} in fit-f, however, disagree with the experimental results.

We attempt in fit-Q to match a fitting curve with δQ^{-1} data. The width and height of dissipation are decreased by lowering τ_0 by several orders of magnitude. We get $\tau_0 = 4$ fs and $\Delta/k_B = 122$ K ($\Delta/k_B T_p = 24$) as fitting parameters. From fit-Q's of other coverages, we get τ_0's of the order of femtosecond or much smaller values. Fit-Q agrees better than fit-f with the experimental data in the entire temperature range. The resulted τ_0 is, however, too small to clarify the physical meaning. It is unlikely that neon has such a larger attempt frequency τ_0^{-1} than helium in several orders of magnitude. If we take the distribution of the energy gap is roughly equal to the median Δ, the product $\tau_0\Delta \sim 10^{-36}$ Js is smaller than the

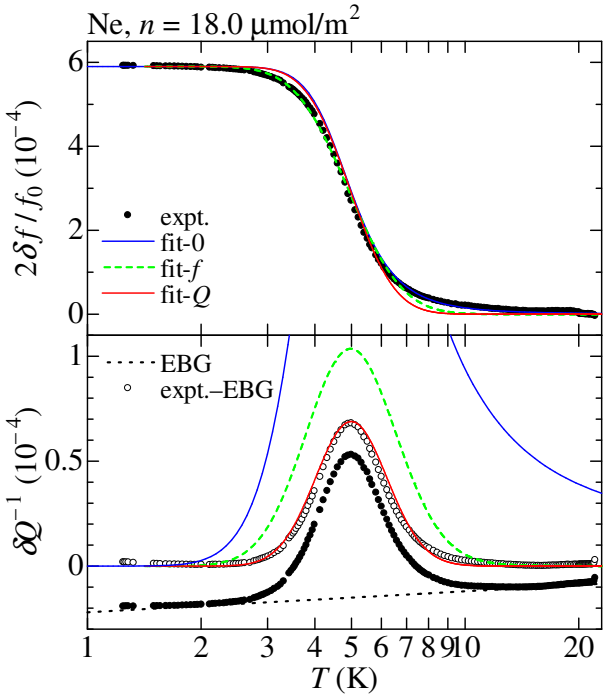

Figure 4.8: Experimental data with $n = 18$ μmol/m^2 and results of fittings. Closed circle data were determined using Eqs. (5.1) and (5.2). Open circles of δQ^{-1} are data from which an extra background (EBG) proportional to $\log(T)$ (black dotted line) was subtracted. The closed circles and the dotted line in (b) are shifted by -0.1×10^{-4}. Fit-0 gives $\tau_0 = 5$ μs and $E/k_B = 18$ K. Fit-f (green dashed curves) are to match with $2\delta f/f_0$, and fit-Q (red solid curves) are with δQ^{-1}. Fitting parameters for fit-f (fit-Q) were $\delta G/G_0 = 5.9 \times 10^{-4}$ (the same), $\tau_0 = 4 \times 10^{-10}$ (4×10^{-15}) s, $\Delta/k_B = 64$ (122) K, and $\sigma = 0.25$ (0.21).

Plank constant h, and this violates the time–energy uncertainty principle. Further physical insights for the model and fitting are necessary for this problem.

4.3 Phase diagram of neon film

We propose a phase diagram by the coverage dependence of the dissipation peak temperature $T_{\rm p}$. It is shown in Fig. 4.6. The dissipation peak temperature strongly depends on coverage below $n = 10$ μmol/m^2, but above that coverage it becomes almost constant. There is a cusp in the n–$T_{\rm p}$ curve at $n = 30$ μmol/m^2, the same coverage at which both $\delta f(T_{\rm min})$ and δQ^{-1} show the features.

One may regard $T_{\rm p}$ as the temperature that distinguishes two states of neon film, a stiff and a soft state. If each of the states corresponds to different phases, there exists only two phases in neon films adsorbed on porous glass. This contrasts with the five phases of submonolayer neon film on graphite [41, 86]. Similar situation has been found in helium: There are two phases at $T = 0$, a gapped solid and a mobile (superfluid) phase in ^{4}He and ^{3}He films on porous Vycor glass and on Gelsil [7, 8], while helium on graphite shows a number of phases depending on coverage [36, 37]. The disordered potential provided by porous glass makes the phase diagram more plain.

4.4 Discussion

In each coverage, the elastic anomaly of neon films is qualitatively identical to that of helium films. There exists, however, an important difference. In each phase diagram of ^{4}He and ^{3}He films [8], $T_{\rm p}$ approaches 0 K and the vanishing point is a critical coverage, $n_{\rm c} \simeq 20$ μmol/m^2. So the elastic anomaly of helium films is linked to the gapped solid phase of the one side of quantum phase transition, which is indeed a superfluid–insulator quantum phase transition for the ^{4}He case (a fluid–insulator quantum phase transition for the ^{3}He case). On the other hand, $T_{\rm p}$ of neon does not decrease below 5 K. This indicates that neon film on porous glass is close to a classical system, which does not show quantum phase transition and does not become superfluid. The elastic anomaly is therefore not limited to the accompanying phenomenon of quantum phase transition, but is rather originated generally from the energy structure of adsorbed films.

As the elastic anomaly is not sharp but gradual, the crossover from the stiff to the soft state does not indicate first order phase transition or Kosterlitz-Thouless type melting, contrary to bulk and monolayer neon on graphite [41, 86]. One may naturally expect that neon atoms on disordered and porous substrate form an amorphous film. The amorphous state is consistent with the fact that layer-by-layer

growth of neon film was not observed on disordered substrates [55], while neon films on graphite show clear layer-by-layer growth and sharp signatures in heat capacity [41].

Finally, we point out that T dependences of frequency and dissipation data (shown in Fig. 4.5) bear a strong resemblance to elastic behavior seen in glass transitions, e.g., Fig. 3.39, p. 110 in Ref. [119]. In glass transitions of polymers and amorphous materials, the elasticity or the velocity of sound gradually increases accompanying a peak in dissipation or attenuation as system passes dynamic glass transition temperature $T_{\rm g}^{\rm dyn}$. Our dissipation peak temperature $T_{\rm p}$ may correspond to $T_{\rm g}^{\rm dyn}$ or may be related to it. In order to clarify the aspects of glass transition in the elastic anomaly of neon films, experiments focused on glassy properties. We can consider that the disordered potential on porous glasses make a glassy adsorbed films without rapid cooling.

Chapter 5

Hydrogen Films

Molecular hydrogen has quantum properties due to its small mass, and their films are possible candidate that exhibit quantum phase transitions. I observed in H_2, HD, D_2 films that all exhibit the elastic anomaly in a temperature range 1–10 K. A remarkable feature in hydrogen films is that they show multiple elastic anomalies. They may originate from the quantum properties and the surface diffusion.

5.1 Experimental results

5.1.1 Raw data

The raw data of H_2 film with a small coverage is shown in Fig. 5.1. We clearly see the elastic anomaly, which is qualitatively similar to those of helium and neon films. The dissipation peak temperature is roughly equals to that of neon film at the same coverage, in Fig. 4.1. The data points at about 1 K are doubly measured because we obtained the data from about 0.1–1.3 K, collected the ^{3}He–^{4}He mixture for several hours, then measured the data from 1.0–22.0 K. The origin of the small discrepancy in the doubly measured data at about 1 K is not known.

5.1.2 Multiple elastic anomalies

As in the analysis of the neon data, the background was subtracted using the following formulae:

$$\delta f(T) = f(T) - f_{\mathrm{B}}(T), \tag{5.1}$$

and

$$\delta Q^{-1}(T) = Q^{-1}(T) - Q_{\mathrm{B}}^{-1}(T). \tag{5.2}$$

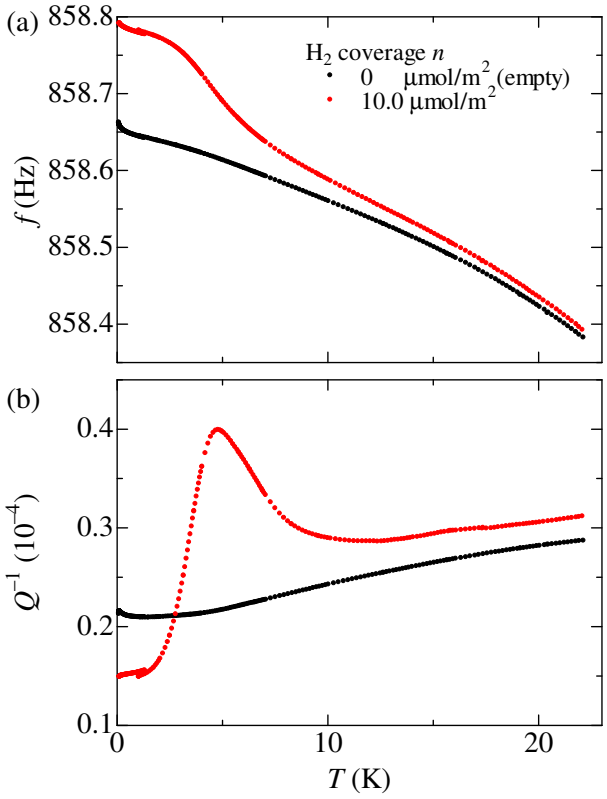

Figure 5.1: Raw data of (a) resonant frequency f and (b) energy dissipation Q^{-1} at the H_2 coverage $n = 0$ (the background) and 10.0 μmol/m^2.

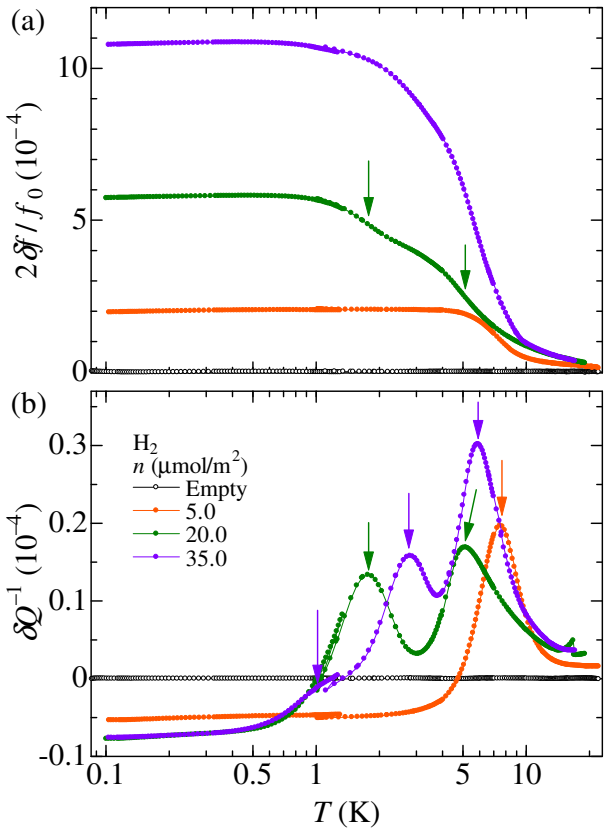

Figure 5.2: (a) Resonant frequency shift and (b) excess dissipation at three H_2 coverages with different numbers of the dissipation peak. The arrows in (b) indicate the peaks, and the arrows in (a) indicate inflection points.

Typical data with three coverages are shown in Fig. 5.2. To our surprise, the number of the dissipation peaks increases with increasing n. We can distinguish three peaks at $n = 35.0$ μmol/m^2. The position of the peak at the highest temperature does not decrease below 5 K by changing n. This feature is similar to the observations in neon films. The peaks at lower temperatures are in a range 1–3 K. The magnitude of the peak at the lowest temperature at $n = 35.0$ μmol/m^2 is small compared with other peaks. The dissipation peaks up to three were observed in H_2, HD, and D_2 films.

All data of H_2, HD, and D_2 are shown in Figs. 5.3, 5.4, and 5.5, respectively. Some data are overlapped, but we see gradual changes in δf and δQ^{-1} by increasing the coverage. For all data (note that δf in HD data are arbitrary shifted, see

below), $\delta f(T_{\min})$ increases by increasing n up to the full-pore coverage $n_{\rm fp}$, whereas $\delta f(T_{\max})$ does not change so much. The number and positions of the dissipation peaks gradually changes by increasing n. The data in H_2, HD, and D_2 are similar except that there exists a broad dissipation peak below 2 K only in the HD data.

I mention that the HD data in Fig. 5.4 should be treated carefully. The resonant frequency data of HD have occasional constant offsets for many coverages, probably due to abrupt frequency jumps from external vibrations or the film preparation. We shifted the $2\delta f/f_0$ data in Fig. 5.4 to set roughly $2\delta f/f_0 = 0$ at about 20 K. Only for the HD data, we observed a broad excess dissipation below 2 K. A broad excess dissipation was observed once in the background (open circles in Fig. 5.4), but it disappeared in the second background measurement (closed circles). We have observed once an excess dissipation peak without adsorbed film above 20 K, and it disappeared in the second warming and did not reappear in the following warmings. Therefore, we used the second data (closed circles) as the background of the HD experiment. However, every δQ^{-1} of finite HD coverage shows again a broad excess dissipation. The position of the broad excess dissipation with finite coverage are not the same as that of the open-circled background. The heights and widths are similar, but not identical. Contrary to the elastic anomaly, $2\delta f/f_0$ slightly *decreases* at the broad excess dissipation peaks. The peak position, height, width of the broad excess dissipation seems to have no systematic dependence on the coverage. We have no explanation for this occasional anomaly of a broad excess dissipation, and do not reject a possibility that the broad dissipation at finite coverages originates from a property in HD films, such as quadrupole moment [11] or in the HD–substrate composite system. We define the anomaly temperature $T_{\rm a}$ at which δf starts to decreases toward lower temperatures. The coverage dependence of $T_{\rm a}$ will be shown later.

When n is larger than $n_{\rm fp}$, the full-pore coverage, δf and δQ^{-1} suddenly increases for higher temperatures, and go outside the displayed range. At this stage, the dissipation is so large that the loop circuit at the resonant frequency is unlocked and the measurement becomes unstable. This feature is probably due to the melting of the full-pore solid hydrogen inside the porous Gelsil glass. The temperature of the melting is smaller than the bulk triple point temperature for H_2 and HD because of supercooling effect of nanometer-scale confinement [120]. The melting temperature of full-pore D_2, 19 K, is nearly equals but slightly higher than the bulk triple point temperature, 18.7 K.

Let us go back to comparing differences among H_2, HD, and D_2 films. Here we number the peaks in descending order of the temperature, i.e., $T_{\rm p1} > T_{\rm p2} > T_{\rm p3}$ for convenience. At $T_{\rm p1}$, $T_{\rm p2}$, and $T_{\rm p3}$, δf increases rapidly toward lower temperatures, therefore each of them is the temperature of the elastic anomaly similar to those of the helium and neon films. The height of the dissipation peak at $T_{\rm p1}$ grows the most,

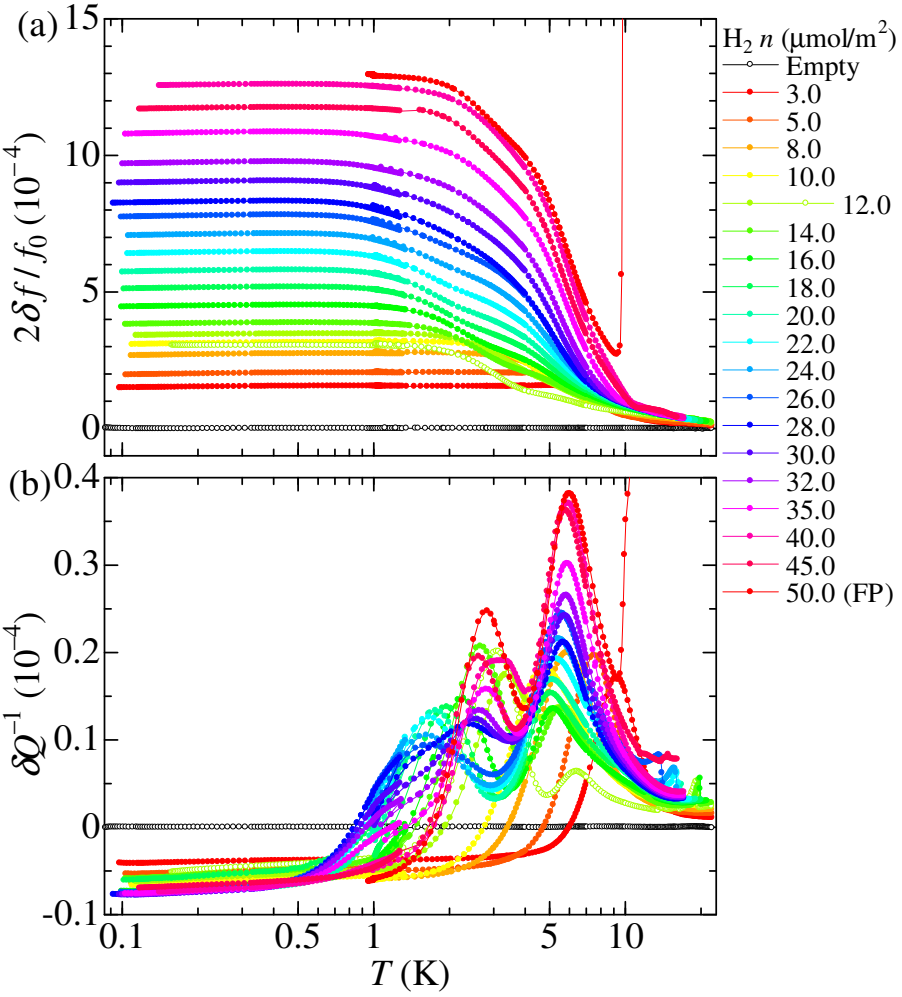

Figure 5.3: (a) Resonant frequency shift and (b) excess dissipation of all H_2 coverages. FP denotes the full-pore coverage.

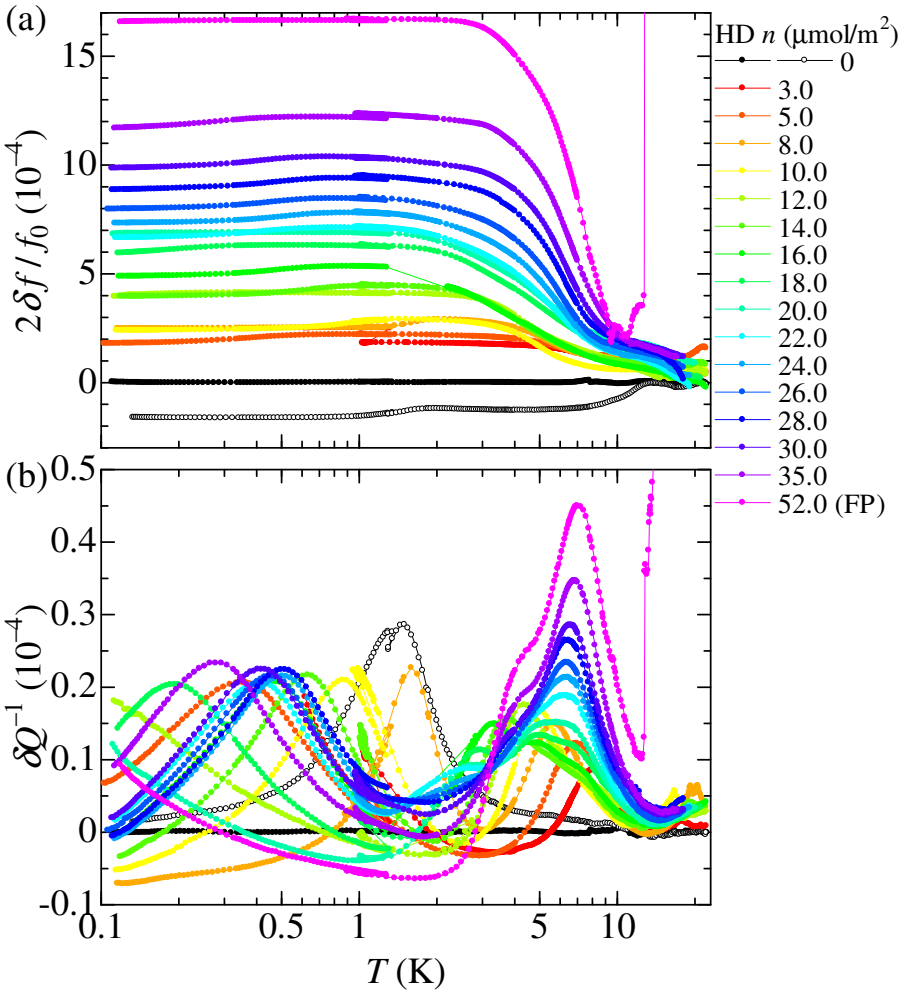

Figure 5.4: (a) Resonant frequency shift and (b) excess dissipation of all HD coverages. FP denotes the full-pore coverage. The frequency data are arbitrary vertically shifted.

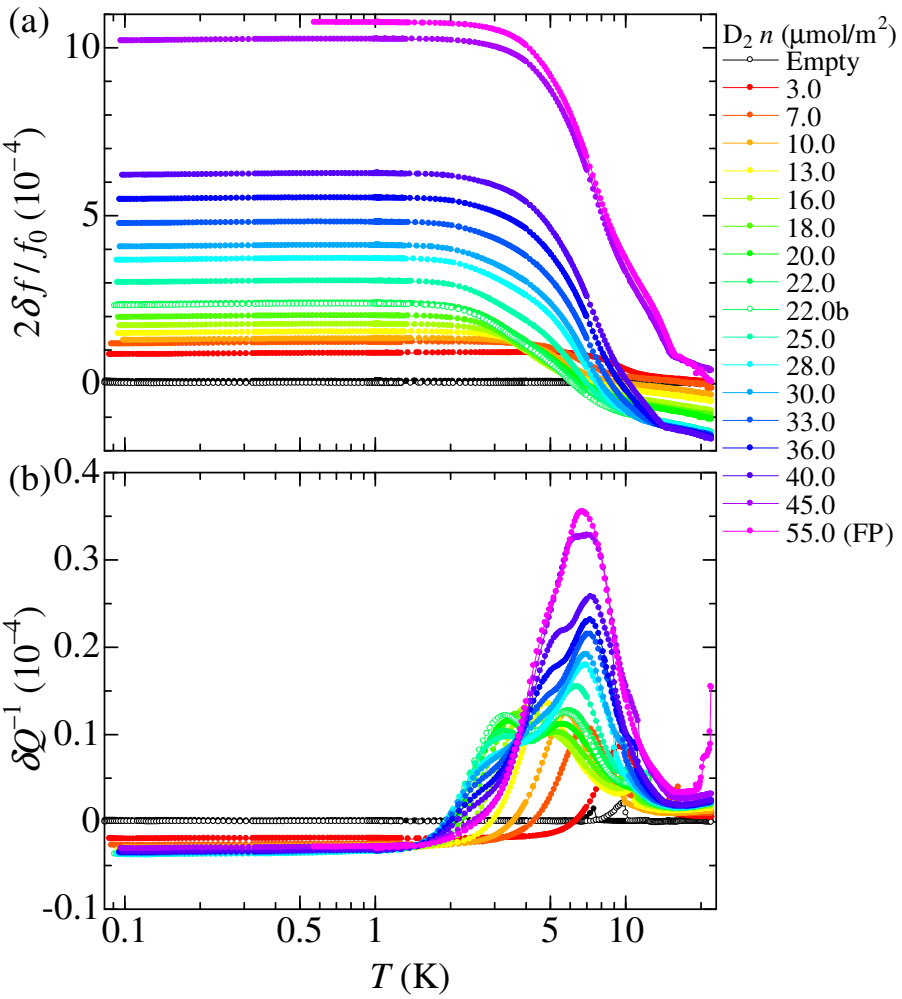

Figure 5.5: (a) Resonant frequency shift and (b) excess dissipation of all D_2 coverages. FP denotes the full-pore coverage.

whereas the one at T_{p3} grows less and disappears before the full-pore coverage n_{fp}.

We find that the lowest temperature peak T_{p3} of H_2 at 1–2 K at higher coverages are more prominent than T_{p3}'s of HD and D_2. In D_2 films, T_{p3}'s are in a higher temperature range, about 2–3 K. In HD films, T_{p3} is barely distinguishable because of the broad dissipation peak at T_a. As we see in the next section, the dissipation peak at T_{p3} in HD films is the smallest.

5.2 Analysis

5.2.1 Coverage dependence of multiple dissipation peaks

The dissipation peak temperature is an important quantity from which we described the quantum critical behavior of helium films and the crossover between the stiff and soft state in classical neon films in the previous Chapters. The multiple peaks, T_{p1}, T_{p2}, and T_{p3}, suggest that hydrogen films have several diffusion mechanisms which are combined to the elasticity. As shown in the Cole–Cole plot in Fig. 5.6, the data draw a deformed semicircle, which suggests that a distribution function for energy gap is needed to fit the data with the anelastic response function. Because of the multiple peaks, it is difficult to fit the data to the anelastic response functions used in the helium and neon films analyses.

To extract the coverage dependence of T_p's, we made trial fittings to get the value of T_p. We use a trial fitting function,

$$\delta Q^{-1} = \sum_i h_i \left[\frac{2(T_{pi}/T)}{1 + (T_{pi}/T)^2} \right]^{a_i}, \tag{5.3}$$

where the index i takes 1, (1 and 2), or (1, 2, and 3) depending on n, T_p is a dissipation peak temperature, h is a height of the peak, and a is an exponent which determines the width of the dissipation. This function has no physical meaning, but enables us to examine the peak positions without complicated conjectures. We fitted this function to the data with three peaks, and with two peaks close to each other. Several trials are shown in Figs. 5.7, 5.8, and 5.9. The exponent was typically $a \sim$ 10–30. For the H_2 data in Fig. 5.7, the lowest-temperature peak is clearly visible at $T_{p3} = 1.25$ K. For the HD and D_2 data in Figs. 5.8 and 5.9, peaks at T_{p1} and T_{p3} are fitted, and we get T_{p2} from the red closed circles.

The coverage dependences of the dissipation peak temperatures are shown in Fig. 5.10. The curve of T_p splits at 10–16 K and at 26–28 K for every hydrogen films. The multiple elastic anomalies are the common feature in bosonic H_2 and D_2 and fermionic HD films.

The T_{p1} curve which terminates to decrease above 5 K is quantitatively similar to that of neon films in Fig. 4.6. It remains until the full-pore coverage, therefore

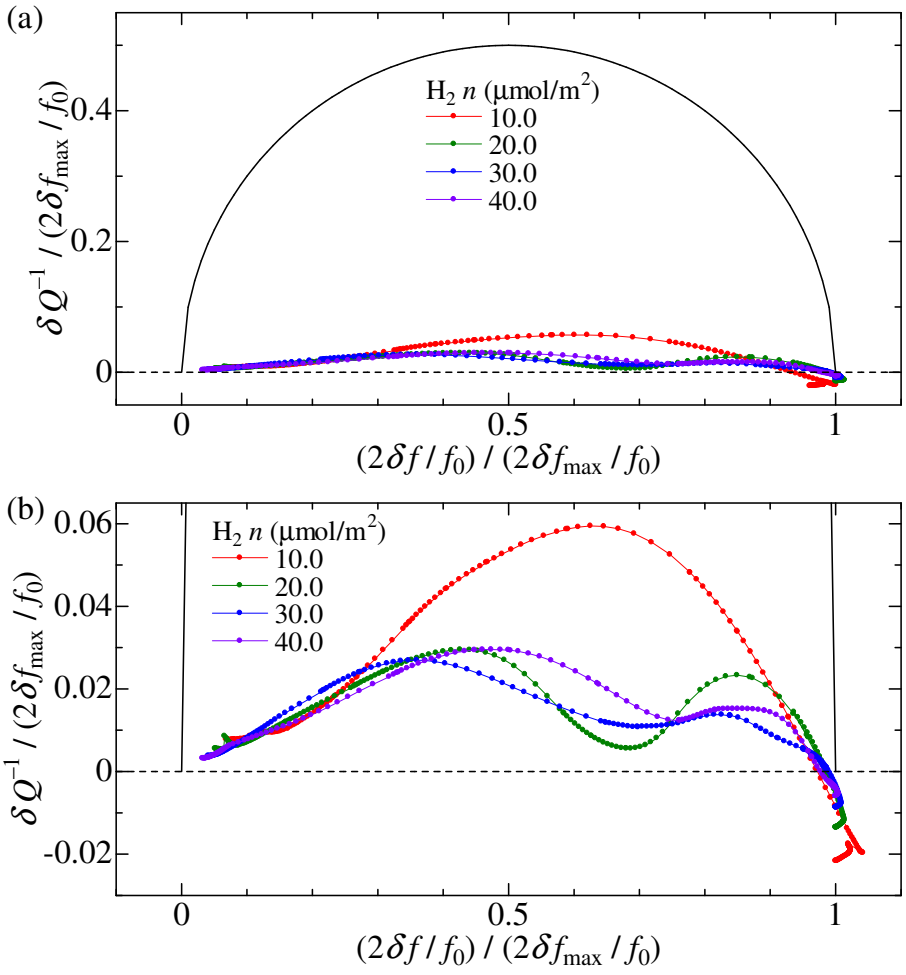

Figure 5.6: Cole–Cole plot of H_2 film data. (a) At equal intervals of the axes, and (b) expanded view.

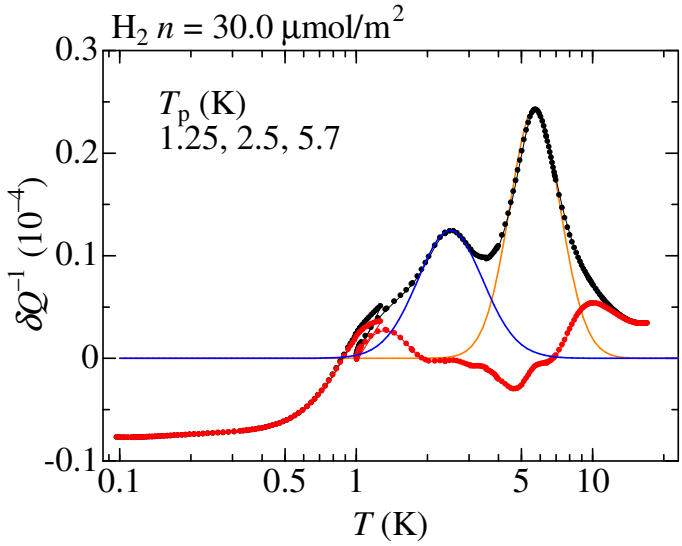

Figure 5.7: Trial fitting to the dissipation peaks at a H_2 coverage 30.0 μmol/m^2. Black closed circles are the original data, and red closed circles are data from which trial functions of the two solid curves are subtracted.

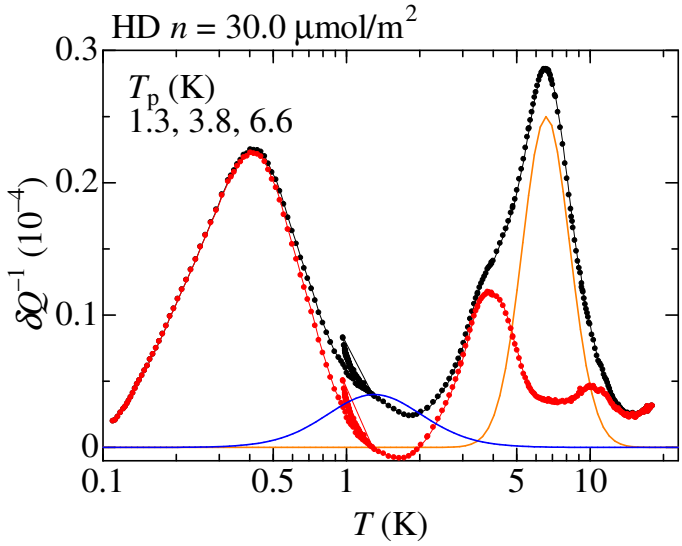

Figure 5.8: Trial fitting to the dissipation peaks at a HD coverage 30.0 μmol/m^2. Black closed circles are the original data, and red closed circles are data from which trial functions of the two solid curves are subtracted.

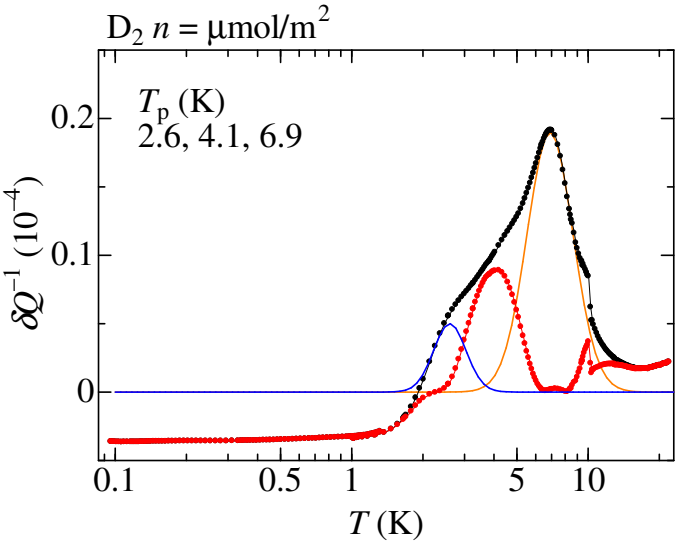

Figure 5.9: Trial fitting to the dissipation peaks at a D_2 coverage 30.0 μmol/m^2. Black closed circles are the original data, and red closed circles are data from which trial functions of the two solid curves are subtracted.

it is also an intrinsic property in solid hydrogen in a porous glass. The same is true for the T_{p2} curve. On the other hand, the T_{p3} curve disappears at a coverage, 26–40 μmol/m^2. At each splitting point of T_{p1}-T_{p2} and T_{p2}-T_{p3}, T_p at higher temperature suddenly rises, and then continue to increase moderately by increasing n up to n_{fp}. The T_{p3} curve from the lowest coverage to the disappearing point show a concave curvature like T_p curve of helium films shown in Fig. 3.10. However, the T_{p3} curve of hydrogen films stop to decrease at above 1 K, and show a plateau or a return to higher temperatures. This suggests that hydrogen films, even H_2 films which have the largest quantum number Λ among stable hydrogen isotopes, do not show quantum phase transition.

The anomaly temperature T_a of HD oscillates with increasing the coverage, as shown in Fig. 5.10. The oscillation period is about 7 μmol/m^2, which corresponds to 0.5 layers (n_1 = 15.16 μmol/m^2), until 20 μmol/m^2. As T_a does not change randomly against the coverage, the anomaly possibly comes from some effect in HD film or HD–substrate composite system.

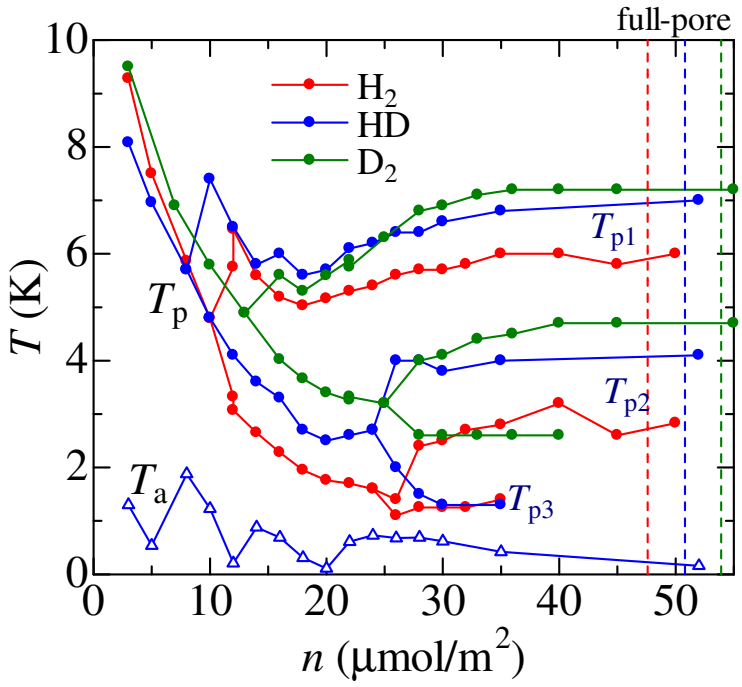

Figure 5.10: Coverage dependences of the dissipation temperature T_p associated with the elastic anomaly and the anomaly temperature T_a of the broad excess dissipation for HD.

5.2.2 Coverage dependence of elastic constant

As discussed in the neon result in Sect. 4.1.4, the normalized resonant frequency shift $2\delta f/f_0$ gives the elastic constant of hydrogen adsorbed on the porous Gelsil glass. In this analysis, we do not use the data of HD because they contain not only occasional offsets in $2\delta f/f_0$ of each coverage as large as 5×10^{-4} but also the anomaly of the broad excess dissipation which decreases $2\delta f/f_0$ at low temperatures.

We take into account the offsets in the data of D_2, which appears at the highest temperature (22 K) as shown in Fig. 5.11 (a). The normalized resonant frequency shift $2\delta f(T_{\max})/f_0$ at $T_{\max} = 22.0$ K decreases as n increases at first, then goes back to zero near the full-pore coverage, $n_{\rm fp} = 53.9$ μmol/m^2. The origin of this background offset cannot be explained by a mass loading, whose effect is comparatively small as shown in dashed line in Fig. 5.11 (a). We consider the difference $[2\delta f(T_{\min})/f_0 - 2\delta f(T_{\max})/f_0]$ as the elasticity $2\delta f(T_{\min})/f_0$ at $T_{\min} \simeq 0.09$ K in Fig. 5.11 (b) for D_2.

The coverage dependence of $2\delta f(T_{\min})/f_0$ is shown in 5.11. Both $2\delta f(T_{\min})/f_0$ increases monotonically by increasing n until $n_{\rm fp}$. We fit the data with a linear function $y = a(n - n_{\rm offset})$ in a range $0 < n < n_{\rm fp}$. The results gives $a = (0.28 \pm 0.01) \times 10^{-4}$ (μmol/m^2)$^{-1}$ and $n_{\rm offset} = (-1 \pm 1)$ μmol/m^2 for H_2, and $a = (0.21 \pm 0.01) \times 10^{-4}$ (μmol/m^2)$^{-1}$ and $n_{\rm offset} = (3 \pm 1)$ μmol/m^2 for D_2, respectively. The offset coverages are zero within the error or positive, similar to neon films. The slopes give the effective shear modulus as follows.

At the full pore coverages, $n_{\rm fp} = 47.6$ and 53.9 μmol/m^2 for H_2 and D_2, the normalized resonant frequency shifts are calculated from the linear fittings to be $2\delta f(T_{\min}, n_{\rm fp})/f_0 = 13.6 \times 10^{-4}$ and 10.7×10^{-4}, respectively. Therefore, the effective shear modulus $\delta G_{\rm g}$ is 50.9 and 40.1 MPa for H_2 and D_2, respectively, using $\delta G_{\rm g} = (G_{\rm g}/0.197)(2\delta f(T_{\min}, n_{\rm fp})/f_0)$. The bulk shear modulus of solid hydrogen is 100 and 160 MPa for H_2 and D_2 from Fig. 52 in Ref. [13]. If we take the effect of the porous structure [118] of full-pore hydrogen into account by multiplying the bulk shear modulus by $(1 - p)^2 = 0.21$, the effective shear modulus becomes 21 and 36 MPa for H_2 and D_2, respectively. Thus, the effective shear modulus $\delta G_{\rm g}$ of D_2 from our experiment is comparable to the estimated value from the bulk shear modulus, and $\delta G_{\rm g}$ of H_2 from the experiment is somehow larger than the estimated value.

5.3 Discussion

The prominent feature of hydrogen films is the emergence of the multiple elastic anomalies. We show a phase diagram of H_2 film in Fig. 5.12. The $T_{\rm p1}$ curve

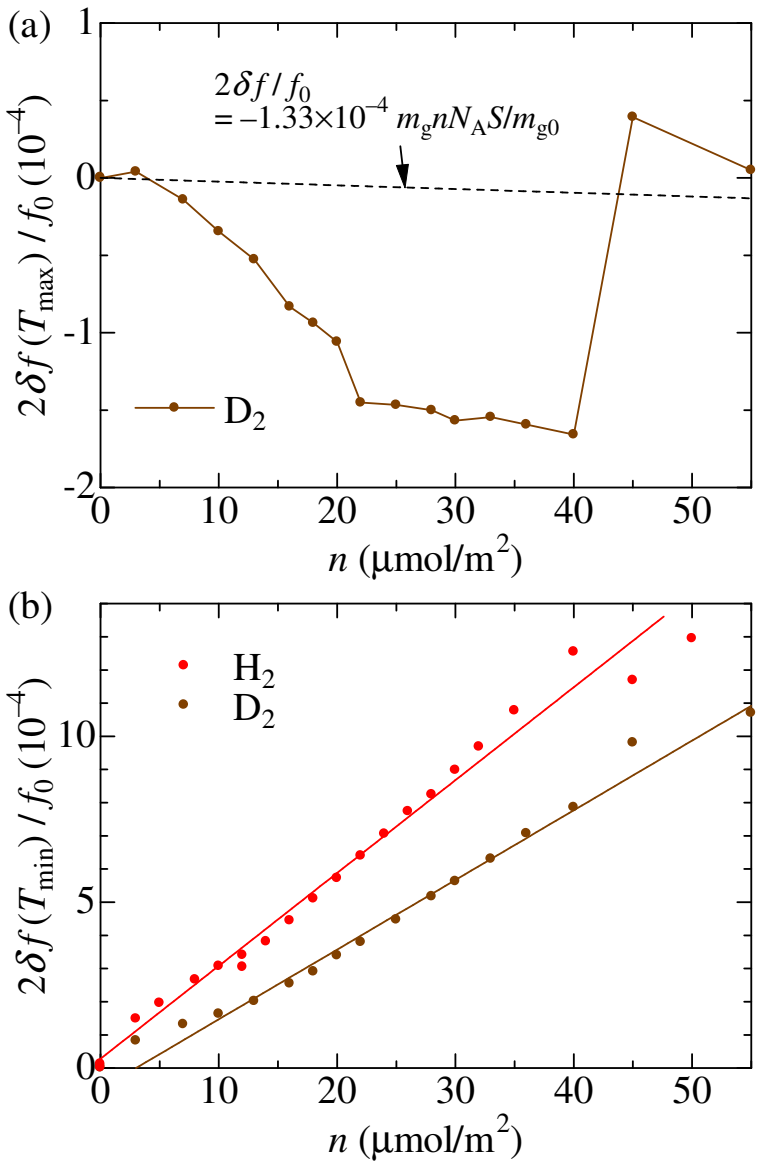

Figure 5.11: (a) Normalized frequency shift of D_2 at T_{max} = 22.0 K as a function of the coverage. The dashed line shows the mass loading effect. (b) Normalized resonant frequency of H_2 and D_2 at $T_{min} \simeq 0.09$ K as a function of the coverage. The lines are linear fittings.

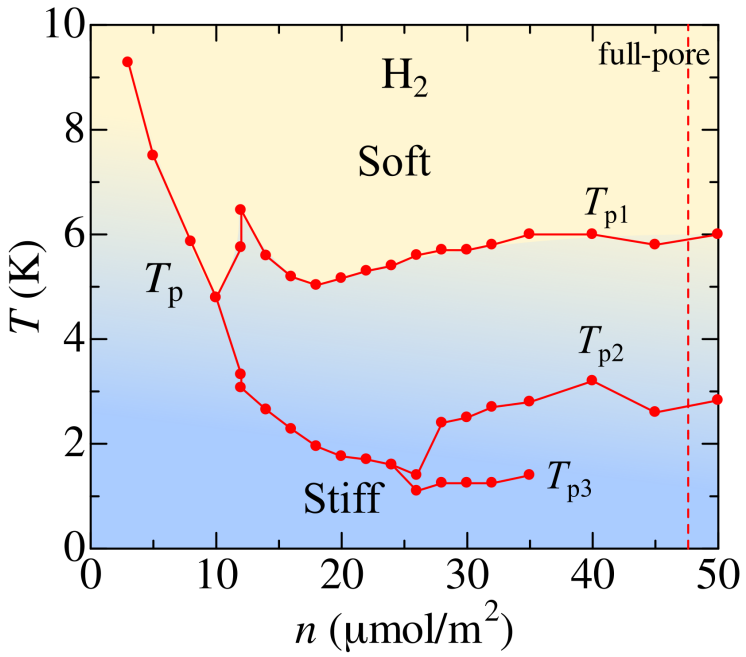

Figure 5.12: Phase diagram of H_2 film.

which persists above 5 K until $n = n_{fp}$ is quantitatively the same as that of neon film (Fig. 4.6), as mentioned above. As neon films behave as a classical system, the T_{p1} curve above 5 K is a crossover temperature between a fluidlike soft state and a solidlike stiff state. At 3 K, every H_2 films in Fig. 5.3 already have 65–100% of the elasticity $(2\delta f/f_0)$ at T_{min}, which suggests that most of H_2 molecules freeze at a temperature below the T_{p1} curve. Therefore, the T_{p1} curve represents the main crossover temperature between a fluidlike soft state and a solidlike stiff state of H_2 films.

The T_{p2} curve which appears at 26 μmol/m^2 also persists until $n = n_{fp}$. The two peak temperatures, T_{p1} and T_{p2}, at $n = n_{fp}$ are 6.0 and 2.8 K, respectively. The dissipation peaks at these T_p's are definitely comes from the solid H_2 confined in the porous glass. In hcp solid H_2 at zero pressure, there are two self-diffusion mechanisms by molecule-vacancy exchange [13, 121, 122]. For any crystals at $T > 0$, vacancies are present in thermal equilibrium. A vacancy changes its position with one of the nearest molecule either by overcoming the potential barrier (classical) or by quantum tunneling. The activation energy in solid H_2 for the classical diffusion is $E_v + E_b = 197$ K, and that for the quantum tunneling is $E_v = 112$ K, where E_v is the vacancy formation energy and E_b is the potential

barrier. The ratio of the two activation energies, 1.8, is in agreement with the ratio of T_{p1} to T_{p2} at $n = n_{fp}$, 2.1. If $T_p = 6.0$ K corresponds to $E/k_B = 197$ K, we obtain $E = 33k_BT_p$, comparable to the neon result. Thus we consider that T_{p1} and T_{p2} are attributed to the classical and quantum diffusion mechanisms in solid hydrogen.

The T_{p3} curve at the lowest temperature does not decreases below 1 K. It has a minimum or a plateau around $n = 30$ μmol/m^2 for every hydrogen isotopes. This coverage corresponds to about 2.1 layers, which is close to n_c of the helium films at 1.8 layers and the coverage of the features in δf, δQ^{-1} and T_p of the neon film at 1.6 layers. It is remarkable that every film examined, ^{4}He, ^{3}He, Ne, H_2, HD, D_2 show some features at about 2 layers.

As the T_{p3} curve vanishes as n approaches n_{fp}, we attribute T_{p3} to the diffusion in the surface of the hydrogen film. It is recognized that the surface of thin hydrogen film is a mobile layer even at low temperatures. A quasi-elastic neutron scattering study showed that 1–5 layers of HD film on MgO has a 0.3 mobile layers above 8 K [123]. The diffusion constant of mobile HD film obeys the Arrhenius relation with an activation energy of $E_s = (16.1 \pm 0.5)$ K. A hole-burning experiment showed that three and more layers of H_2 and D_2 films has diffusivity at down to 1.5 K [124]. The activation energies they posed are $E_s = (19 \pm 1.5)$ and (38 ± 4) K, respectively. The surface diffusion or fluidity at such low temperatures is because the motion of molecules at the uppermost layer does not require the vacancy-formation energy [124]. Our T_{p3} suggests the surface fluid state of H_2, HD and D_2 films at down to 1 K, very low temperature compared to the triple point temperatures (13.8, 16.6, and 18.7 K). The ratios E_s/T_{p3} are 17, 12, and 15, respectively. These results are reasonable compared with the result in the helium films, $\Delta/k_BT_p = 13$.

The non-vanishing T_{p3} of hydrogen films on porous Gelsil glass suggests that our hydrogen films does not undergo a quantum phase transition. However, it should be mentioned that T_{p3}'s of H_2 and HD decrease until 1 K, far below $T_p \sim 5$ K of less quantum neon films. Future improvements, such as using substrates with shallow potential depth or with weak disorder, may produce a quantum phase transition of hydrogen films.

Chapter 6

Conclusions

I have demonstrated that the direct elasticity measurement of adsorbed films at low temperatures is a powerful tool to investigate their elasticity and stiff-soft crossover phenomena. The elastic anomaly, an increase of the elastic constant at low temperatures with excess dissipation, was discovered in every film examined in this study. This fact suggests that the elastic anomaly is a universal phenomenon in molecular films adsorbed on a substrate.

Helium films on porous glass exhibit the elastic anomaly at the quantum phase transitions. The localized ^{4}He and ^{3}He films show an identical elastic anomaly, regardless of their bosonic and fermionic quantum statistics. The elastic anomaly is explained by the thermal activation of helium atoms from the localized to extended states with a distributed energy gap. The dissipation peak temperature and the energy gap decreases as the film coverage approaches the critical coverage, n_c. The two-dimensional compressibility shows divergent behavior near n_c, which is deduced from the power law behavior of the gap and the energy band. The divergent behavior of the compressibility was confirmed from the direct calculation of the observed frequencies. Both the localized ^{4}He and ^{3}He are gapped and compressible, suggesting that the ground state is a sort of Mott insulator or Mott glass. Future studies in the vicinity of n_c at lower temperatures will unveil the nature of the quantum phase transition of the helium films.

I have also found that neon films on porous glass exhibit the elastic anomaly. The elastic anomaly is qualitatively identical to that of helium films. The elasticity at the lowest temperature and the height of dissipation peak are proportional to the coverage until certain coverages, and both of them show kinks at the same coverage 30 μmol/m^2. The data are fitted by the thermal activation model that successfully explains the elastic anomaly of helium films. In contrast to helium films, the dissipation peak temperature becomes kept to be about 5 K, suggesting that neon

films behave as a classical system without quantum phase transition by changing the coverage. The crossover from the stiff to the soft state bear a resemblance to dynamic glass transition.

Hydrogen films show from one to three elastic anomalies. The number of elastic anomalies changes by changing the coverage. The coverage-dependence of the branched T_p-curve is similar among H_2, HD, and D_2. Each T_p indicates different diffusion mechanism in solid hydrogen. The origin of two T_p's at high T are attributed to the classical thermal diffusion and the diffusion by quantum tunneling in solid hydrogen. The T_p at low T suggests that the surface of the hydrogen films is a mobile layer even near 1 K, very low temperature compared to the bulk triple point temperature. We observed that T_p's of hydrogen films do not vanish toward 0 K, which means that hydrogen films do not undergo quantum phase transition.

Reference

[1] S. J. Gregg and K. S. W. Sing, *Adsorption, Surface Area and Porosity* (Academic Press, London, 1982), 2nd ed.

[2] J. Tao and A. M. Rappe, Physical Review Letters **112**, 106101 (2014).

[3] D. P. Broom, *Hydrogen Storage Materials* (Springer-Verlag, London, 2011).

[4] C. Chen and J. Hone, Proceedings of the IEEE **101**, 1766 (2013).

[5] J. D. Reppy, J. Low Temp. Phys. **87**, 205 (1992).

[6] M. A. Fisher, P. B. Weichman, G. Grinstein, and D. S. Fiher, Physical Review B **40**, 546 (1989).

[7] P. A. Crowell, F. W. V. Keuls, and J. D. Reppy, Physical Review B **55**, 12620 (1997).

[8] T. Makiuchi, M. Tagai, Y. Nago, D. Takahashi, and K. Shirahama, Physical Review B **98**, 235104 (2018).

[9] T. Makiuchi, K. Yamashita, M. Tagai, Y. Nago, and K. Shirahama, Journal of the Physical Society of Japan, in press (2019).

[10] C. Enss and S. Hunklinger, *Low-Temperature Physics* (Spriger-Verlag, Berlin, Heidelberg, 2005).

[11] J. Van Kranendonk, *Solid Hydrogen: Theory of the Properties of Solid H_2, HD and D_2* (Springer, New York, 1983).

[12] L. W. Bruch, M. W. Cole, and E. Zaremba, *Physical Adsorption: Forces and Phenomena* (Dover, New York, 2007).

[13] I. F. Silvera, Reviews of Modern Physics **52**, 393 (1980).

[14] J. N. Israelachvili, *Intermolecular and Surface Forces* (Academic Press, Burlington, MA, 2011), 3rd ed.

[15] L. H. Nosanow, Journal of Low Temperature Physics **26**, 613 (1977).

[16] J. de Boer, Physica **14**, 139 (1948).

[17] F. London, Nature **141**, 643 (1938).

[18] F. Pobell, *Matter and Methods at Low Temperatures, Third Edition* (Springer, Berlin, 2007).

[19] S. Kobayashi and Y. Otsuka, *Low temperature technique (Teion-gijutsu)*, [in Japanese] (University of Tokyo Press, Tokyo, 1987).

[20] PLTS-2000: "The provisional low temperature scale from 0.9mK to 1K", Comité International des Poids et Mesures (CIPM) (2000), Appendix to recommendation C1.

[21] D. S. Greywall, Physical Review B **33**, 7520 (1986).

[22] V. D. Arp, R. D. McCarty, and D. G. Friend, Technical Note 1334, National Institute of Standards and Technology (U.S.) (1998).

[23] H. M. Roder, G. E. Childs, R. D. McCarty, and P. E. Angerhofer, Technical Note 641, National Bureau of Standards (U.S.) (1973).

[24] V. A. Rabinovich, A. A. Vasserman, V. I. Nedostup, and L. S. Veksler, *Thermophysical properties of neon, argon, krypton and xenon* (Hemisphere, New York, 1988).

[25] M. W. Cole and T. T. Tsong, Surface Science **69**, 325 (1977).

[26] G. Vidali, G. Ihm, H.-Y. Kim, and M. W. Cole, Surface Science Reports **12**, 133 (1991).

[27] E. Cheng, M. W. Cole, J. Dupont-Roc, W. F. Saam, and J. Treiner, Reviews of Modern Physics **65**, 557 (1993).

[28] J. Treiner, Journal of Low Temperature Physics **92**, 1 (1993).

[29] M. Boninsegni, Journal of Low Temperature Physics **159**, 441 (2010).

[30] L. Pricaupenko and J. Treiner, Physical Review B **74**, 430 (1995).

[31] H. Godfrin and H.-J. Lauter, in *Progress in Low Temperature Physics*, edited by W. P. Halperin (Elsevier, Amsterdam, 1995), vol. XIV, chap. 4.

[32] H. Fukuyama, Journal of the Physical Society of Japan **77**, 111013 (2008).

[33] Y. Niimi, S. Murakawa, Y. Matsumoto, H. Kambara, and H. Fukuyama, Review of Scientific Instruments **74**, 4448 (2003).

[34] P. A. Crowell and J. D. Reppy, Physical Review B **53**, 2701 (1996).

[35] J. Nyéki, A. Phillis, A. Ho, D. Lee, P. Coleman, J. Parpia, B. Cowan, and J. Saunders, Nature Physics **13**, 455 (2017).

[36] D. S. Greywall, Physical Review B **41**, 1842 (1990).

[37] D. S. Greywall, Physical Review B **47**, 309 (1993).

[38] S. Nakamura, K. Matsui, T. Matsui, and H. Fukuyama, Physical Review B **94**, 180501(R) (2016).

[39] G. Zimmerli, G. Mistura, and M. H. W. Chan, Physical Review Letters **68**, 60 (1992).

[40] O. E. Vilches, Y.-M. Liu, P. S. Ebey, and F.-C. Liu, Physica B **194–196**, 665 (1994).

[41] R. E. Rapp, E. P. de Souza, and E. Lerner, Physical Review B **24**, 2196 (1981).

[42] M. H. W. Chan, A. D. Migone, K. D. Miner, and Z. R. Li, Physical Review B **30**, 2681 (1984).

[43] A. Casey, H. Patel, J. Nyéki, B. P. Cowan, and J. Saunders, Physical Review Letters **90**, 115301 (2003).

[44] M. Neumann, J. Nyéki, B. Cowan, and J. Saunders, Science **317**, 1356 (2007).

[45] J.-P. Coulomb, T. S. Sullivan, and O. E. Vilches, Physical Review B **30**, 4753 (1984).

[46] T. S. Sullivan, A. D. Migone, and O. E. Vilches, Surface Science **162**, 461 (1985).

[47] J. Ma, L. Kingsbury, F. L. Liu, and O. E. Vilches, Physical Review Letters **61**, 2348 (1988).

[48] P. Levitz, G. Ehret, S. K. Sinha, and J. M. Drake, The Journal of Chemical Physics **95**, 6151 (1991).

[49] K. Yamamoto, H. Nakashima, Y. Shibayama, and K. Shirahama, Physical Review Letters **93**, 075302 (2004).

[50] K. Yamamoto, Y. Shibayama, and K. Shirahama, Physical Review Letters **100**, 195301 (2008).

[51] K. Yamamoto, Ph.D. thesis, Keio University, Yokohama (2008), [in Japanese].

[52] D. F. Brewer and D. C. Champeney, Proceedings of the Physical Society **79**, 855 (1962).

[53] D. F. Brewer, A. J. Symonds, and A. L. Thomson, Physics Letters **13**, 13 (1964).

[54] T. E. Huber and C. A. Huber, Journal of Low Temperature Physics **80**, 315 (1990).

[55] T. E. Huber, D. Scardino, and H. L. Tsou, Physical Review B **52**, 11372 (1995).

[56] J. M. Kosterlitz and D. J. Thouless, Journal of Physics C: Solid State Physics **6**, 1181 (1973).

[57] D. J. Bishop and J. D. Reppy, Physical Review Letters **40**, 1727 (1978).

[58] D. J. Bishop and J. D. Reppy, Physical Review B **22**, 5171 (1980).

[59] G. Agnolet, D. F. McQueeney, and J. D. Reppy, Physical Review B **39**, 8934 (1989).

[60] D. McQueeney, G. Agnolet, and J. D. Reppy, Physical Review Letters **52**, 1325 (1984).

[61] D. Tulimieri, N. Mulders, and M. H. W. Chan, Journal of Low Temperature Physics **110**, 609 (1998).

[62] G. A. Csáthy and M. H. W. Chan, Physical Review Letters **87**, 045301 (2001).

[63] G. A. Csáthy, J. D. Reppy, and M. H. W. Chan, Physical Review Letters **91**, 235301 (2003).

[64] M. Hieda, K. Matsuda, T. Kato, T. Matsushita, and N. Wada, Journal of the Physical Society of Japan **78**, 033604 (2009).

[65] N. Wada, T. Matsushita, M. Hieda, and R. Toda, Journal of Low Temperature Physics **157**, 324 (2009).

[66] M. Hieda, Ph.D. thesis, The University of Electro-Communications, Tokyo (2001), [in Japanese].

[67] K. Atkins, *Liquid Helium* (Cambridge University Press, Cambridge, 1959).

[68] I. Rudnick and J. C. Fraser, Journal of Low Temperature Physics **3**, 225 (1970).

[69] D. R. Nelson and J. M. Kosterlitz, Physical Review Letters **39**, 1201 (1977).

[70] V. Ambegaokar, B. I. Halperin, D. R. Nelson, and E. D. Siggia, Physical Review B **21**, 1806 (1980).

[71] J. E. Berthold, D. J. Bishop, and J. D. Reppy, Physical Review Letters **39**, 348 (1977).

[72] D. J. Bishop, J. E. Berthold, J. M. Parpia, and J. D. Reppy, Physical Review B **24**, 5047 (1981).

[73] K. Shirahama, M. Kubota, S. Ogawa, N. Wada, and T. Watanabe, Physical Review Letters **64**, 1541 (1990).

[74] G. A. Csáthy, D. Tulimieri, J. Yoon, and M. H. W. Chan, Physical Review Letters **80**, 4482 (1998).

[75] G. A. Csáthy, Ph.D. thesis, The Pennsylvania State University (2001).

[76] M. H. W. Chan, A. W. Yanof, and J. D. Reppy, Physical Review Letters **32**, 1347 (1974).

[77] T. E. Washburn, J. E. Rutledge, and J. M. Mochel, Physical Review Letters **34**, 183 (1975).

[78] D. Finotello, K. A. Gillis, A. Wong, and M. H. W. Chan, Physical Review Letters **61**, 1954 (1988).

[79] P. A. Crowell, Ph.D. thesis, Cornell University, Ithaca (1994).

[80] T. Giamarchi, P. L. Doussal, and E. Orignac, Phys. Rev. B **64**, 245119 (2001).

[81] R. H. Tait and J. D. Reppy, Physical Review B **20**, 979 (1979).

[82] P. A. Crowell, F. W. V. Keuls, and J. D. Reppy, Physical Review Letters **75**, 1106 (1995).

[83] A. Golov and F. Pobell, Journal of Low Temperature Physics **101**, 373 (1995).

[84] A. Golov and F. Pobell, Physical Review B **53**, 12647 (1996).

[85] R. H. Torii, H. J. Maris, and G. M. Seidel, Physical Review B **41**, 7167 (1990).

[86] G. B. Huff and J. G. Dash, Journal of Low Temperature Physics **24**, 155 (1974).

[87] M. Hieda, T. Nishino, M. Suzuki, N. Wada, and K. Torii, Physical Review Letters **85**, 5142 (2000).

[88] P. Mohandas, C. P. Lusher, V. A. Mikheev, B. Cowan, and J. Saunders, Journal of Low Temperature Physics **101**, 481 (1995).

[89] T. Kogure, H. Yoshimura, R. Higashino, D. Takahashi, and K. Shirahama, unpublished.

[90] E. Kim and M. H. W. Chan, Science **305**, 1941 (2004a).

[91] Y. Aoki, I. Iwasa, T. Miura, D. Takahashi, A. Yamaguchi, S. Murakawa, and Y. Okuda, Journal of Physical Society of Japan **83**, 084604 (2014).

[92] D. Y. Kim and M. H. W. Chan, Phys. Rev. Lett. **109**, 155301 (2012).

[93] H. J. Maris, Phys. Rev. B **86**, 020502 (2012).

[94] A. S. Nowick and B. S. Berry, *Anelastic Relaxation in Crystalline Solids* (Academic Press, New York and London, 1972).

[95] E. Kim and M. H. W. Chan, Nature **427**, 225 (2004b).

[96] J. Day and J. Beamish, Nature **450**, 853 (2007).

[97] M. A. Paalanen, D. J. Bishop, and H. W. Dail, Physical Review Letters **46**, 664 (1981).

[98] A. D. Fefferman, J. R. Beamish, A. Haziot, and S. Balibar, Journal of Low Temperature Physics **176**, 1 (2014).

[99] MicrotracBEL Corp.

[100] S. Brunauer, P. H. Emmett, and E. Teller, Journal of the American Chemical Society **60**, 309 (1938).

[101] E. P. Barrett, L. G. Joyner, and P. P. Halenda, Journal of the American Chemical Society **73**, 373 (1951).

[102] Cryoconcept.

[103] SOLIDWORKS, Dassault Systèmes SolidWorks Corporation.

[104] COMSOL Multiphysics, and add-on LiveLink for SOLIDWORKS, COMSOL, Inc.

[105] Y. Negishi and K. Shirahama, unpublished.

[106] Sumitomo Heavy Industries, Ltd.

[107] S. Tanuma and T. Mamiya, *Ultralow temperature (Cho-teion)*, [in Japanese] (Kyoritsu Shuppan, Tokyo, 1998).

[108] K. J. R. Rosman and P. D. P. Taylor, Pure and Applied Chemistry **70**, 217 (1998).

[109] TAIYO NIPPON SANSO CORPORATION.

[110] Japan Fine Products.

[111] NIKI GLASS CO., LTD.

[112] Cambridge Isotope Laboratories, Inc.

[113] E. Adams, Review of Scientific Instruments **64**, 601 (1993).

[114] O. Syshchenko, J. Day, and J. Beamish, Physical Review Letters **104**, 195301 (2010).

[115] R. Yu, L. Yin, N. S. Sullivan, J. S. Xia, C. Huan, A. Paduan-Filho, N. F. Oliveira Jr, S. Haas, A. Steppke, C. F. Miclea, et al., Nature **489**, 379 (2012).

[116] J. B. E. White, J. Hessinger, and R. O. Pohl, Journal of Low Temperature Physics **111**, 233 (1998).

[117] J. R. Beamish, in *Handbook of Elastic Properties of Solids, Liquids, and Gases*, edited by M. Levy, H. E. Bass, and R. R. Stern (Academic Press, San Diego, 2001), vol. Volume II, p. 77.

[118] W. Pabst, E. Gregorová, and G. Tichá, Journal of the European Ceramic Society **26**, 1085 (2006).

[119] J. K. Krüger, P. Alnot, J. Baller, R. Bactavatchalou, S. Dorosz, M. Henkel, M. Kolle, S. P. Krüger, U. Müller, M. Philipp, et al., in *Ageing and the Glass Transition*, edited by M. Henkel, M. Pleimling, and R. Sanctuary (Springer-Verlag, Berlin Heidelberg, 2007).

[120] E. Molz, A. P. Y. Wong, M. H. W. Chan, and J. R. Beamish, Physical Review B **48**, 5741 (1993).

[121] C. Ebner and C. C. Sung, Physical Review A **5**, 2625 (1972).

[122] D. Zhou, M. Rall, J. P. Brison, and N. S. Sullivan, Physical Review A **42**, 1929 (1990).

[123] M. Maruyama, M. Bienfait, F. C. Liu, O. E. Vilches, and F. Rieutord, Surface Science **283**, 333 (1993).

[124] K. G. Sukhatme, J. E. Rutledge, and P. Taborek, Journal of Low Temperature Physics **103**, 301 (1996).